Doctoral Thesis

Josephson spectroscopy of single atoms in a scanning tunneling microscope

Martina Trahms, M.Sc.

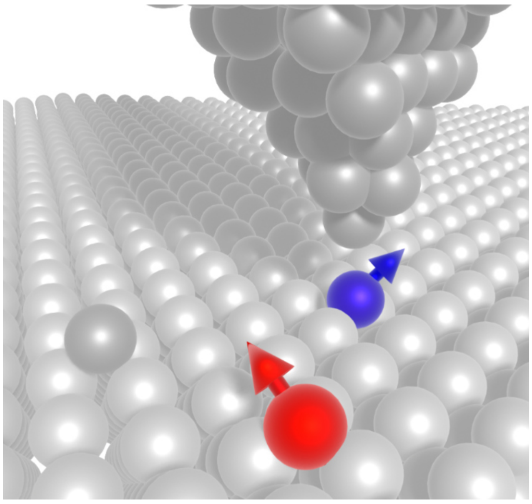

[1]

Dissertation
zur Erlangung des Grades eines
Doktors der Naturwissenschaften (Dr. rer. nat.)

Eingereicht am Fachbereich Physik der
Freien Universität Berlin
vorgelegt von

Martina Trahms

Berlin, 2024

Diese Arbeit ist in der Arbeitsgruppe und mit der Betreuung von Frau Prof. Dr. Katharina J. Franke am Fachbereich Physik der Freien Universität Berlin entstanden.

Erstgutachterin: Prof. Dr. Katharina J. Franke
Zweitgutachter: Prof. Dr. Martin Wolf
Datum der Disputation: 19. Juni 2024

Abstract

Josephson junctions are formed by a non-superconducting weak link between two superconducting electrodes. The dissipation-less superconducting tunnel current flowing across the Josephson junction is carried by superconducting charge carriers which are called Cooper pairs. The tunnel junction is characterized by the overlap of the macroscopic wavefunctions of the two superconducting electrodes. Josephson junctions are highly sensitive to changes of the phase difference between the two wavefunctions.

In this thesis Josephson junctions between a superconducting tip and superconducting sample were investigated in a scanning tunneling microscope (STM). The STM enables atomic resolution of the sample surface as well the formation and manipulation of atomic structures on the surface. Josephson spectroscopy in an STM allows the investigation of the influence of the junction composition on the phase coherence between the macroscopic wavefunctions of the superconducting electrodes on the atomic scale.

Josephson junctions can be interpreted as an oscillating circuit with distinct damping properties. The damping behaviour due to energy losses caused by the interaction with the environment can be frequency dependent. Biasing the Josephson junction by either an applied current or voltage influences the frequency-dependent impedance that couples the system to the electromagnetic environment.

Phase coherence is strongly influenced by the energy exchange of the junction with the environment. In this study, the Josephson junction is exposed to a high frequency (HF) electromagnetic field in order to further investigate the phase coherence of the system. Generally, tunneling charge carriers can absorb quantised energy from the photons of the HF field (photon-assisted tunneling). However, in Josephson contacts coherent absorption of energy from the external field is expected (Shapiro steps). The investigated junctions show resonant absorption at the expected energies in the presence of the HF field. Additionally the current-biased V(I)-curves show a hysteresis depending on the direction of the applied current. This hysteresis indicates phase coherence between tunneling Cooper pairs. However, other features observed in the V(I)-characteristics are correlated to dissipative processes. For that reason a clear identification of Shapiro steps is not possible in this setup.

Furthermore, Josephson spectroscopy was performed on single magnetic adatoms on the Pb(111) surface. The magnetic moment of the atom's unpaired electrons couples to the superconducting condensate and induces localized bound states within the energy gap of the superconductor (YSR states). The tunneling probability for electrons and holes into the YSR states is known to vary due to potential scattering on the surface (electron-hole asymmetry). In a Josephson junction magnetic adatoms were found to induce a diode-like behaviour, i.e., the transition from the resistive single-particle conductance into the Cooper-pair tunneling regime depends on the direction of the applied current. In collaboration with the theory group of Felix von Oppen at Freie Universität Berlin the observed non-reciprocity was correlated to the damping properties of the Josephson junction and explained by the electron-hole asymmetry of the induced YSR bound states.

Kurzzusammenfassung

Ein Tunnelkontakt zwischen zwei Supraleitern durch den ein supraleitender Strom fließt nennt sich Josephson-Kontakt und die tunnelnden Ladungsträger werden als Cooper Paare bezeichnet. Josephson-Kontakte sind sehr empfindlich gegenüber Änderungen der Phasenrelation der makroskopischen Wellenfunktionen der beiden supraleitenden Elektroden.

In dieser Arbeit wurden Josephson-Kontakte zwischen einer supraleitenden Spitze und einem supraleitendem Substrat (Pb(111)) in einem Rastertunnelmikroskop (RTM) untersucht. Mit dem RTM ist es möglich die Oberfläche atomar genau abzubilden und atomare Strukturen zu formen und zu manipulieren. Das eröffnet die Möglichkeit den Einfluss von Änderungen der Josephson-Kontakte auf atomarer Ebene auf die Phasenkorrelation der Wellenfunktionen zu untersuchen.

Josephson-Kontakte können als eine Art Schwingkreis verstanden werden in denen die Dämpfung eine große Rolle spielt. Die Dämpfung kann frequenzabhängig sein und beschreibt den Verlust von Energie des Systems an die Umgebung. Die Frequenzabhängigkeit des untersuchten Systems unterscheidet sich abhängig davon, ob der Kontakt strom- oder spannungs- getrieben ist. Dieser Abhängigkeit wird auf Unterschiede der frequenzabhängigen Impedanz zurückgeführt, mit der das System an die elektro-magnetische Umgebung koppelt.

Die Phasenkohärenz der Josephson-Kontakte ist stark beeinflusst von diesem Energieaustausch. Um die Phasenkohärenz genauer zu untersuchen, wird ein elektromagnetisches (em) Feld eingestrahlt. In Tunnelkontakten können individuell tunnelnde Ladungsträger die quantisierte Energie der Photonen des em Feldes absorbieren (photon-assistiertes Tunneln). In Josephson-Kontakten wird neben diesem Effekt auch die kohärente Absorption der Strahlung erwartet (Shapiro-Stufen). In den untersuchten Kontakten werden Stufen in den Kennlinien bei den erwarteten Energien beobachtet. Zusätzlich tritt in den Stromgetriebenen Josephson Kontakten eine Hysterese abhängig von der Richtung des angelegten Stroms auf. Diese Hysterese deutet auf einen phasenkohärenten Tunnelprozess der Cooper Paare hin. Da allerdings zeitgleich auch dissipative Prozesse erkennbar sind können Shapiro-Stufen nicht eindeutig festgestellt werden.

Zusätzlich zu diesen Erkenntnissen wurde Josephson Spektroskopie auf einzelnen magnetischen Atomen durchgeführt. Der Spin der ungepaarten Ladungsträger der magnetischen Atome wechselwirkt mit dem supraleitenden Kondensat und induziert gebundene Einzelelektronenzustände (YSR-Zustände). Aufgrund von Potential-Streuung durch die Änderung der elektro-magnetischen Umgebung kann die Tunnelwahrscheinlichkeiten in diese Zustände für Elektronen und Löcher variieren (Elektron-Loch-Asymmetrie). In den untersuchten Josephson-Kontakten rufen diese Zustände ein dioden-artiges Verhalten der übergänge von dem normalleitenden zu dem supraleitenden Zustand des Kontakts hervor. In Zusammenarbeit mit der Forschungsgruppe von Felix von Oppen an der Freien Universität Berlin konnte herausgearbeitet werden, dass die Dämpfung der Josephson-Kontakte durch die Elektron-Loch-Asymmetrie der YSR-Zustände beeinflusst wird und für das nicht-reziproke Verhalten der Josephson-CPKontakte verantwortlich ist.

ACRONYMS

BCS	Bardeen-Cooper-Schrieffer
BSCCO	Bismuth strontium calcium copper oxide ($Bi_2Sr_2Ca_nCu_{n+1}O_{2n+6}$)
CPR	current-phase relation
CP	Cooper-pair
Cr	Chromium
DoS	density of states
HF	high frequency
I(V)C	current-voltage characteristic (voltage-biased)
LDoS	local density of states
LHe	liquid Helium
LN_2	liquid Nitrogen
Mn	Manganese
MQT	Macroscopic quantum tunneling
$NbSe_2$	Niobium diselenide
Ne	Neon
Pb	Lead
PID	proportional-integral-derivative
qp	quasiparticle
RCSJ	resistively and capacitively shunted junction
SOC	spin-orbit coupling
SQUID	superconducting quantum interference device
STM	scanning tunneling microscopy
STS	scanning tunneling spectroscopy
V(I)C	voltage-current characteristic (current-biased)
YSR	Yu-Shiba-Rusinov

CONTENTS

III Results and Discussion 83

In Erinnerung an Rosel und Heinz Beblik.
"The ships have come to carry you home"[1]

---

[1] aus dem Stück *Into the west* von Howard Shore, Fran Walsh und Annie Lennox.

CHAPTER 1

INTRODUCTION

Electronic devices that experience asymmetric electrical transport with respect to the biasing direction are essential in technological applications. Semiconducting diodes are among the most prominent representatives of devices experiencing non-reciprocal transport. The observation of a superconducting equivalent where the current flow is dissipation-free in one direction while the other direction can be highly resistive holds the prospect of extremely high rectification ratios between biasing directions. Josephson junctions can be used as a platform to investigate and engineer the properties of superconducting devices. This thesis investigates the phase dynamics of current-biased Josephson junctions within a scanning tunneling microscope (STM) which provides the possibility to manipulate the composition of the junction on the atomic scale.

Josephson junctions consist of two weakly coupled superconductors and enable the tunneling of paired electrons (so called Cooper pairs) through a tunneling barrier as predicted by B.D. Josephson [2] in 1962. The overlap of the macroscopic wavefunctions of the superconductors results in a dissipation-free tunneling current at zero voltage. The properties of Josephson junctions are very sensitive to the phase difference between the wavefunctions.

Enhancing the understanding of the phase dynamics in Josephson junctions enables their implementation in technological devices. For example, superconducting quantum interference devices (SQUIDs) rely on the phase coherent properties in a ring structure containing two Josephson junctions [3]. They are used to detect changes of an external magnetic field on a scale below single flux quanta. An external magnetic field induces a circular current in the ring structure which influences the phase relation of the overlapping wavefunctions within the two junctions. Interference effects occur between the two sides of the ring and cause magnetic field dependent periodic fluctuations of the critical current of the ring structure. At a constant bias current, oscillations of the measured voltage capture changes in the external magnetic field [4].

Phase dynamics are strongly correlated to the potential difference between the two superconducting electrodes. The ac Josephson effect causes the supercurrent of the junction to oscillate with a characteristic frequency for a constant voltage drop across the junction. High frequency (HF) electromagnetic fields are able to resonantly excite Josephson junctions matching their characteristic Josephson frequency. In a current-voltage characteristic (I(V)C) this gives rise to so called Shapiro steps at specific voltage values fulfilling the resonance conditions. Josephson junctions have been suggested to be utilized as voltage standards due to the accuracy of the voltage values of these resonances [5–7].

On a more fundamental level, non-reciprocal behaviour of superconductors and in particular Josephson junctions has recently attracted the attention of the scientific community. The concept of superconducting diodes shows promising potential for technical applications, e.g., in quantum technology [8–11]. F. Ando *et al.* [12] first observed a superconducting diode effect in heterostructures consisting of Nb, V and Ta in 2020. They found that this material system experiences strong spin-orbit coupling which shows a magnetochiral effect in the presence of an external magnetic field perpendicular to the sweep direction. They showed that the maximum supercurrent that this heterostructure supports depends on the direction of the applied current. The superconducting diode effect is understood to be caused by helical superconductivity in systems in which inversion and time reversal symmetry are broken [13, 14]. Helical superconductivity describes a finite Cooper-pair momentum at zero energy, which gives rise to non-reciprocal V(I)Cs.

A similar non-reciprocal effect can be observed in the critical currents of Josephson junctions which are then called Josephson diodes. A high interest in investigating Josephson diodes has been demonstrated in the last few years both experimentally [15–19] and theoretically [20, 21]. In Josephson diodes the current-phase relation becomes asymmetric in response to helical superconductivity. Helical superconductivity is found in superconductors when inversion and time reversal symmetry are broken. Inversion symmetry can be broken by the design of the junction so that $I(V) \neq I(-V)$. For breaking time reversal symmetry usually an external magnetic field is applied. However, H. Wu *et al.* [22] designed a Josephson diode consisting of $NbSe_2$ flakes that are separated by a Nb_3Br_8 thin film without the necessity of an external magnetic field. The design of the junction breaks inversion symmetry and polarizing properties of the Nb_3Br_8 have been suggested to be the cause of breaking time reversal symmetry. The exact origin of time-reversal breaking is still a topic of ongoing investigations and discussions.

In this thesis Josephson spectroscopy was implemented in a STM. Josephson spectroscopy in a STM holds the advantage of controlling the junction on the atomic scale. Scanning tunneling microscopy was first implemented by G. Binnig and H. Rohrer [23, 24] in 1982. The technique is based on measuring a tunneling current though the vacuum barrier between a probing tip and the sample surface. The tunneling current is highly dependent on the tip-sample distance and by scanning the tip over the surface the topography can be reproduced on the atomic scale. Scanning tunneling spectroscopy probes the electronic structure of the surface and can be used to correlates the density of states (DoS) of a surface to its topography. Low-temperature STM has been used to investigate superconducting materials with high spectroscopic energy resolution [25]. For example, the two-band nature of the superconducting state of Pb was shown by M. Ruby *et al.* [26] by resolving coherence peaks at two distinct energies on different surface orientations of Pb. B. Sacépé *et al.* investigated disordered superconductors with STM techniques and found local gap variations on amorphous InO surfaces.

Josephson junctions are formed in an STM by using a superconducting tip material [27, 28]. M. Ternes *et al.* [29] investigated tunneling processes between superconductors with different gap sizes and described the behaviour in terms of multiple Andreev reflections. H. Kimura *et al.* [30] discussed Josephson junctions in an STM on the high temperature superconductor BSCCO in the context of the local superconducting order parameter. J. G. Rodrigo *et al.* [31] performed Josephson spectroscopy on the atomic scale to investigate phase diffusion effects and the interaction of the junction with the electromagnetic environment. J. Senkpiel *et al.* [32] investigated high transmission Josephson junctions in STM experiments and modelled the results within the dynamical Coulomb blockade regime.

In STM experiments it has been shown that single magnetic atoms on a superconducting surface induce electronic states as their magnetic moment couples to the superconducting condensate [33–35]. These states are commonly named after L. Yu [36], H. Shiba [37] and A. I. Rusinov [38] (YSR) who independently derived the first theoretical description at the same time. The energy of YSR states holds information of the coupling strength of the electronic spin of the atom to the superconducting condensate. M. Ruby *et al.* analysed the tunneling and relaxation processes into YSR states [39] and investigated local YSR patterns of single magnetic Mn adatoms on Pb surfaces [40] as well as their hybridization into YSR bands for Mn dimers [41]. L. Farinacci *et al.* [42] showed a quantum phase transition upon changing the coupling strength of the magnetic adsorbate on the superconducting substrate by interaction with STM tip. E. Liebhaber *et al.* [43] investigated the influence of the charge density wave in $NbSe_2$ on the hybridized YSR states in atomic Fe chains.

The first STM Josephson experimetn in the presence of single magnetic atoms was performed by M. T. Randaria *et al.* [44]. A reduction of the Josephson peak intensity at zero bias was observed in the presence of magnetic adatoms on the surface. Recently F. Küster *et al.* [45] correlated the reduction of the Josephson peak by different magnetic adatoms on a Nb(110) surface to the d-orbital occupation of the magnetic adatom.

So far Josephson junctions have mainly been investigated by voltage-biased STM junctions [27–31]. Voltage-biased STM Josephson junctions have been modelled under the assumption of incoherent Cooper-pair tunneling events by P(E)-theory calculations [32, 46–48]. The Cooper-pair transport through these junctions consists of single tunneling events of particles with a charge of 2e. This is confirmed in experiments by applying an external high frequency (HF) irradiation to the junction [49–52]. The energy splitting of the conductance peaks in the presence of HF irradiation depends on the number of particle that tunnel simultaneously. Multi-particle tunneling processes result in a smaller energy splitting compared to single-particle tunneling events. Photon-assisted tunneling of individual Cooper pairs is observed in the energy splitting of the Josephson peak. Since the investigated voltage-biased Josephson junctions lack phase coherence between tunneling events, external irradiation is not absorbed resonantly in the form of Shapiro steps.

In this thesis current-biased Josephson spectroscopy was performed in STM experiments since the phase dynamics of the Josephson junction are not directly influenced by an applied current. To investigate the phase coherence and the coupling of the junction to the electromagnetic environment current- and voltage- biased junctions are compared.
To further investigate the phase coherence in the Josephson junction an external HF-field was applied. It is known that voltage-biased Josephson junctions incoherently absorb energy from the HF-field by photon-assisted tunneling. However, current-biased Josephson junctions do not inherently affect the phase coherence and may interact differently. Current-biased Josephson junctions are investigated in the presence of HF irradiation to gain information on the interplay of coherent and incoherent absorption of energy in the junction.
To investigate the Josephson diode effect in the absence of an external magnetic field, single-atom magnetic impurities were included in the STM Josephson junctions. The influence of the induced YSR states on the phase dynamics of the Josephson junctions was investigated in collaboration with the theory group of Felix von Oppen at Freie Universität Berlin.

Thesis structure

This thesis is divided into three parts separating the theoretical background from the experimental details and the results. The theoretical background gives an overview of the physics that is necessary to understand the results of the thesis. The experimental methods include STM theory and STM operation techniques as well as a description of the adjustments of the setup to perform Josephson spectroscopy. Furthermore the sample and tip preparation is explained and the data analysis is explained in detail. The result section focusses on the physics of the STM Josephson junctions investigated in this thesis in particular with regard to HF irradiation and the presence of magnetic adatoms.
In chapter 2, the fundamental properties of superconductivity are discussed with emphasize on YSR - physics and their implication for tunneling experiments (chapter 2.3). Multi-particle tunneling processes and the formation of Andreev bands are

explained in chapter 2.4.

The theoretical background to understand the phase dynamics in Josephson junctions is given in chapter 3. The resistively and capacitively shunted junction (RCSJ) model and the washboard potential picture is explained in chapter 3.1. Here the concept of frequency-dependent damping in Josephson junctions is introduced. The relevant energy scales of Josephson junctions are defined in chapter 3.2. The concept of incoherent Cooper-pair tunneling and the treatment of these processes by P(E)-theory are presented. In chapter 3.3 the influence of HF irradiation on Josephson junctions is discussed. Photon-assisted tunneling processes as well as Shapiro steps are considered in this chapter. Finally the superconducting diode effect and the implications for Josephson diodes is explained in chapter 3.4.

Part II of the thesis gives details about the experimental techniques and data analysis. STM theory is presented in chapter 4.1. The experimental setup and operation techniques of the STM are described in 4.2. In chapter 4.3 a description of the surface and tip preparation as well as the evaporation of single magnetic Mn and Cr adatoms is found. The induced YSR states for the two atom species are characterized. The adjustments to the setup designed to enable current-biased Josephson spectroscopy and the tip stabilization process are described in chapter 4.4.

The data treatment was mostly performed by self written python programs and is explained in chapter 5. Since Josephson spectroscopy is performed at (for STM experiments) unusually high conductances, the voltage-biased conductance spectra need to be corrected for systematic influences of the line resistance (chapter 5.1). The statistical nature of the Josephson experiments required the acquisition of up to 2500 bias sweeps for each data point. The analysis of this large amount of data and challenges that come with measuring in close proximity to the surface for an extended period of time are described in chapter 5.2. In the presence of HF frequency the damping of the HF lines need to be determined. For that purpose the splitting of the conductance peaks in the voltage-biased spectra were simulated as explained in chapter 5.3.

Part III shows and discusses the experimental findings of this thesis. In chapter 6 a short summary of the RCSJ model and washboard potential picture is given in chapter 6.1. The current- and voltage- biased Josephson junction results are described in chapter 6.2 and 6.3, respectively. The measured data is put into context with the theoretical models that were previously described and differences between the two biasing methods are pointed out (chapter 6.4). In chapter 7, the V(I)Cs that were measured under the application of high frequency irradiation are presented. A short summary of the theoretical concepts of photon-assisted tunneling and Shapiro steps in overdamped and underdamped is presented in chapter 7.1. The current-biased data is discussed in chapter 7.2. In chapter 7.3 the data is discussed in comparison with the voltage-biased data. Josephson junctions formed on single magnetic impurities are shown in chapter 8. The range of influence of the magnetic adatom on the superconducting condensate is estimated by acquiring Josephson data in close lateral proximity to a Mn adatom (chapter 8.1). The observed non-reciprocities in the retrapping and switching currents is discussed in chapter 8.2 and 8.3, respectively. In chapter 8.4 the theoretical considerations that went into the simulation and reproduction of the non-reciprocities are explained as performed by the group of Felix von Oppen at Freie Universität Berlin. The affect of the magnetic adatoms on the damping properties of the Josephson junction that results in a diode-like behaviour is discussed in chapter 8.5.

In the end the results and conclusions are summarized and an outlook is given for future investigation of STM Josephson junctions (chapter 9).

Part I

Theoretical background

CHAPTER 2

GENERAL INTRODUCTION TO SUPERCONDUCTIVITY

Superconductivity was first observed by H. Kamerlingh Onnes who succeeded in liquefying Helium at 4.2 K in 1911 [53]. By cooling down Hg he found a sudden jump to zero of the resistance at a critical temperature T_{C}. While a decrease of the resistance with decreasing temperature is not surprising, a finite residual resistance due to electron-electron scattering is expected for a normal metal [54].

In addition to the disappearance of the resistance at a critical temperature, superconductors behave as perfect diamagnets as shown by W. Meissner and R. Ochsenfeld [55]. Generally, diamagnetism induces an opposing magnetic field within the material that counteracts an external magnetic field. A perfect diamagnet refers to a susceptibility of $\chi = -1$ which completely expels the magnetic field from its interior as the magnetization M cancels the field strength H.

$$B = \mu_0 H(1+\chi) = \mu_0(H+M) \rightarrow M = -H \tag{2.1}$$

In paramagnets the diamagnetic forces are overcome as unpaired electrons align with the external magnetic field.

The difference between a perfect conductor and a perfect diamagnet is most clearly explained by their behaviour within a magnetic field. Both materials go through a transition from the normal conducting to the perfect conducting or diamagnetic state when cooled down sufficiently. An external magnetic field that is applied to the materials in the perfect conducting/diamagnetic state cannot enter either of the materials due to the induced screening currents. On the other side of the transition, i.e. in the normal conducting state, magnetic field lines penetrate both materials. Maintaining the applied magnetic field during the transition to the perfect conducting/diamagnetic state, the materials behave differently. At the transition temperature the perfect diamagnet expels the flux from its interior and screening currents prevent magnetic field lines within the material. In contrast, the perfect conductor

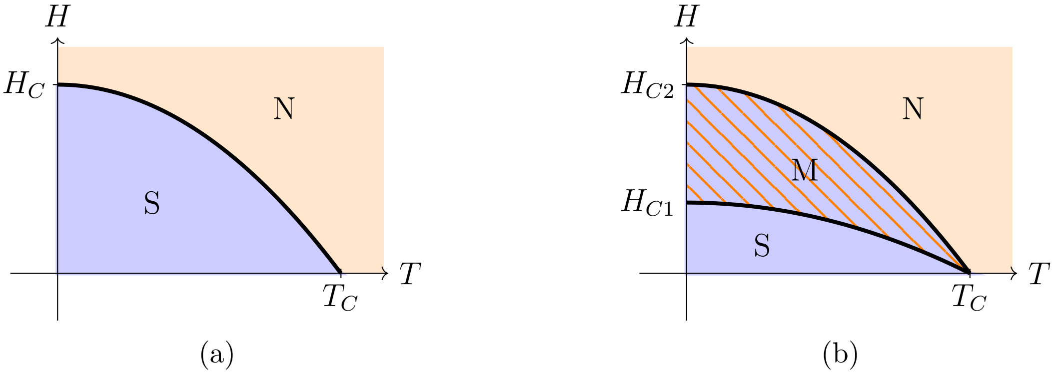

Figure 2.1: Phase diagrams $H_C(T)$ for a) type I and b) type II superconductors. a) The superconducting state (S) transitions directly to the normal conducting state (N). b) Exceeding the first critical field H_{C1} the magnitude of the magnetization decreases gradually and the mixed phase (M) is formed. At the second magnetic field H_{C2} the material becomes normal conducting.

freezes the magnetic field lines in place. The perfect conductor counteracts changes of the external magnetic field, maintaining the original field in its interior. That means when the external field is turned off below the transition temperature, the perfect conductor still maintains the magnetic field lines while the perfect diamagnet stays field free. A perfect conductor is conserving the magnetic flux while perfect diamagnetism/superconductivity is a flux expelling phenomenon [56].

The superconducting state is susceptible to temperature and magnetic field. Exceeding a critical temperature T_C or a critical field H_C destroys the superconducting phase. The phase diagram is shown in figure 2.1a for a so called type I superconductor. Type I superconductors transition sharply from the normal conducting to the superconducting state. A microscopic theory for these superconductors was developed by J. Bardeen , L. N. Cooper and J. R. Schrieffer (BCS) [57] which was awarded with the Nobel prize in 1972. More details will be given in chapter 2.2.

Another type of superconductor referred to as type II superconductor experiences an intermediate or mixed phase, in which the magnetic field can penetrate the superconductor partially (figure 2.1b). The Ginzburg-Landau theory is a phenomenological model that captures the properties of type II superconductors as well [58] (see chapter 2.1). Type II superconductors enter the mixed phase at a first critical field strength H_C1 at which flux quanta start penetrating the material. In contrast to type I superconductors, the magnetization in type II superconductors decreases gradually with increasing applied magnetic field until it reaches zero at the second critical field value H_C2. For more details on the phenomenology of superconductivity see [56, 59–61].

In the next chapters 2.1 and 2.2 a more detailed introduction to the theoretical considerations of superconductivity will be given with emphasis on the BCS theory. For the experiments conducted in this thesis magnetic impurities on superconducting surfaces play a major role. Their mathematical description is given in chapter 2.3. Phenomena at interfaces between superconductors and normal or insulting areas are such as Andreev reflections and the proximity effect discussed in chapter 2.4.

2.1 Basic terms of superconductivity

Before going into the theoretical description of superconductivity by BCS-theory in this chapter a more qualitative and intuitive description of the most important concepts is given. These concepts are well known and are summarized from the following text books [56, 59, 61].

Below the critical temperature of a superconductor it becomes energetically favourable for electrons to form pairs. These pairs are integer-spin particles (Bosons) and condensate into a common ground states at the Fermi energy E_{F}. The superconducting state is a macroscopic quantum phenomenon which is described by a single macroscopic wavefunction $\Psi = |\Psi(r,t)|e^{i\Theta(r,t)}$. Accordingly, the charge carriers with energies around the Fermi level have the same ground-state and interact coherently on the length scale of their coherence length ξ_0 which was first introduced by A. B. Pippard [62].

The macroscopic wavefunction can be interpreted as a probability function for the quantum particles and the absolute square is linked to the density of superconducting charge carriers $|\Psi|^2 = n_s$. A phenomenologically description was derived in form of the London equations which result from purely electrodynamic considerations. It describes perfect conductivity and an exponential decay of magnetic fields at the interface of the material on the length scale of the London penetration depth λ.

Bardeen-Cooper-Schrieffer (BCS) theory describes the origin of superconductivity on a microscopic level. It is based on the formation of Cooper pairs below the material's specific critical temperature T_{C}. A Cooper pair consists of two electrons with opposite spin and momentum coupled by electro-phonon interaction. Accordingly, Cooper pairs have an integer spin and therefore are no longer subject to the Pauli exclusion principle and a single quantum phase is formed that may be described by a single macroscopic wavefunction. The energy that is required to break a Cooper pair is given by the wavefunction's order parameter 2Δ.

Formation of Cooper Pairs. The underlying assumption of BCS theory is the existence of a positive interaction between electrons that overcomes the Coulomb repulsion. In a classical approach this interaction takes place indirectly via crystal lattice deformations (phonons). The first electron interacts with the lattice leaving a polarized trail. The second electron is attracted by this lattice distortion which leads to a positive net interaction between the two electrons. The BCS theory states that the Fermi sea is unstable against this kind of pair formation. The momentum absorbed from the first electron will be transferred to the second by the lattice atoms. The Cooper pairs are formed in a narrow energy range around the Fermi energy E_F and the interaction is mediated by the phonons which have much larger energies in the order of $\hbar\omega_D$. The Debye frequency ω_D corresponds to the frequency of the highest occupied phonon energy state. The length scale of this attractive interaction is defined as the BCS-coherence length ξ_0.

The BCS gap. The formation of Cooper pairs implies that no single particle excitations are possible with energies that are insufficient to break the superconducting state. Therefore an energy gap is formed in the quasiparticle density of states around zero energy. The size of the gap is given by the minimum energy to break the Cooper pairs in that specific material Δ. There is a direct correlation between the gap size of the superconductor and its critical temperature $\Delta(0) = 1.76k_BT_C$. The superconducting gap closes as the critical temperature is approached and vanishes upon exceeding T_C. Δ corresponds to the minimum excitation energy of a single-particle as will be shown in the next section going into more detail of the BCS theory. It may have a phase ϕ that corresponds to the phase between the hole and electron like components of the ground state.

Ginzburg-Landau Theory takes spatial variations of the density of the superconducting charge carriers n_S into account by introducing a pseudowavevector $\Psi(r)$ as an order parameter with $|\Psi(r)|^2 = n_S(r)$. For that reason the theory is well applicable at interfaces from superconducting to non-superconducting materials and gives an intuitive understanding of the mixed phase in type II superconductors. The Ginzburg-Landau coherence length ξ_{GL} gives a measure of the length scale on which the density can vary. The London penetration depth λ determines the extent to which an external magnetic field may penetrate into a superconductor before it is completely screened. Combining these two parameters gives a phenomenological explanation for the existence of type II superconductors. At the interface of a normal to a superconducting material an external magnetic field penetrates the surface of the superconductor up to the London penetration depth λ. If the Ginzburg-Landau coherence length is smaller than the penetration depth the superconducting electron density varies at a smaller scale. For that reason it is possible to develop normal conducting cores for the flux vortexes which are screened by a circular supercurrent. The ratio of the London penetration depth and the Ginzburg-Landau coherence length $\kappa = \frac{\lambda}{\xi_{GL}}$ determines the behaviour of the superconductor (type I: $\kappa < \frac{1}{\sqrt{2}}$, type II: $\kappa > \frac{1}{\sqrt{2}}$).

2.2 Basics of Bardeen-Cooper-Schrieffer theory

This chapter mostly follows the notation used in 'Introduction to superconductivity' by M. Tinkham [59] (chapters 3.3, 3.5 and 3.7). Further information and insights were taken from [56, 63, 64].

The formation of Cooper pairs is described by the pairwise creation of electrons with opposite spin and momentum so that a single pair's wavefunction is represented by:

$$|\Psi_0\rangle = \sum_{k>k_F} g_k c^\dagger_{k\uparrow} c^\dagger_{-k\downarrow} |F\rangle . \tag{2.2}$$

where $|F\rangle$ represents the Fermi sea and g_k is a probability weight that needs to be determined for each pair. The operators $c^\dagger_{k\uparrow}$ and $c^\dagger_{-k\downarrow}$ create electrons of a certain momentum $k/-k$ and spin $\uparrow/\downarrow$. To avoid too many arguments in the sum and the determination of individual weights for many electron pairs a mean-field approach is chosen. The average amount of occupied ($|v_k|^2$) and unoccupied pair states ($|u_k|^2$) determines the occupancy of each individual Cooper-pair state ($|u_k|^2 + |v_k|^2 = 1$) and the BCS ground state is written as:

$$|\Psi_G\rangle = \Pi_{k=k_1\ldots k_M}(u_k + v_k e^{i\phi} c^\dagger_{k\uparrow} c^\dagger_{-k\downarrow}) |\phi_0\rangle . \tag{2.3}$$

ϕ_0 is the particle-free vacuum state and $e^{i\phi}$ allows for a phase factor between u_k and v_k. Ideally non-paired electrons are neglected and the pairing Hamiltonian is given by

$$H = \sum_{k,\sigma} \xi_k n_{k\sigma} + \sum_{k,l} V_{k,l} c^\dagger_{k\uparrow} c^\dagger_{-k\downarrow} c_{l\uparrow} c_{-l\downarrow}. \tag{2.4}$$

$V_{k,l}$ describes the interaction of Cooper pairs scattering from the $(l\uparrow, -l\downarrow)$ state to the $(k\uparrow, -k\downarrow)$ state, requiring the state with momentum l to be filled and the state with momentum k to be empty. $\xi_k = \epsilon_k - E_F$ corresponds to the energy of a single particle relative to the Fermi energy E_F.

Equation 2.4 can be equivalently rewritten as the model Hamiltonian H_M for the coherent state that has non-vanishing expectation values of $\langle c_{-k,\downarrow} c_{k,\uparrow}\rangle$. Additionally the superconducting gap parameter is defined as

$$\Delta_k = -\sum_l V_{kl} \langle c_{-l\downarrow} c_{l\uparrow}\rangle, \tag{2.5}$$

so that the Hamiltonian becomes:

$$H = \sum_{k,\sigma} \xi_k c^\dagger_{k,\sigma} c_{k,\sigma} - \sum_k (\Delta_k c^\dagger_{k\uparrow} c^\dagger_{-k\downarrow} + \Delta^*_k c_{-k\downarrow} c_{k\uparrow} - \Delta_k \langle c^\dagger_{-k,\downarrow} c^\dagger_{k,\uparrow}\rangle). \tag{2.6}$$

The Hamiltonian is diagonalized by the Bogoliubov transformation:

$$c^\dagger_{-k\downarrow} = u^*_k \gamma^\dagger_{k\uparrow} - v_k \gamma_{k\downarrow} \tag{2.7}$$

$$c_{k\uparrow} = u_k \gamma_{k\downarrow} + v^*_k \gamma^\dagger_{k\uparrow}. \tag{2.8}$$

The new Fermi operators $\gamma^\dagger_k$ and γ_k are quasiparticle operators and have an electron and hole-like component, i.e. $\gamma^\dagger_k$ may create an electron with $k\uparrow$ or destroy an an electron with $-k\downarrow$ to the effect that the system's spin quantum number increases as well as its momentum is increased by k. Accordingly $\gamma_{k,\downarrow}$ decreases the momentum

and spin quantum number of the system.
With equation 2.4, 2.7 and 2.8 the coefficients for occupied and unoccupied states u_k and v_k can be determined

$$\begin{gathered}|v_k|^2 = 1 - |u_k|^2 = \frac{1}{2}(1 - \frac{\xi_k}{E_k}) \\ \text{with } E_k = (\Delta^2 + \xi_k^2)^{\frac{1}{2}}.\end{gathered} \tag{2.9}$$

ξ_k is the single-particle energy with respect to the Fermi level and E_k the excitation energy of a quasiparticle with $\hbar k$. For more details on this derivation see [59] or [63].
The energy gap becomes

$$\Delta_k = -\sum_l V_{kl} u_l^* v_l \langle 1 - \gamma_{l\downarrow}^\dagger \gamma_{l\downarrow} - \gamma_{l\uparrow}^\dagger \gamma_{l\uparrow} \rangle \tag{2.10}$$

The quasiparticle density of states can be derived by using the quasiparticle operators

$$\gamma_{k,\downarrow}^\dagger = u_k^* c_{k\uparrow}^\dagger - v_k^* c_{-k\downarrow}, \tag{2.11}$$

$$\gamma_{k,\uparrow}^\dagger = u_k^* c_{-k\downarrow}^\dagger + v_k^* c_{k\uparrow}, \tag{2.12}$$

$$\gamma_{k,\downarrow} = u_k c_{k\uparrow} - v_k c_{-k\downarrow}^\dagger, \tag{2.13}$$

$$\gamma_{k,\uparrow} = u_k c_{-k\downarrow} + v_k c_{k\uparrow}^\dagger. \tag{2.14}$$

As $|\Psi_G\rangle$ is the BCS ground state no quasiparticle can be annihilated from that state, i.e. $\gamma_{k\downarrow}|\Psi_G\rangle = \gamma_{k\uparrow}|\Psi_G\rangle = 0$ using equations 2.13 and 2.14. Equation 2.11 and 2.12 create a quasiparticle excitation that does not condense into the common groundstate of the Cooper pairs. These quasiparticle excitations increase the energy of the system. Quasiparticle excitations are created or annihilated in pairs so that two states are created with $\xi_{ek} = E_k + E_F$ and $\xi_{hk} = E_k - E_F$ with respect to the Fermi energy E_F for electron and hole energies, respectively. For that reason in spectroscopy experiments the measured energy has the gap of 2Δ.
During the superconducting transition the number of particles is conserved. In the superconducting state the number of quasiparticles $N_S(E)dE$ must correspond to the number of normal conducting states $N_n(\xi)d\xi$ due to the direct relation of the quasiparticle excitation operator $\gamma_k^\dagger$ to the electron creation operator $c_k^\dagger$. E is the quasiparticle excitation energy in the superconducting state while ξ corresponds to the single-particle energy in the normal state. Their relation is given in equation 2.9. As the relevant energy scales are small the normal conducting electron states

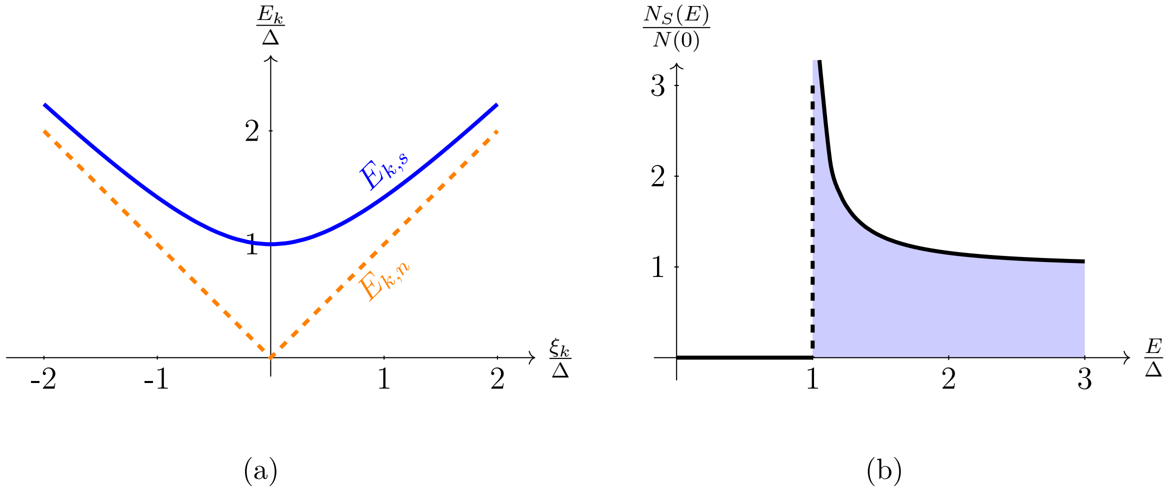

(a) (b)

Figure 2.2: Single particle excitations (a) and quasiparticle density of states (b) of a superconductor according to equation 2.15. a) shows the single particle excitation in a superconductor $E_{k,s}$ (blue line) and normal conductor $E_{k,n}$ (orange dashed line). Excitations with energies below Δ in the normal conducting state are lifted above Δ in the superconducting state. Accordingly, in b) no quasiparticles exist below $E = \Delta$. The number of particles is conserved as the function diverges at Δ. Images adapted from [59].

at ξ are essentially equal the states at Fermi energy (here set to zero).

$$\begin{aligned} N_S(E)dE &= N_n(\xi)d\xi \approx N(0)d\xi \\ \frac{N_S(E)}{N(0)} &= \frac{d\xi}{dE} = \begin{cases} \frac{E}{\sqrt{E^2-\Delta^2}} & \text{for } E \geq \Delta \\ 0 & \text{for } E < \Delta \end{cases} \end{aligned} \tag{2.15}$$

Excitations with momentum k corresponding to $\xi_k < \Delta$ in the normal conducting state are raised to energies above Δ in the superconductor (figure 2.2a). The total number of particles is conserved which is met by a diverging density of states just above Δ (figure 2.2b).

2.3 Magnetic impurities on superconducting surfaces

In this chapter we focus on the interaction of single magnetic adatoms with the superconducting condensate. In this chapter we will first discuss a magnetic adatom with spin S on a metal surface to explain the concept of potential scattering and exchange scattering. These concepts are applicable for magnetic impurities on a superconducting surfaces as well as will be explained next.

In the following description we will focus on the spin 1/2 system, though the concept

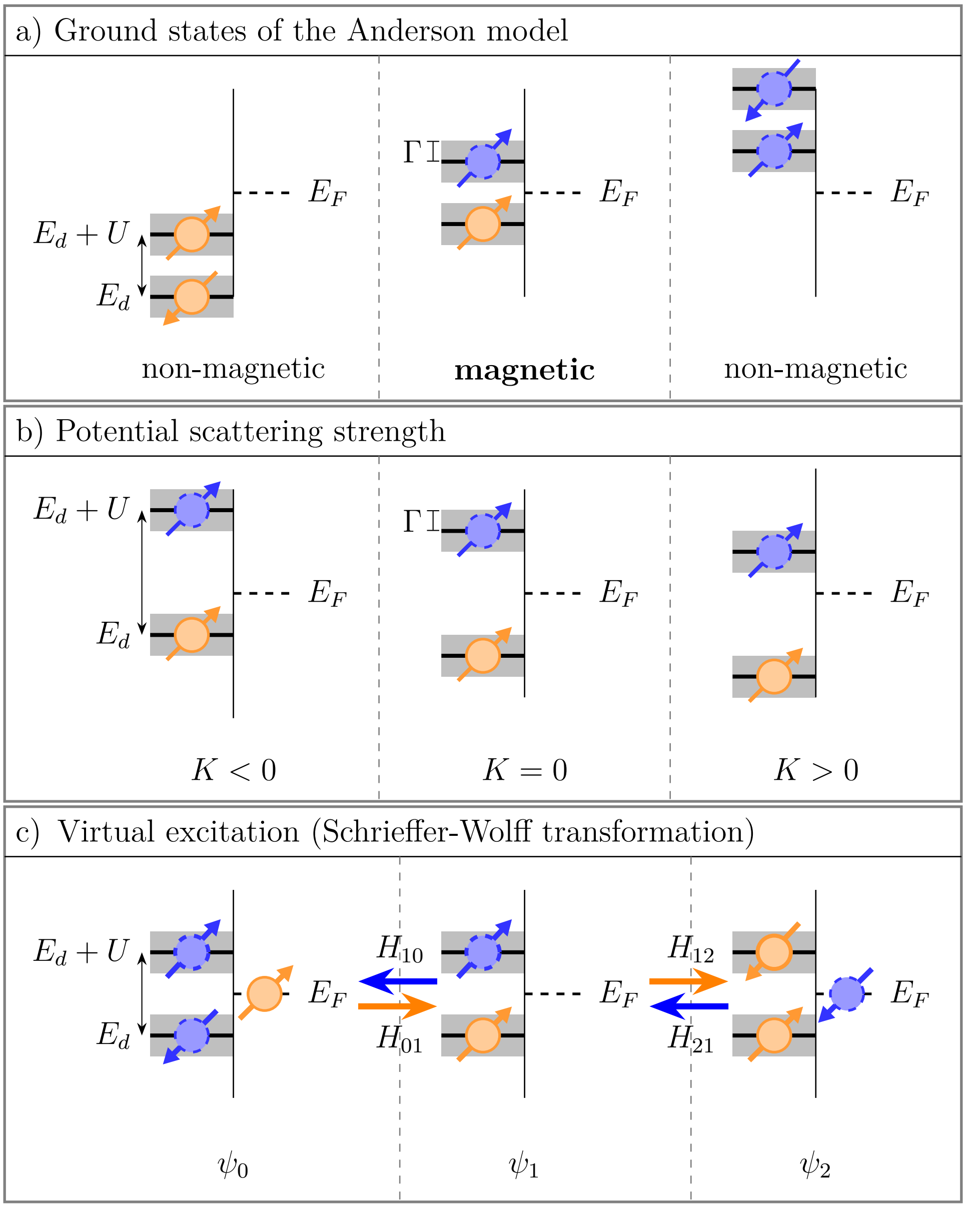

Figure 2.3: Anderson impurity model for an impurity on a metal surface. The degeneracy of the d-level E_d is lifted by the Coulomb interaction U. a) Possible ground states of the Anderson model. If the both d-level energies are above or below the Fermi energy E_F the d-level is either completely empty or filled. In the absence of a magnetic moment no exchange interaction is observed. If E_F of the substrate is between E_d and $E_d + U$, the d-level is singly occupied giving rise to a magnetic moment on the surface. b) Potential scattering of a magnetic impurity depends on the asymmetry of the d-levels with respect to E_F of the metal. If E_d and $E_d + U$ to E_F are symmetric around E_F no potential scattering is observed. c) Virtual excitations of the magnetic ground state ψ_1 to the conduction band of the metal. Transitions to the empty ψ_0 and the filled d-level state ψ_2 are possible.

is applicable to higher spin number systems as well. The magnetic moment of the adatom attracts charge carriers with opposite spin within the metal substrate. The effect of this kind of magnetic screening on a metal surface is well investigated and results in the so called Kondo-effect [65]. The Kondo-effect is discussed within the framework of the Anderson impurity model.

The Anderson impurity model

In the Anderson impurity model the interaction of the impurity with the crystal field is taken into account. It allows for the spin level of the impurity to be changed (occupied or unoccupied) by the surrounding conduction electrons from the crystal. The Hamiltonian of the system is describes by:

$$H_A = \sum_{\alpha} E_d d_{\alpha}^{\dagger} d_{\alpha} + \sum_{k\alpha} E_k c_{k\alpha}^{\dagger} c_{k\alpha} + U n_{d\uparrow} n_{d\downarrow} + \sum_{k,\alpha} (V_k^* d_{\alpha}^{\dagger} c_{k,\alpha} + V_k c_{k,\alpha}^{\dagger} d_{\alpha}) \tag{2.16}$$

The first part of the Hamiltonian describes the occupation $d_{\alpha}^{\dagger}$ or depletion d_{α} of the impurity state based on the location of the impurity state at energy E_d relative to the Fermi level E_0. The second term takes into account the Coulomb repulsion U of electrons that are localized at the impurity with $n_{\sigma} = d_{\alpha}^{\dagger} d_{\alpha}$. The last part of the Hamiltonian describes the hybridization of the impurity state with the conduction electrons with momentum k by V_k. Annihilating a conduction electron ($c_{k,\alpha}^{\dagger}$) and creating an electron on the impurity site (d_{α}) occupies the impurity state by a conduction electron [63, 66].

In the Anderson impurity model the degeneracy of the spin states of the d-level of the impurity is lifted by the Coulomb interaction U. As shown in figure 2.3a) the ground state of the impurity's d-level can either be singly occupied, doubly occupied or empty depending on the relative location of the impurity energy levels with respect to the Fermi energy. The impurity is magnetic only if the d-level is singly occupied which is the case when $E_d < E_F < E_d + U$. Additionally, hybridization of the impurity with the metal is taken into account and gives the impurity states a finite width that depend on the occupation rate of the spin state $\Gamma \propto |V_k|^2$ by the conduction electrons of the metal substrate. The impurity is screened by conduction electrons if $U < \Gamma$.

Scattering events on the impurity site are treated in more detail by the Schrieffer-Wolff transformation (see figure 2.3 c)). In the case of a singly occupied impurity level virtual excitation processes of the impurity electrons to the Fermi sea of the metal are taken into account. These processes violate energy conservation and are therefore only accessible within the Heisenberg uncertainty principle. In figure 2.3c) the two excitation levels from the singly occupied ground state ψ_1 are illustrated. The impurity can either be doubly occupied ψ_2 or empty ψ_0 in the excited state. The wavefunction becomes a three component vector $\psi = (\psi_0, \psi_1, \psi_2)$ and the Hamiltonian given in 2.16 can be separated into a 3x3 tensor.

$$\begin{pmatrix} H_{00} & H_{01} & H_{02} \\ H_{10} & H_{11} & H_{21} \\ H_{20} & H_{21} & H_{22} \end{pmatrix} \begin{pmatrix} \psi_0 \\ \psi_1 \\ \psi_2 \end{pmatrix} = E \begin{pmatrix} \psi_0 \\ \psi_1 \\ \psi_2 \end{pmatrix} \tag{2.17}$$

$H_{nn'} = P_n H P'_n$ corresponds to the transition from the occupation state n to n' of the d orbital of the impurity. P_n is the projection operator of the respective occupation subspace with

$$\begin{aligned} P_0 &= (1 - n_{d\uparrow})(1 - n_{d\downarrow}) \\ P_1 &= n_{d\uparrow} + n_{d\downarrow} - 2n_{d\uparrow}n_{d\downarrow} \\ P_2 &= n_{d\uparrow}n_{d\downarrow} \end{aligned} \tag{2.18}$$

Excitations $H_{20} = H_{02} = 0$ do not exist as they involve a two electron transfer which is not supported by the Hamiltonian in equation 2.16. The residual off diagonal elements stem from the hybridization of the impurity with the substrate as shown in figure 2.3c).

$$\begin{aligned} H_{10} = H_{01}^{\dagger} &= \sum_{k,\alpha} V_k d_{\alpha}^{\dagger}(1 - n_{d,-\alpha})c_{k,\alpha} \\ H_{12} = H_{21}^{\dagger} &= \sum_{k,\alpha} V_k d_{\alpha}^{\dagger} n_{d,-\alpha} c_{k,\alpha}. \end{aligned} \tag{2.19}$$

Eliminating ψ_0 and ψ_2 the corresponding Hamiltonian becomes:

$$H = \sum_{k,k'} J_{k,k'}(S^+ c_{k,\downarrow}^{\dagger} c_{k'\uparrow} + S^- c_{k\uparrow}^{\dagger} c_{k'\downarrow} + S_z(c_{k\uparrow}^{\dagger} c_{k',\uparrow} - c_{k\downarrow}^{\dagger} c_{k'\downarrow})) + \sum_{k,k} K_{kk'} c_{k\uparrow}^{\dagger} c_{k'\uparrow} \tag{2.20}$$

with

$$\begin{aligned} \text{Exchange scattering}: \ J_{k,k'} &= V_k^* V_{k'} \left(\frac{1}{U + E_d - E_{k'}} + \frac{1}{E_k - E_d}\right) \\ \text{Potential scattering}: \ K_{k,k'} &= \frac{V_k^* V_{k'}}{2}\left(\frac{1}{E_k - E_d} - \frac{1}{U + E_d - E_{k'}}\right) \end{aligned} \tag{2.21}$$

The first term corresponds to the exchange coupling term derived from the sd-model with S_z and $S^{\pm} = S_x + \pm i S_y$ being spin operators.

Conduction electrons with energy $E_{k/k'}$ in close vicinity of the Fermi energy contribute most to the scattering events at the impurity ($E_k \approx E_{k'} \approx E_F$), $E_F - E_d$ corresponds to the distance of the singly occupied d level to the Fermi energy and $U + E_d - E_F$ corresponds to the distance of the first unoccupied d-level of the impurity [67, 68].

In figure 2.3b) the consequences of equation 2.21 for the potential scattering term is illustrated. If the split d-levels are symmetric around the Fermi energy the potential scattering term becomes zero. In the case of the occupied state being closer to the Fermi level the potential scattering term becomes negative $K_{kk'} < 0$. If the unoccupied state is closer to the Fermi level the potential scattering is positive $K_{kk'} > 0$

[67, 68].

On the other hand, the exchange coupling depends only on the distance of the singly and doubly occupied d-level from the Fermi energy. Going back to figure 2.3a) it becomes apparent that if both levels are far above or below the Fermi energy of the metal, the exchange interaction becomes zero and the impurity becomes a pure potential scatterer. The energy scales on which either of these scattering events occur are very small in comparison to the energy scales on which the d-levels are split [67, 68].

In figure 2.3 c) the spin states are degenerate, i.e. the spin state of the ground state for spin up and down are the same. Scattering of conduction electrons from the impurity that result in spin-flip events of the ground state cause a many-body state that screens the spin of the magnetic impurity and is called the Kondo-effect [65].

Yu-Shiba-Rusinov states

In the case of the substrate being a superconductor, the conduction electrons are bound in Cooper pairs of opposing spin and momentum [34, 69]. As a result the impurity creates a Bogoliubov quasiparticle state inside the superconductor. The induced quasiparticle can screen the atom's magnetic moment. The formal description of these states was performed by Yu [36], Shiba [37] and Rusinov [38] and are therefore called Yu-Shiba-Rusinov states (YSR states). The first experimental observation followed in 1997 by Yazdani *et al.* [35].

The quasiparticle state is accessed via the following creation and annihilation operators introduced in 2.11 - 2.14:

$$\begin{aligned} \gamma^\dagger &= u^* c_\alpha^\dagger + v^* c_\beta \\ \gamma &= u c_\alpha - v c_\beta^\dagger \end{aligned} \tag{2.22}$$

α sets the spin and momentum of the electron that is created or annihilated with β having the directly opposite spin and momentum. For a classical magnetic adatom on a superconducting surface two kinds of interaction are relevant.

The exchange interaction J(r) has been introduced for impurities on a metal surface within the Anderson model in the previous section. On a superconductor it describes the coupling of the magnetic moment of the impurity atom to the spin of a quasiparticle in the Cooper-pair condensate. Exchange scattering results in a pair breaking potential and the impurity's spin may be screened or unscreened depending on the strength J. The Hamilton operator is given by

$$H_{ex} = \int dr \sum_{\alpha\beta} \psi_\alpha^\dagger(r) J_\alpha(r) S \sigma_{\alpha\beta} \psi_\beta(r) \tag{2.23}$$

$\psi_\alpha^\dagger(r)/\psi_\beta^\dagger(r)$ are spatial dependent fermionic creation and annihilation operators for the spin states α and β. S is the spin state of the adatom that is exchange coupled

to the conduction electron spin via the Pauli matrix elements $\sigma_{\alpha\beta}$ in spin space [63, 66, 68].
The potential scattering K(r) takes the disturbance of the crystal electrical field by the addition of a foreign adatom into account. In the previous section we have seen that K(r) originates from the asymmetric arrangement of the split energy levels around the Fermi energy of the substrate. The Coulomb interaction $U(r)$ results in an electrical potential that introduces an asymmetry in the occupation probabilities of electrons and holes. In tunneling experiments that leads to a discrepancy of the tunneling rates for inserting or extracting an electron. The probability with which a quasiparticle state may be occupied by a particle or hole is indirectly probed in tunneling experiments and is reflected in the tunneling probabilities for electrons ($|u|^2$) and holes ($|v|^2$). The energy of the quasiparticle state is not affected severely as the potential scattering energy is usually small compared to the exchange scattering energy. Formally the Hamiltonian for the potetnial scattering can be written as

$$H_{pot} = \int dr \sum_{\alpha} \psi_{\alpha}^{\dagger}(r) K(r) \tau_z \psi_{\alpha}(r) \tag{2.24}$$

K(r) denotes the strength of the potential scattering and τ_i are the Pauli matrices in Nambu space equivalent to σ_α in spin space [63, 66, 68].
The impurity is often considered to have a very local influence on the superconductor so that $K(r) = V_0\delta(r-r_0)$ and $J(r) = J_0\delta(r-r_0)$. The Hamiltonian can be separated in independent 2x2 Matrices for spin up and spin down along the z-direction [66]

$$H_{\pm} = \xi_p\tau_z + (K\tau_z \mp JS)\delta(r) + \Delta\tau_x. \tag{2.25}$$

This Hamiltonian gives rise to sub-gap energy states called YSR states which localized at the impurity site [66, 68]:

$$\epsilon_{\pm} = \pm\Delta\frac{1-\alpha^2+\beta^2}{\sqrt{(1-\alpha^2+\beta^2)^2+4\alpha^2}} \tag{2.26}$$

$\alpha = \pi\rho_0 SJ$ is related to the exchange interaction while $\beta = \pi\rho_0 K$ is caused by potential scattering. K is usually small compared to J. ρ_0 is the normal state density of states. The wavefunction directly at the impurity site $\Psi(0)$ can be determined to be

$$\Psi(0) = \begin{pmatrix} u(0) \\ v(0) \end{pmatrix} = C \begin{pmatrix} \sqrt{1+(\alpha\pm\beta)^2} \\ \pm\sqrt{1+(\alpha\mp\beta)^2} \end{pmatrix}. \tag{2.27}$$

Here $u(0)$ is the electron-like component of the Bogoliubov quasiparticle state and $v(0)$ the hole-like component. The difference in sign comes from the separation of the system in spin up and spin down electrons that was made in 2.25. The particle-hole asymmetry is given in dependence of the scattering potential K and results in unequal occupation probabilities of the YSR states [66, 68].

Excitations of YSR states

The system's ground state is determined by the coupling energy J of the magnetic moment of the atom to the superconducting condensate. If $J < J_C$ the magnetic moment on the surface is not screened (S= $\frac{1}{2}$). The impurity localizes a Cooper pair without breaking it. On the other hand, if $J > J_C$ the system is in the screened spin state (S= 0). In that scenario the coupling is strong enough to break a Cooper pair and couple to a single quasiparticle state [33, 64, 68, 70]. It has been shown that by changing the coupling strength of a molecule on a superconducting surface it is possible to smoothly transition between these two regimes [42].

Both regimes are illustrated in figure 2.4. To excite a YSR state an electron may be added or removed, e.g., by tunneling experiments. For the unscreened (screened) ground state the YSR state is excited by creating (annihilating) a quasiparticle state according to equation 2.22. The excited state corresponds to the screened (unscreened) state. The quasiparticle state may in both regimes be created by tunneling an electron-like particle at positive energies or a hole-like particle at negative energies. In the screened ground state a Cooper pair from the condensate is broken. Similarly, the hole (electron) excitation process of the unscreened (screened) ground state leads to a reduction (increase) of the total number of Cooper pairs in the system. The alteration of the number of Cooper pairs does not lead to measurable influences on the condensate and therefore on the energy of the YSR state [63]. Note that the tunneling does not occur by the orbitals of the magnetic atom but via the quasiparticle state induced by the impurity spin [33]. Due to the potential scattering K the electron u and hole v components of the quasiparticle state are not equal which influences the tunneling probabilities at positive and negative energies. In figure 2.4 a finite potential scattering is assumed. The spectral weights reverse upon changing the ground state of the system. This is due to the excitation changing from the creation to the annihilation of a quasiparticle state which has reversed electron and hole components [33, 64, 68, 70].

In tunneling experiments an actual electron or hole is introduced to the system. That may require creating or annihilating Cooper pairs to explicitly create an additional electron or hole. For that purpose the Cooper-pair creation $S^\dagger$ and annihilation operators S are introduced. The excitation of a hole $\gamma_{hk}^\dagger$ is the same operation as destroying a Cooper pair and creating an electron $S\gamma_{ek}^\dagger$. The eigenvalue of S is related to the phase factor $e^{i\phi}$ of Δ, i.e. the phase between u and v component [59].

2.4 Andreev reflections

At interfaces the macroscopic wavefunction of a superconductor meets a normal conducting (SN-junction) or insulating (SI-junction) material. One of the main features of such an interface consists in the superconductor's wavefunction penetrating

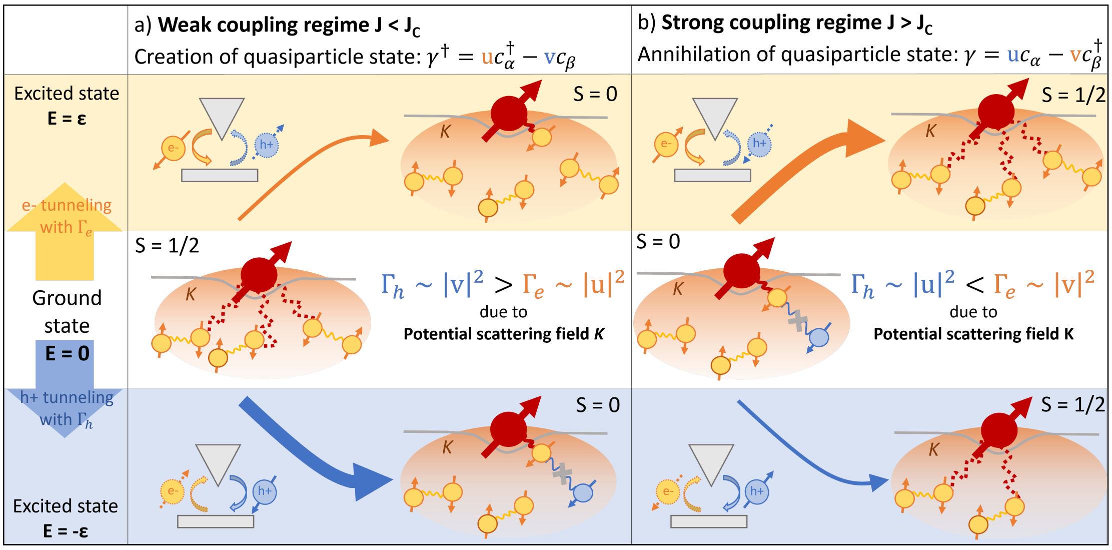

Figure 2.4: Tunneling processes into a superconductor via a magnetic impurity with potential scattering $K < 0$. a) shows the unscreened ground state ($J < J_C$) in the weak coupling regime. The excited states at $\pm\epsilon$ is the screened state accessible via electron or hole tunneling illustrated in the upper and lower part of the figure. a) shows the unscreened ground state ($J < J_C$). Tunneling a hole is favourable to create the quasiparticle state. This effect is reversed in b) which shows the screened ground state ($J > J_C$) in the strong coupling regime. The size of the orange and blue arrows indicate the tunneling probabilities of electrons and holes, respectively. The asymmetric probabilities are caused by potential scattering. Adapted from [64, 68].

into the normal conducting or insulating barrier. This is equivalent to Cooper pairs leaking into the normal conductor which provides it with superconducting properties with a reduced superconducting gap. This phenomenon is called proximity effect and is commonly observed as thin metal layers becoming superconducting in close proximity to the superconductor [71]. It is equally true that normal electrons disturb the superconducting phase on the other side of the interface. The latter effect is usually small and is neglected using so called rigid boundary conditions [72–74]. The proximity also affects the interface between superconductors with different gaps.

Another aspect comes from scattering effects at the interfaces between superconducting and normal conducting (SN) materials. At the interface so called Andreev reflections may occur [75]. Due to the superconducting gap, single charge carriers with $E < \Delta$ can not transfer between the two materials. However, it is possible to generate a Cooper pair ($2e^-$) by transferring an electron (e^-) and simultaneously reflecting a hole (e^+). The process is illustrated in figure 2.5a). The effect can be considered as a parallel two channel system for electrons and holes. In [76] a δ potential with the dimensionless height Z is introduced to account for the transparency of the junction $D = \frac{1}{1+Z^2}$. If $Z = 0$ the BCS gap is completely filled up to twice the normal state conductance of $2G_N$. Depending on the transmission t_n of each channel n the conductance across the junction is given by [73, 74]:

$$G_{NS} = \frac{2e^2}{\pi\hbar} \sum_{n=1}^{N} \frac{t_n^2}{2 - t_n} \tag{2.28}$$

In a single Andreev scattering event the reflected hole (electron) acquires a phase compared to the initial electron (hole).

$$\begin{aligned} \phi_h &= \phi_e + \phi_s + \arccos(E/\Delta) \\ \phi_e &= \phi_h - \phi_s + \arccos(E/\Delta) \end{aligned} \tag{2.29}$$

where $\phi_{e/h}$ is the phase of the reflected electron/hole and ϕ_s is the phase of the macroscopic superconducting wavefunction [73, 74]. The last term $\arccos(E/\Delta)$ corresponds to an additional phase shift that comes from the penetration of the wavefunction into the superconductor and is related to the energy of the electron/hole compared to the pair potential of the superconductor.

In the case of a superconductor - normal conductor - superconductor (SNS) junction this phase shift becomes more relevant. For a sufficiently thin normal conducting layer, the same particle may be reflected multiple times between the two superconductors as shown in figure 2.5 b). Furthermore, from equation 2.29 we can observe that the particle acquires a phase during each reflection process $\phi = \phi_{s1} - \phi_{s2} + \pi$. A resonance condition is met when $\phi_{s1} - \phi_{s2} = n\pi$ For this conditions so called Andreev bound states are induced in the junction with energy:

$$E = \pm\Delta\sqrt{1 - D\sin^2(\frac{\phi}{2})}, \tag{2.30}$$

where D is the junction transparency. The Andreev states can be considered as Andreev bands with dispersion, i.e. a finite width which is determined by D. The energy-phase relation of an Andreev band for different values of D is shown in figure 2.5c). The phase-dispersion relation is given by

$$I_S = (\frac{2e}{\hbar}\frac{dE}{d\phi}) \tag{2.31}$$

which only depends on the phase relation between the two superconductors ϕ. The band dispersion can be correlated to the current-phase relation of a Josephson junction which will be discussed in more detail in the next chapter [74].

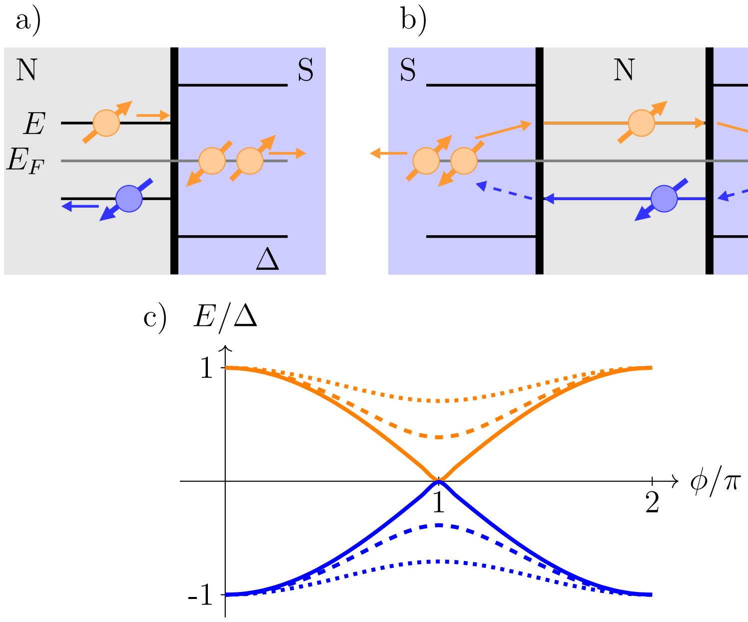

Figure 2.5: Schematic illustration of Andreev reflections at a) an SN junction, where an electron is reflected as a hole and a Cooper pair is created in the superconductor. b) shows an SNS junction where an electron/hole is reflected multiple times back and forth between the two superconductors. Depending on the phase difference between the superconductors ϕ resonance conditions are met for certain energies. The so formed Andreev bands for different values of junction transparencies D according to equation 2.30 ($D = 1$, 0.75, 0.5 for solid, dashed, dotted lines) are shown in c). Adapted from [74].

CHAPTER 3

JOSEPHSON JUNCTIONS

In a Josephson junction Cooper pairs tunnel directly through a sufficiently small barrier [2]. At finite energy Cooper pairs may be transferred indirectly via Andreev reflections as described in the previous chapter. This process is analogous to the quantum mechanical tunnel effect of electrons. Cooper pairs tunnel when the macroscopic wavefunctions Ψ of the two superconductors overlap ($\Psi_1 = |\Psi_1|e^{i\phi_1}$, $\Psi_2 = |\Psi_2|e^{i\phi_2}$) as depicted in figure 3.1a. The barrier between the superconductors influences the overlap of the macroscopic wavefunctions [74, Chap. 1.2].

In a Josephson junction a dissipation-less current is measured due to the direct tunneling of Cooper pairs up to the junction's critical current I_C at which superconductivity breaks down. In Josephson experiments the junction is biased by a current while recording the voltage, which jumps from zero to a finite voltage value at I_C.

In chapter 4 single-particle tunneling and in particular quasiparticle tunneling between two superconductors is discussed in detail. In STM experiments single-particle tunneling events through a vacuum barrier are recorded by the tunneling current. If both electrodes are superconductors the quasiparticle density of states, as derived in equation 2.15, is reproduced by the first derivative of the current (dI/dV) (more details in chapter 4). The transmission through the tunneling barrier is determined by the tip-sample distance and can be quantified by the normal state conductance $G_N = I_N/V$ for normal state currents I_N measured at voltages V far larger than Δ/e [77, Chap. 3]. With decreasing tip-sample distance the normal state conductance increases. For high conductances the macroscopic wavefunctions of the two superconductors start to overlap and Cooper-pair tunneling becomes possible. The junction becomes a Josephson junction, opening a new tunneling channel at zero voltage.

In figure 3.1b the ideal voltage-current characteristic (V(I)C) of a Josephson junction in comparison with a single-particle tunneling current-voltage characteristic (I(V)C) is shown.

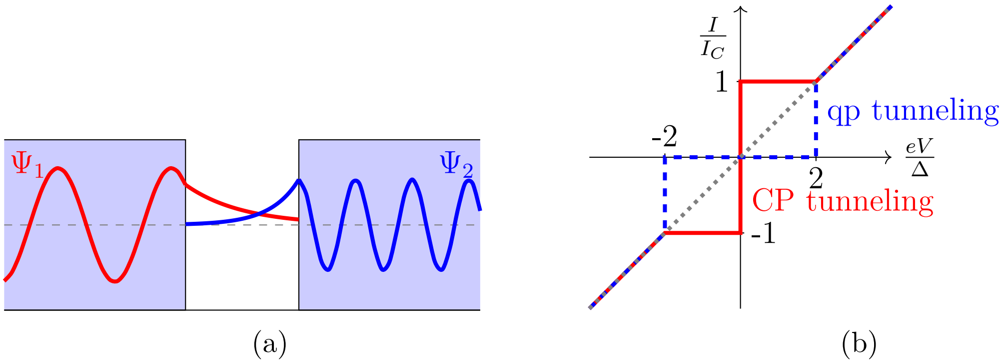

Figure 3.1: a) Two superconductors with wavefunctions Ψ_1 and Ψ_2 are separated by a thin insulating barrier. Within the barrier the wavefunctions decay exponentially. As long as there is an overlap of the wavefunctions Cooper pair tunneling is possible. b) Ideal V(I)C for a (overdamped) Josephson junction (red line), and I(V)C for single particle tunneling between two superconductors (blue line) and a normal conductive junction with ohmic resistance (gray dotted line). Both red and blue curves have superconducting electrodes, however in the first case the macroscopic wavefunctions overlap and permit Cooper-pair (CP) tunneling while the other shows purely quasiparticle (qp) tunneling.

Single-particle tunneling: In the superconducting state no single particles are allowed at energies below 2Δ, i.e. at voltages below $2\Delta/e$ no single-particle current is measured. At higher voltages enough energy is provided to split Cooper pairs in both electrodes and quasiparticles start to tunnel.

Cooper-pair tunneling: A dissipation-less Josephson junction is realized for applied currents below I_C. In an ideal Josephson junction the measured voltage jumps to a value of 2Δ/e at the critical current.

In this chapter we focus on current-biased Josephson junctions. The supercurrent density J_S is a function of the phase difference with the following restrictions [77, Chap. 1]:

- The overlap of the macroscopic wavefunctions change periodically with the phase difference $\phi = \phi_1 - \phi_2$ between the two superconductors across the junction. For that reason, the current density is 2π-periodic ($J_S(\phi) = J_S(\phi + 2\pi n)$).

- If there is no current passing through the junction the phase difference must be zero ($J_S(\phi = 0) = J_S(2\pi n) = 0$).

These requirements are most simply met by the current-phase relation of the dc Josephson equation:

$$\text{1. Josephson equation:} \qquad J_S = J_C \sin\phi \qquad [2] \tag{3.1}$$

This is the first or dc Josephson equation. J_C is the maximum current density that the junction can withstand before breaking the zero-voltage state [59, 74, 77]. An expression for the critical current I_C which is an inherent property of the Josephson junction has been provided by V. Ambegaokar and A. Baratoff [78]:

$$I_C(0) \approx \frac{\pi\hbar}{eR_N}\frac{\Delta_R\Delta_L}{\Delta_L+\Delta_R} \tag{3.2}$$

This equation is often referred to as AB-formula and in this form is valid if the two superconducting electrodes have similar pairing energies ($\Delta_L \approx \Delta_R$) and at T = 0. For finite temperatures and for a symmetric junction ($\Delta_L = \Delta_R = \Delta$) it gives

$$I_C(T) = \frac{\pi\hbar}{2eR_N}\Delta(T)\tanh(\frac{\hbar\Delta(T)}{2k_BT}). \tag{3.3}$$

.

The relative energies of the two electrodes, i.e. a voltage drop across the junction, is directly correlated to a change of the relative phase of the two superconductors over time according to the ac Josephson equation:

$$\text{2. Josephson equation:} \qquad V = \frac{\hbar}{2e}\frac{\partial\phi}{\partial t} \qquad [2] \tag{3.4}$$

The phase difference of the two superconductors becomes time dependent:

$$\phi(t) = \frac{2e}{\hbar}Vt + \phi_0 \tag{3.5}$$

The two Josephson equations 3.1 and 3.4 result in the ac Josephson effect. A voltage drop across the junction causes an alternating current.

$$I_S = I_C \sin(\frac{2e}{\hbar}Vt + \phi_0) \tag{3.6}$$

Accordingly, the oscillation frequency of the current resulting from an applied dc voltage V_dc is called the Josephson frequency ω_J [74, Chap. 1.2]

$$\frac{\omega_J}{2\pi V_{dc}} = \frac{e}{\pi\hbar} = \frac{1}{\Phi_0} \approx 483.6\,\frac{\mathrm{GHz}}{\mathrm{mV}}. \tag{3.7}$$

The energy stored in the junction can be deduced from equation 3.1 and 3.4 as follows

$$\begin{aligned} E_J &= \int_0^{t_0} I_S V dt \\ &= \frac{I_C\hbar}{2e}\int_0^{\phi}\sin(\phi(t))d\phi \end{aligned} \tag{3.8}$$

with $\phi(0) = 0$ and $\phi(t_0) = \phi$.

$$E_J = \frac{I_C\hbar}{2e}(1 - \cos(\phi)) \quad = E_{J0}(1 - \cos(\phi)) \tag{3.9}$$

The Josephson energy corresponds to the maximum energy that can be stored in the junction given by $E_{J0} = \frac{\hbar I_C}{2e}$ [77, Chap. 2].
As the junction is able to store energy, the Josephson junction can be treated as a non-linear inductor. The response of the junction to an alternating current can be derived directly from the Josephson equations 3.1 and 3.4:

$$\frac{dI(t)}{dt} = I_C \cos\phi \frac{d\phi}{dt} = I_C \cos\phi \frac{2e}{\hbar} V = \frac{\cos\phi}{L_J} V, \tag{3.10}$$

with

$$L_J = \frac{\hbar}{2eI_C\cos(\phi)} = \frac{L_C}{\cos(\phi)}. \tag{3.11}$$

The junction's inductance L_J shows oscillatory behaviour with the time dependent phase difference ϕ in response to an applied dc voltage. These oscillations are called Josephson oscillations [77, Chap. 2].
From these equations a fundamental difference between Josephson junctions that are biased by a current source in comparison to a voltage source arises. The phase dynamics are strongly influenced by the bias and are either driven by a voltage or evolve freely with an applied current. In the absence of noise, an applied current does not change ϕ over time. In contrast, a voltage bias directly causes a phase change over time and therefore is never a static case. The topic of how phase dynamics are influenced in different energy regimes of the junction will be discussed throughout this chapter.

3.1 RCSJ model and the washboard potential

Previously, the general concept of Cooper pairs tunneling through a barrier maintaining the zero-resistance state was discussed. When describing the junction in a more realistic scope, i.e. at currents around the transition to the resistive state, the resistively and capacitively shunted junction (RCSJ) model comes into play [79, 80]. The model is discussed in various text books and scripts and the following section is primarily based on [59, 74, 77], if not indicated otherwise. A summary of the most important parameters of a Jospehson junction that are introduced in this chapter and their physical meaning is given in table 3.1.

In the RCSJ model a real junction is described by adding a resistive, a capacitive and a fluctuating element in parallel to the ideal Josephson junction. The equivalent circuit is shown in figure 3.5 a). The resistive term is generated by tunneling quasiparticles that may come from thermal excitations and is assumed to follow ohmic behaviour $I_N = V/R_N$. R_N is the resistance of the junction in the normal conducting state and it corresponds to the normal state conductance $G_N = \frac{1}{R_N}$. At the critical current the junction transitions to the resistive state with a finite characteristic voltage

$$V_C = I_C R_N. \tag{3.12}$$

The second part of the RCSJ model consists in the capacitance that is formed by the two electrodes of the junction. It results in a displacement current in response of the charging or discharging of the capacitor $I_D = C\frac{\partial V}{\partial t}$. Lastly current fluctuation, e.g. from thermal or other noise sources, is treated by another unspecific contribution to the current I_F. The combination of the four components described above lead to the following second order differential equation in ϕ:

$$\begin{aligned} I(t) &= \overbrace{\quad I_S \quad}^{\substack{\text{super} \\ \text{current}}} + \overbrace{\quad I_R \quad}^{\substack{\text{resistive} \\ \text{current}}} + \overbrace{\quad I_D \quad}^{\substack{\text{displacement} \\ \text{current}}} + \overbrace{\quad I_F \quad}^{\substack{\text{fluctuation} \\ \text{current}}} \\ &= I_C \sin\phi + V/R_N + C\frac{\partial V}{\partial t} + I_F \\ &= I_C \sin\phi + \frac{\hbar}{2e}\frac{1}{R_N}\frac{\partial \phi}{\partial t} + \frac{\hbar}{2e}C\frac{\partial^2 \phi}{\partial t^2} + I_F \end{aligned} \tag{3.13}$$

Ignoring the fluctuation term for now, the first Josephson equation 3.1 is reproduced for a static phase difference across the junction. The RCSJ model treats the physical consequences of the phase dynamics in the junction. The RCSJ model gives a very intuitive picture for the phase dynamics when connecting equation 3.13 to a mechanical analogue. The differential equation 3.13 formally shows similarities to the general differential equation of a particle with mass M in a periodic potential

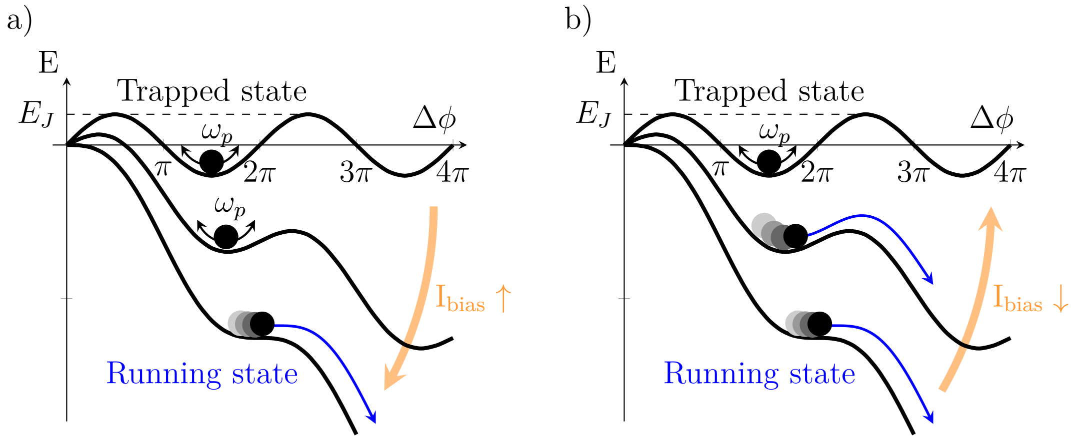

Figure 3.2: Ideal washboard potential derived from the RCSJ model. a) at zero bias the phase particle is trapped inside a potential minimum and the phase difference across the junction is constant. As the bias is increased, the potential is tilted and the effective maxima become smaller until they disappear at I_C and the phase particle switches to the running state where the phase is continuously changing and voltage drop occurs across the junction. b) an underdamped junction behaves differently when the bias current is decreased and the phase particle is in the running state initially. The inertia of the phase particle in the absence of damping causes the particle to overcome potential maxima for currents below I_C until it is eventually retrapped at I_re.

U in the presence of damping η

$$M\frac{d^2x}{dt^2} + \eta\frac{dx}{dt} + \nabla U = 0. \tag{3.14}$$

To compare eq 3.13 to 3.14 we multiply with $\frac{\hbar}{2e}$:

$$\left(\frac{\hbar}{2e}\right)^2 C\frac{d^2\phi}{dt^2} + \left(\frac{\hbar}{2e}\right)^2 \frac{1}{R_N}\frac{d\phi}{dt} + \left(\frac{\hbar}{2e}\right)(I_C\sin\phi - I(t) + I_F) = 0. \tag{3.15}$$

The following assignments can be made:

$$\begin{aligned} M &= \left(\frac{\hbar}{2e}\right)^2 C & \nabla U &= \left(\frac{\hbar}{2e}\right)(-I(t) + I_C\sin(\phi) + I_F) \\ \eta &= \left(\frac{\hbar}{2e}\right)^2 \frac{1}{R_N} & \hookrightarrow U &= E_{J0}(1 - \cos\phi - \frac{I(t)}{I_C}\phi + \frac{I_F}{I_C}\phi). \end{aligned} \tag{3.16}$$

Phase dynamics can be intuitively visualized in this analogy to a mass particle in a periodic potential. In the Josephson junction a phase particle is placed in a potential U that is described in terms of the Josephson energy $E_{J0} = \frac{\hbar}{2e}I_C$ (derived in the previous section) [77]. The mass M of the phase particle is given by the capacitive

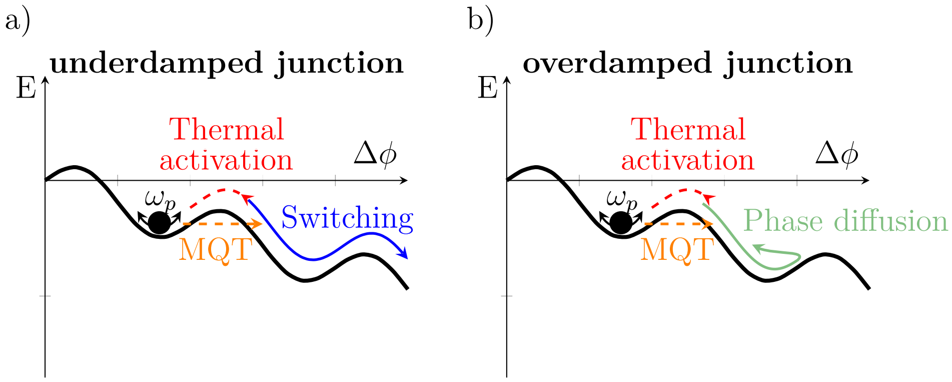

Figure 3.3: There are different mechanisms that cause the phase particle to escape below I_{C}. Thermal activation can lift the particle to a potential maximum. Additionally, Macroscopic Quantum Tunneling (MQT) has been observed for low noise junctions as the phase particle tunnels through the potential barrier. In the underdamped case a) the phase particle has enough energy to overcome subsequent potential maxima and the junction switches prematurely into the running state. If the junction is over damped b) the phase particle is retrapped in one of the following minima due to the damping. A finite voltage is measured however, the particle is not in the free running state.

term and the damping η by the normal state resistance of the junction. An applied current tilts the periodic potential and results in the tilted washboard potential of the RCSJ model depicted in figure 3.2 a). The fluctuation term additionally 'shakes' the tilt angle of the potential. Neglecting the fluctuation current and without a driving current the potential follows a cosine periodic shape around zero. As the washboard potential starts tilting the effective maxima become smaller until they disappear at $I_s = I_C$.

From the previous discussion we know that the Josephson junction can either be in the zero- or the resistive-state. In the tilted washboard potential picture for currents below the critical current the phase particle is trapped in a potential minimum. As the particle is trapped in this state the phase is not changing over time corresponding to $V = 0$. The potential maxima disappear at I_C so that the particle escapes and freely runs down the potential. This corresponds to a continuous change of the phase in time and therefore to a finite voltage across the junction. This transition from the trapped (zero) state to the running (resistive) state is depicted in 3.2 a).

Analogous to a pendulum that oscillates around equilibrium in the absence of a driving force the trapped phase particle can oscillate around its equilibrium position. The plasma frequency ω_p of a Josephson junction is a measure for this oscillation. On average the phase is not changing over time so that $V \propto \frac{d\phi}{dt} = 0$. Equation 3.13 gives the following differential equation in the absence of an applied current $I_{\mathrm{b}} = 0$

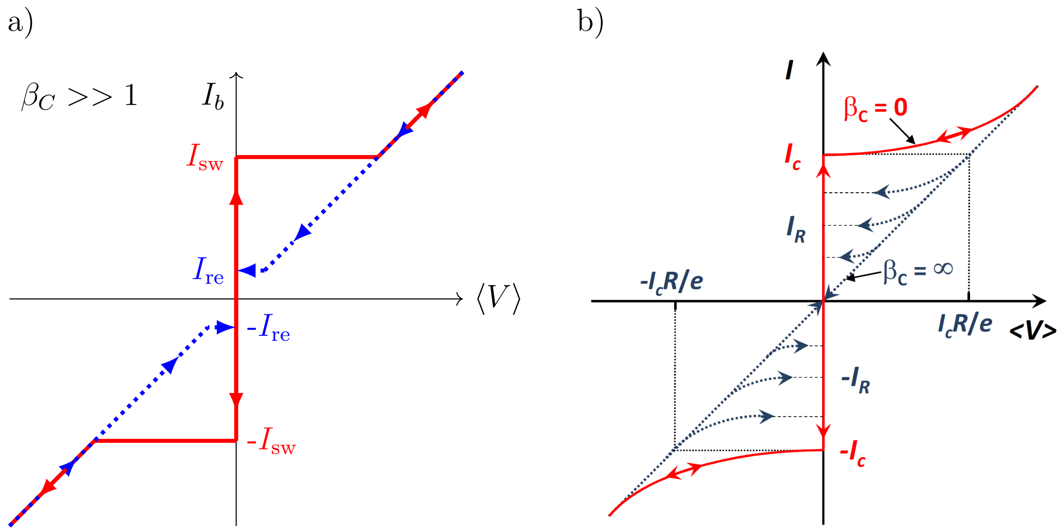

Figure 3.4: Schematic V(I)Cs of a Josephson junctions with different damping properties . a) V(I)C for an underdamped junction with $\beta_C >> 1$. The direction dependent transitions between regimes are marked as switching currents I_{sw} and retrapping currents I_{re}. b) shows V(I)Cs for different damping values β_C. Small β_C values correspond to an overdamped junction for which no hysteresis is observed. As β_C increases the curves become hysteretic [77].

and noise fluctuations $I_F = 0$

$$\left(\frac{\hbar}{2e}\right) C \frac{d^2\phi}{dt^2} = I_C \sin\phi \tag{3.17}$$

which is solved by

$$\phi = \omega_p t \rightarrow \omega_p = \sqrt{\frac{2e}{\hbar}\frac{I_C}{C}}. \tag{3.18}$$

More technically speaking the plasma frequency corresponds to the electrical resonance frequency of the $L_J C$-circuit formed by the capacitance from the RCSJ model and the Josephson inductance L_J.

Overdamped and underdamped junctions

As described above the damping and inertia are determined both by the normal state resistance R_N and the capacitance of the junction C. Several parameters are defined by different authors to quantify damping and here we will focus on the Sterwart-McCumber parameter β_C [80] and the quality factor Q

$$\begin{aligned} \beta_C &= \frac{2e}{\hbar} I_C R_N^2 C \\ Q &= \frac{\hbar}{2e}\sqrt{\beta_C} = \omega_p R_N C \end{aligned} \tag{3.19}$$

[74, 77]. The junction shows properties of an underdamped junction at large capacitance when $\beta_C > 1$. On the other hand, when the capacitance is small the junction is overdamped and $\beta_C < 1$. In figure 3.4 the IV characteristics of a Josephson junction with varying damping properties are shown.

In the washboard potential picture, overdamped and underdamped Josephson junctions are distinguished by the behaviour of the phase particle when it starts at the potential maximum with no excess energy. As the particle gains energy from moving down the potential well there are two possible scenarios:

1. The underdamped case: The provided energy is sufficient to overcome the next potential maximum and the phase particle switches into the running state.
2. The overdamped case: The particle looses energy due to the damping and it stays trapped in the next potential minimum.

In figure 3.4 a) an exemplary V(I)C is shown for an underdamped junction. In the underdamped junction, the phase particle switches into the running state as soon as it reaches a potential maximum in a slightly tilted washboard potential. If the trapped phase particle is provided with sufficient energy a transition to the running state at currents below I_C is possible. This is called premature switching and the corresponding current value is defined by the **switching current** $I_{\mathbf{sw}}$ of the junction. Premature switching becomes more likely for higher applied currents as the effective height of the potential maxima decreases with increasing tilt angle of the washboard potential. As indicated in figure 3.3 a) thermal or other noise sources are predominantly responsible for premature switching in the junctions discussed in this thesis. In low noise junctions, macroscopic quantum tunneling (MQT) is another possible reason for premature switching. MQT occurs when the phase particle tunnels directly through the potential barrier.

Another feature of an underdamped junction is the observation of a hysteretic behaviour as shown in the V(I)Cs in figure 3.4 b) for a varying amount of damping. The transition between running and trapped state depends on the initial state of the phase particle. So far the transition from the initially trapped to the running state of the phase particle has been discussed. In the running state the particle has a finite inertia which is not compensated by damping. The energy that the particle gains from the previous potential maximum is sufficient to overcome the next maximum as long as there is a finite tilt of the washboard potential. In the absence of noise the phase particle is retrapped in a potential minimum at currents close to zero bias. Noise enables retrapping events at higher current values. The retrapping event at a finite **retrapping current** $I_{\mathbf{re}}$ is shown in figure 3.2 b)). This hysteretic behaviour between forward and backward sweep in V(I)Cs is characteristic for the underdamped Josephson junction. In an underdamped junction the V(I)Cs are ambiguous and both states are unstable against external noise.

This is not the case for the phase dynamics in an overdamped Josephson junction were the V(I)Cs are well defined. Here, the phase particle looses energy due to friction and is not able to overcome the next potential maximum starting from the previous maximum. If the particle escapes a minimum, e.g. induced by noise, the junction does not switch into the running state but retraps immediately in one of the next minima. In the strongly overdamped junction no premature switching is observed as noise does not trigger the escape process. The system remains in a quasi static state where the phase particle escapes and is being retrapped but does not switch into the running state as shown in figure 3.3 b). These phase slips cause a finite voltage in the trapped state. Phase diffusion becomes more likely with higher applied currents and the slope in this regime is quantified by the **phase-diffusion conductance** $G_{\mathbf{PD}}$. The overdamped junction shows no hysteresis as the particle's inertia in the running phase is overcome by the damping as soon as potential maxima appear. This is shown by the red curve in figure 3.4.

Frequency-dependent damping

In some V(I)Cs both hysteresis and a finite slope in the trapped state are observed. This behaviour can be understood by frequency dependent damping as has been explained by R. L. Kautz and J. M. Martinis [81]. They treat the case in which the Josephson energy is much larger than the charging energy ($E_J >> E_C$) and the main noise contribution is due to thermal noise so that macroscopic quantum tunneling and single electron tunneling process can be excluded. Phase diffusion is a process that occurs at high frequencies that are close to the plasma frequency ω_p which usually is in the order of microwaves. The steady motion of the phase particle

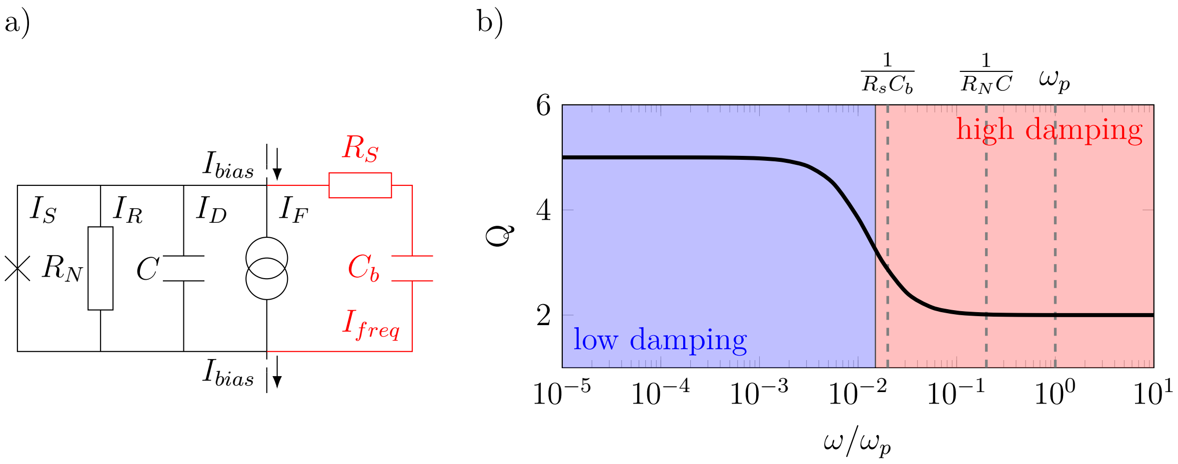

Figure 3.5: Frequency dependent damping can be implemented in the RCSJ model by the addition of a frequency dependent shunt. In a) the standard RCSJ model circuit is shown in black with the addition of an RC term which is shown in red. With this addition the quality factor Q can change for different frequencies as shown in b). The plot follows equation 3.20 with $Q_0 = R_N C \omega_p = 5$ so that $R_N C = \omega_p/5$ and $Q_1 = 2$. The ratio $\rho = R_N C / R_S C_b = 0.1$ was assumed. Graph and values from [81].

down the washboard potential in the running state which governs the hysteresis of the V(I)Cs occurs at very low frequencies close to zero. The damping of the junction is determined by the junction resistance. Frequency-dependent damping is implemented in the RCSJ model by the addition of a frequency-dependent shunt in the form of an $\mathrm{R}_S\mathrm{C}_b$-element to the circuit shown in red in figure 3.5 a). For low frequencies C_b behaves as open circuit and the damping depends solely on R_N so that the quality factor Q_0 is given by equation 3.19. At high frequency C_b behaves as a shunt and the parallel resistance R_S is included in equation 3.19 so that $Q_1 = (\frac{1}{R_N} + \frac{1}{R_S})^{-1} C\omega_p$. The frequency dependent quality factor is introduced in [81] which includes the effect of the additional capacitance C_b and resistance R_S by the ratio $\rho = R_N C / R_S C_b$

$$Q(\omega) = Q_0 \frac{1 + \frac{Q_0^2}{\rho^2}(\frac{\omega}{\omega_p})^2}{1 + \frac{Q_0^3}{Q_1 \rho^2}(\frac{\omega}{\omega_p})^2}. \tag{3.20}$$

In figure 3.5 b) the quality factor is plotted for an exemplary junction. At the plasma frequency ω_p the damping is high (Q is small) and for frequencies lower than $\frac{1}{R_S C_b}$ the damping can be much smaller (Q is large). R. L. Kautz and J. M. Martinis showed in their calculations that this leads to phase diffusion and hysteresis in the V(I)Cs of junctions in the given parameter space [81].

I_{C}	ideal critical current	Maximum current the junction can sustain in the absence of noise.	$I_C = \frac{\pi}{2e}\frac{\Delta}{R_N}\tanh(\frac{\Delta(T)}{2k_BT})$
I_{sw}	switching current	Transition from the low-voltage to the high-voltage branch in the presence of noise.	measured in experiments
I_{re}	retrapping current	Transition from the high-voltage to the low-voltage branch in the presence of noise.	measured in experiments, $I_{\mathrm{re}} = \frac{4I_C}{\pi Q}$
G_{PD}	phase-diffusion conductance	Conductance due to phase slips in the washboard potential in the low-voltage branch.	measured in experiments
ω_p	plasma frequency	Oscillation of the trapped quasiparticle around equilibrium.	$\omega_p = \sqrt{\frac{2e}{\hbar}\frac{I_C}{C}}$
ω_J	Josephson frequency	Ac current response to an applied dc voltage.	$\omega_J = \frac{2e}{\hbar}V_{dc}$
ω_{RC}	RC-frequency	Timescale of the RC-element of the RCSJ circuit.	$\omega_{RC} = \frac{1}{R_NC}$
β_C	Stewart-McCumber parameter	Measure for the damping of the Josephson junction.	$\beta_C = \frac{2e}{\hbar}I_CR_N^2C$
Q	quality factor	Measure for the damping of the Josephson junction.	$Q = \frac{\hbar}{2e}\sqrt{\beta_C} = \omega_pR_NC$
E_J	Josephson energy	Height of the potential barrier that needs to be overcome for the junction to switch in the running state.	$E_J = \frac{\hbar}{2e}I_C$
E_C	charging energy	Energy scale of the capacitive term of the RCSJ model. C largely determines the inertia of the phase particle.	$E_C = \frac{2e^2}{C}$
E_{th}	Thermal energy	Thermal activation energy of the phase particle.	$E_{th} = k_BT$

Table 3.1: Properties of a Josephson junction.

3.2 Incoherent Cooper-pair tunneling

The tunneling processes in STM Josephson junctions are strongly influenced by external noise due to their strong coupling to the environment. The coupling of the junction to the environment depends on the biasing method of the junction as will be shown in chapter 6. There are three energy scales affecting the tunneling processes in Josephson junctions:

$$\begin{aligned} \text{Josephson energy:} \qquad E_J &= \frac{\hbar}{2e} I_C \\ \text{Thermal energy:} \qquad E_{th} &= k_B T \\ \text{Charging energy:} \qquad E_C &= \frac{2e^2}{C}. \end{aligned} \tag{3.21}$$

So far mostly coherent Cooper-pair tunneling was discussed where the phase difference across the junction is stable and does not change significantly during the tunneling process. Coherent Cooper-pair tunneling occurs in the strong coupling regime when the charging energy is much smaller than the Josephson energy ($E_J >> E_C$). Strongly overdamped junction may experience phase diffusion in the presence of noise, e.g. thermal fluctuations when $E_{th} \approx E_J$. Phase diffusion is observed in the presence of energy dissipation and a finite voltage drop in the Cooper-pair tunneling regime of the junction occurs [74, 82].

Incoherent Cooper-pair tunneling exists in the weak coupling regime ($E_J << E_C$) [47]. It can be understood as a process, where Cooper pairs break and the individual electrons tunnel to form a new Cooper pair on the other electrode. In that case, the Cooper-pair transport is dominated by charging effects in the so called dynamical Coulomb blockade regime. In this regime Cooper pairs tunnel sequentially and exchange excess energy with the environment via photons [47]. This interaction can be described by P(E)-theory which is described below [46].

In the Coulomb blockade regime the junction is well coupled to the environment which is the case if $\rho = \frac{R_{\text{vac}}}{R_Q} << 1$, where ρ is the ratio of the vacuum impedance R_{vac} and the quantum of resistance R_Q. The limit for the Coulomb blockade regime is given by [74, 82–84]:

$$\frac{E_C}{E_J}\frac{1}{\rho^2} >> \frac{E_C}{E_{th}}\frac{1}{\rho}. \tag{3.22}$$

The phase coherence of the Cooper pairs is affected by noise and also by the biasing method. Applying a voltage prevents phase coherence and Cooper-pair tunneling is only possible sequentially. With an applied current the phase dynamics may still be influenced by external influences but they are not explicitly driven. With increasing noise fluctuations the energy scales change and the two regimes meet when E_J becomes comparable to E_C. Phase coherence gradually declines until Cooper pairs tunnel sequentially.

P(E)-theory

In ultrasmall tunneling junctions with small capacitances of $C < 10^{-15}$ F charging effects dominate the transport through the junction, i.e. $E_C >> E_{th}$. P(E)-theory is derived for these junctions and is based on probability functions that describe the coupling of the system to the environment via an impedance. A description of this theory is found in Gert-Ludwig Ingold and Yu. V. Nazarov [46]. In a tunnel junction that is biased by a voltage source the environmental impedance is governed by the leads to the junction. It can be modelled by an inductance and/or resistance in the bias line with a capacitive coupling to ground (see figure 3.6 a)). The capacitance may act as voltage source when charged by a dc bias source. The circuit shown in figure 3.6 a) containing a superconducting junction follows the description of G.-L. Ingold and Y. V. Nazarov [46] and A. Steinbach *et al.* [85]. If the wire impedance is dominated by the RC-component with no significant inductance, the

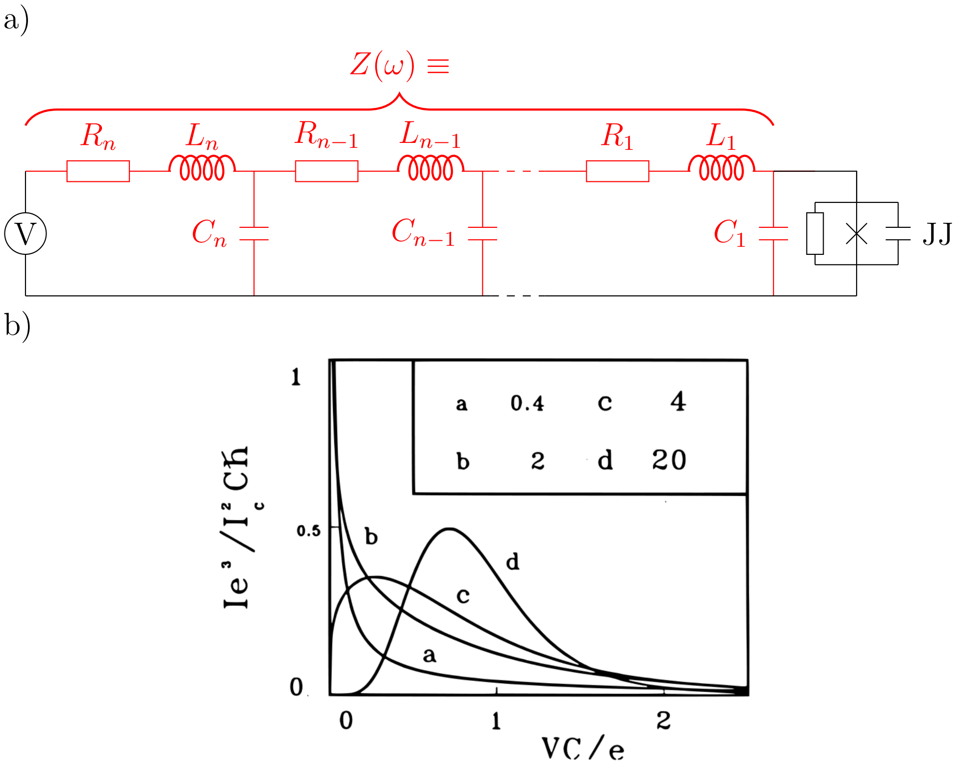

Figure 3.6: P(E)-theory for Josephson junctions. a) shows the equivalent circuit for a Josephson junction with a frequency-dependent impedance modelling the transmission lines as described in [46, 81, 85]. b) I(V) curves as calculated by P(E)-theory with an ohmic impedance (neglecting inductance) for different resistor values (a-d) given in kΩ. For low impedance the current peak is located sharply at zero voltage and shifts towards higher energies with increasing impedance [46]. Figure 3.6 b) is reproduced with permission from Springer Nature.

total inductance is given by $Z(\omega)^{-1} = R_W^{-1} + jC_W\omega$. Here R_W and C_W are the total resistance and capacity of the wires in the setup. In figure 3.6 a) the circuit is further subdivided into R_n and C_n components of the the wires.

Details on calculating tunneling currents and extracting the density of states in STM experiments are given in chapter 4. Here we calculate tunneling rates with perturbation theory, focussing on charging effects and phase-phase correlation. The Hamiltonian of this tunneling junction with the described equivalent circuit is given by

$$H = H_{qp} + H_{\mathrm{env}} + H_T \tag{3.23}$$

[46]. $H_{qp} = \sum_{k\sigma}(\epsilon_k + eV)c^\dagger_{k,\sigma}c_{k,\sigma} + \sum_{q\sigma}\epsilon_q c^\dagger_{q,\sigma}c_{q,\sigma}$ corresponds to the quasiparticle Hamiltonian. k and q correspond to wave vectors with energies $\epsilon_{q/k}$. $c^\dagger_{k,\sigma}$ and $c_{k,\sigma}$ are the annihilation and creation operators for quasiparticles with wave vector k and spin σ. The H_{env} captures the details of the impedance of the environment. Finally the tunneling Hamiltonian $H_T = \sum_{kq\sigma} T_{kq}c^\dagger_{q\sigma}c_{k\sigma}e^{i\phi} + H.c.$ takes the coupling of the two electrodes into account via the tunneling matrix element T_{kq}. The addition of the phase operator $e^{i\phi}$ takes a change of the charge of the junction into account. More details can be found in [46]. For weak coupling of the two electrodes H_T can be treated as a perturbation to calculate tunneling probabilities.

Due to charging effects additional reservoir states $|R\rangle$ are generated by the environment. The initial and final state of the junction are given by $|i\rangle = |E\rangle|R\rangle$ and $|f\rangle = |E'\rangle|R'\rangle$, respectively. $|E\rangle$ are the quasiparticle states at energy E. By means of Fermi's golden rule tunneling rate are derived as follows:

$$\begin{aligned}
\overrightarrow{\Gamma}_{i\to f} =& \frac{2\pi}{\hbar}|\langle f|H_T|i\rangle|^2\delta(E_i - E_f)\\
\overrightarrow{\Gamma}(V) =& \frac{2\pi}{\hbar}\int_{\infty}^{\infty} d\epsilon_k d\epsilon_q \sum_{kq\sigma}|T_{qk}|^2 f(\epsilon_k)(1 - f(\epsilon_q))\cdot\\
&\sum_{R,R'}|\langle R|e^{i\phi}|R\rangle|^2 P_\beta(R)\delta(\epsilon_k + eV + E_R - \epsilon_q - E_{R'})
\end{aligned} \tag{3.24}$$

$f(\epsilon)$ are Fermi distribution functions and $P_\beta(R)$ is the probability function of finding the reservoir state E at the inverse thermal energy $\beta = (k_BT)^{-1}$. For details of the derivation see [46]. This result is in accordance with chapter 4 where charging is neglected.

The probability function of finding the initial reservoir state $|R\rangle$ is given by

$$P_\beta(R) = \langle R|\rho_\beta|R\rangle = Z_\beta^{-1}\langle R|e^{-\beta H_{\mathrm{env}}}|R\rangle \tag{3.25}$$

with the equilibrium density matrix of the reservoir

$$\rho_\beta = Z_\beta^{-1}\exp(-\beta H_{\mathrm{env}}) \tag{3.26}$$

and the partition function of the environment at thermal equilibrium

$$Z_\beta = \mathrm{Tr}(\exp(-\beta H_{\mathrm{env}})) \tag{3.27}$$

Continuing the calculation of the tunneling rates using this equation leads to the conclusion that the reservoir part of the equation boils down to a phase-phase correlation term:

$$Z_\beta^{-1} \sum_R \langle R| e^{i\phi(t)} e^{i\phi(0)} e^{-\beta H_{\mathrm{env}}} |R\rangle = \langle e^{i\phi(0)} e^{i\phi(t)} \rangle = e^{\langle(\phi(t)-\phi(0))\phi(0)\rangle} = e^{J(t)}. \tag{3.28}$$

Here, the phase-phase correlation function $J(t) = \langle(\phi(t) - \phi(0))\phi(0)\rangle$ is introduced which contains information of the junction's coupling to the environmental impedance. The Fourier transform of this function gives the probability function

$$P(E) = \frac{1}{2\pi\hbar} \int_{\infty}^{\infty} dt \exp(J(t) + \frac{i}{\hbar} Et). \tag{3.29}$$

This simplifies the tunneling rate formula to

$$\overrightarrow{\Gamma}(V) = \frac{1}{eR_T} \int_{\infty}^{\infty} dE dE' f(E)(1 - f(E' + eV))P(E - E')), \tag{3.30}$$

where R_T is the resistance of the tunneling junction. [46]
P(E)-theory is derived from perturbation theory and holds for any ultra small metal-insulator-metal tunneling junction. Translating this model to Josephson junctions requires some adjustments. Another energy scale, namely the Josephson energy E_J becomes relevant for the tunneling of Cooper pairs. Josephson junction can be weakly ($E_J << E_C$) or strongly coupled ($E_J >> E_C$). The first case may be treated with P(E)-theory. For small voltages and low temperatures quasiparticle excitations can be neglected. The Hamiltonian for this systems becomes

$$H = H_{\mathrm{env}} + H_{CP} = H_{\mathrm{env}} + E_J \cos(2\phi) = H_{\mathrm{env}} + E_J/2e^{-2i\phi} + H.c. \tag{3.31}$$

The operator $e^{-i\phi}$ for single charge transfer translates into $e^{-2i\phi}$ for the tunneling of two charges. The tunneling rates for Cooper pairs can be calculated as previously with $\frac{E_J}{2} e^{-2i\phi}$ as perturbation, leading to the tunneling rate:

$$\overrightarrow{\Gamma}(V) = \frac{\pi}{2\hbar} E_J^2 \sum_{R,R'} | \langle R| e^{-2i\phi} |R\rangle |^2 P_\beta(R) \delta(E_R - E_{R'}) \tag{3.32}$$

This finally leads to the probability function for tunneling Cooper pairs:

$$P'(E) = \frac{1}{2\pi\hbar} \int_{\infty}^{\infty} dt \exp(4J(t) + \frac{i}{\hbar} Et). \tag{3.33}$$

So that the forward tunneling rate becomes:

$$\overrightarrow{\Gamma}(V) = \frac{\pi}{2\hbar} E_J^2 P'(2eV) \tag{3.34}$$

The supercurrent through the junction is determined by the forward and backward tunneling rates as follows:

$$I_S(V) = 2e(\overrightarrow{\Gamma}(V) - \overleftarrow{\Gamma}(V)) = \frac{\pi e E_J^2}{\hbar}(P'(2eV) - P'(-2eV)) \tag{3.35}$$

As these results are derived from perturbation theory the Josephson energy needs to be small. [46]
The environment impedance is modelled by the phase-phase correlation function J(t). Modelling the impedance of the environment is therefore crucial for modelling the expected behaviour of voltage-biased Josephson junction. Depending on the impedance that is coupled to the Josephson junction the probability function $P(2eV)$ shows different characteristics as depicted in figure 3.6 b). For low impedance the I(V)-characteristics of the junction is peaked sharply at zero energy. A higher impedance shifts the peak of the function to higher energies up to the charging energy E_C [46]. For the presented curves RC-transmission lines were used neglecting inductances.

3.3 Photon-assisted tunneling and Shapiro steps

In the previous chapter the concept of incoherent Cooper-pair tunneling in voltage-biased Josephson junctions was discussed. In chapter 6 voltage- and current-biased Josephson junctions are found to couple differently to the electromagnetic environment. In current-biased junctions the observed hysteresis indicates phase coherence across the Josephson junction. When exposed to high frequency (HF) irradiation Josephson junctions are able to absorb energy from the field. The absorption mechanism depends on the coherence of the tunneling Cooper pairs and the coupling of the junction to the environment. In response to the irradiation, steps occur in the V(I)Cs of a Josephson junction. The number of steps increases with increasing irradiation amplitude while the their energy spacing is determined by the frequency. If the steps originate from Cooper pairs that incoherently absorb or emit photons from the environment the process is called **photon-assisted tunneling**. If the electromagnetic field is treated as an ac modulation to the applied bias in the framework of the RCSJ model the time dependent Josephson phase is excited resonantly while it is moving down the washboard potential. The resulting coherent features are called **Shapiro steps**. Shapiro steps are treated differently in current- or voltage-biased junctions. Even though, the incoherent absorption or emission of photons occur at the same energy as Shapiro steps, the exact shape of the features is expected to differ slightly according to the theoretical description.

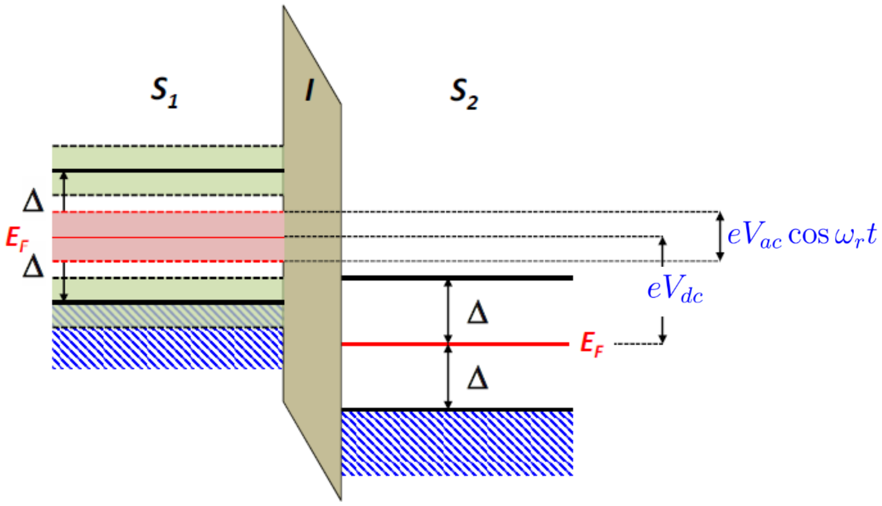

Figure 3.7: P. K. Tien and J. P. Gordon approach to photon-assisted quasiparticle tunneling. The energy levels of one electrode are shifted with respect to the other electrode by the HF irradiation. The absorption of photons from the electromagnetic environment is quantized. The amplitude V_{ac} of the irradiation determines the number of photons that can be absorbed during the tunneling process. The frequency of the irradiation sets the size of the energy steps at which the absorption occurs. Graphic from [77].

Photon-assisted tunneling

Photon-assisted tunneling describes the process of the absorption or emission of photons to an electromagnetic environment while tunneling from one electrode to the other. The tunneling particle can absorb or emit photons with the energy $\hbar\omega_r$, where ω_r is the radial frequency of the applied irradiation. The number of photons n that can be absorbed during the tunneling process is determined by the amplitude of the applied radiation V_{ac} so that $n\hbar\omega_{\mathrm{r}} < eV_{\mathrm{ac}}$.

In figure 3.7 the tunneling process is schematically illustrated as suggested by P. K. Tien and J. P. Gordon [49]. The applied dc voltage is modulated by an ac signal. To simplify, it is assumed that the modulation does not change the energies levels within the electrodes but only the relative position across the tunnel barrier. By varying the energy levels $E_n = E_{qp} + eV_{ac}\cos(\omega_{\mathrm{r}} t)$ the resulting current steps can be expanded by a Bessel function so that:

$$I(t) = \sum_{n=-\infty}^{+\infty} J_n^2\left(\frac{eV_{\mathrm{ac}}}{\hbar\omega_{\mathrm{r}}}\right) I_{qp}^0\left(V + \frac{n\hbar\omega_{\mathrm{r}}}{e}\right) \tag{3.36}$$

This model has been successfully applied to the splitting of the superconducting coherence peak in a superconductor-superconductor junction where current steps occur at voltages of $V_n = \frac{n\hbar\omega_r}{e}$ [52, 86].

For Cooper-pair tunneling the model has been adjusted to reproduce the splitting of the Josephson peak in a dI/dV spectrum of a voltage-biased junction [50, 51]. It assumes that instead of single electrons with charge e, pairs of electrons with a charge of $2e$ tunnel. In that case the steps occur at $V_n = \frac{n\hbar\omega_r}{2e}$ which corresponds to half the energy intervals compared to single electron tunneling and the number of absorbed n is accordingly determined by $n\hbar\omega_r < 2eV_{ac}$. The tunneling current can be described by:

$$I(t) = \sum_{n=-\infty}^{+\infty} J_n^2\left(\frac{2eV_{ac}}{\hbar\omega_r}\right) I_{qp}^0\left(V + \frac{n\hbar\omega_{\mathrm{r}}}{2e}\right) \tag{3.37}$$

These steps do not directly translate into Shapiro steps as there is no correlation with the phase change across the junction.

Voltage-biased Shapiro steps

Shapiro steps are resonant features in Josephson junctions caused by an ac bias modulation that matches the time evolution of the phase. The phenomenon needs to be treated individually for a voltage or a current bias.

The dc voltage bias in combination with an ac voltage modulation is discussed following the argumentation of chapter 12.1 of the textbook *'Fundamentals and Frontiers of the Josephson Effect'* [74] and the lecture notes of A. Marx and R. Gross [77]. Using the second Josephson equation (eq. 3.4) for dc voltage that is modulated by V_{ac} with the angular frequency ω_{r} results in

$$V = V_{\mathrm{dc}} + V_{\mathrm{ac}} \cdot \cos(\omega_{\mathrm{r}} t) = \frac{\hbar}{2e}\frac{d\phi}{dt}. \tag{3.38}$$

The time dependent phase difference becomes

$$\phi(t) = \frac{2e}{\hbar} \cdot (V_{\mathrm{dc}} t + \frac{V_{\mathrm{ac}}}{\omega_{\mathrm{r}}} \cdot \sin(\omega_{\mathrm{r}} t)) + \phi_0). \tag{3.39}$$

With the first Josephson equation (eq. 3.1) the current can be expanded by Bessel functions and results in

$$I(t) = I_C \sum_{n=-\infty}^{+\infty} (-1)^n \frac{\hbar}{2e}\frac{V_{\mathrm{ac}}}{\omega_{\mathrm{r}} t} J_n(\frac{2eV_{\mathrm{ac}}}{\hbar\omega_{\mathrm{r}}}) \sin((\frac{2e}{\hbar} V_{\mathrm{dc}} - n\omega_{\mathrm{r}})t + \phi_0). \tag{3.40}$$

Resonance conditions are met when $\frac{2e}{\hbar} V_{\mathrm{dc}} = n\omega_{\mathrm{r}}$ which results in a step in the I(V)Cs at

$$V_{\mathrm{dc}n} = n\frac{\hbar\omega_{\mathrm{r}}}{2e}. \tag{3.41}$$

These conditions correspond to the ac driving frequency matching the Josephson frequency ω_J (eq. 3.7) that is caused by the applied dc voltage. At $V_{\mathrm{dc}n}$ the supercurrent is ambiguous and can take values between $I_{qp} \pm I_C J_n(n\frac{V_{\mathrm{ac}}}{V_{\mathrm{dc}}})$ as

$$|I_n(V_{\mathrm{ac}})| = I_C |J_n(n\frac{V_{\mathrm{ac}}}{V_{\mathrm{dc}}})|. \tag{3.42}$$

In experiments the Josephson junctions switch out of the Cooper-pair tunneling regime at currents far below the critical current of the junction due to noise. The in-gap conductance (below $eV = 2\Delta$) of the junction is taken into account in equation 3.36 by the irradiation-free quasiparticle current I_{qp}^0. At high normal state conductances this quasiparticle current is additionally affected by multiple Andreev reflections that occur within the superconducting gap.

Current-biased Shapiro steps

For a Josephson junction that is driven by an ideal current source which is modulated by HF irradiation the applied current is described as follows [59, 77]

$$I(t) = I_{\mathrm{dc}} + I_{\mathrm{ac}} \sin(\omega_{\mathrm{r}} t). \tag{3.43}$$

Using this in the RCSJ equation 3.13 described in chapter 3.1 the differential equation becomes

$$I_{\mathrm{dc}} + I_{\mathrm{ac}} \sin(\omega_{\mathrm{r}} t) = I_{\mathrm{C}} \sin\phi + \frac{\hbar}{2eR}\frac{d\phi}{dt} + \frac{\hbar}{2e} C \frac{d^2\phi}{dt^2}. \tag{3.44}$$

Figure 3.8 illustrates the effect of the HF irradiation on the phase particle in the washboard potential. Figure 3.8 a) shows the steps in the V(I)C as expected for a current-biased overdamped Josepshon junction under HF irradiation in the absence of noise. The ac component modulates the tilt of the washboard potential with its frequency ω_r and an amplitude of I_{ac}. Even at zero bias this modulation can be seen as a resonant excitations as the phase particle may resonantly jump back and forth between minima (figure 3.8 b)). As the current increases the washboard potential tilts further. If the particle is running down the potential landscape a resonance is met when the Josephson frequency matches the irradiation frequency. the condition $V_n = n\frac{\hbar\omega_r}{2e}$ is met with $n = 1$ when the time that elapses while the phase particle overcomes one period of the potential corresponds to the frequency of the irradiation (shown in figure 3.8 c)). As the tilt of the washboard potential increases the phase particle becomes faster until it reaches the next resonant condition at $n = 2$. Here the particle overcomes two periods of the washboard potential with a frequency that matches the external irradiation as shown in 3.8 d).

This implies that the phase particle moves with a finite velocity in the washboard potential picture. That means that when no voltage drop occurs at the junction the particle cannot be excited to resonances with $n > 0$. The behaviour of the junction is highly influenced by its damping which will be discussed in detail in chapter 7. The overdamped junction is not expected to show Shapiro steps before switching conditions are reached earliest at $I_{dc} = I_{sw} - I_{ac}$ as shown in the inset in figure 3.8 a). When noise causes phase diffusion a finite voltage can be measured in the low-voltage branch of the junction and can cause resonant excitations. The situation is different for the underdamped junction. Since the phase particle does not experience damping several resonances are available to the phase particle for the same current bias. This results can result in zero crossing steps, where a positive voltage is measured for a negative applied current and vice versa. The particle can move within any of the resonances dissipation free. The order of the resonance depends on the history of the system. This is often discussed in the context of a voltage standard and realized in specifically designed Josephson junction arrays [6, 87, 88].

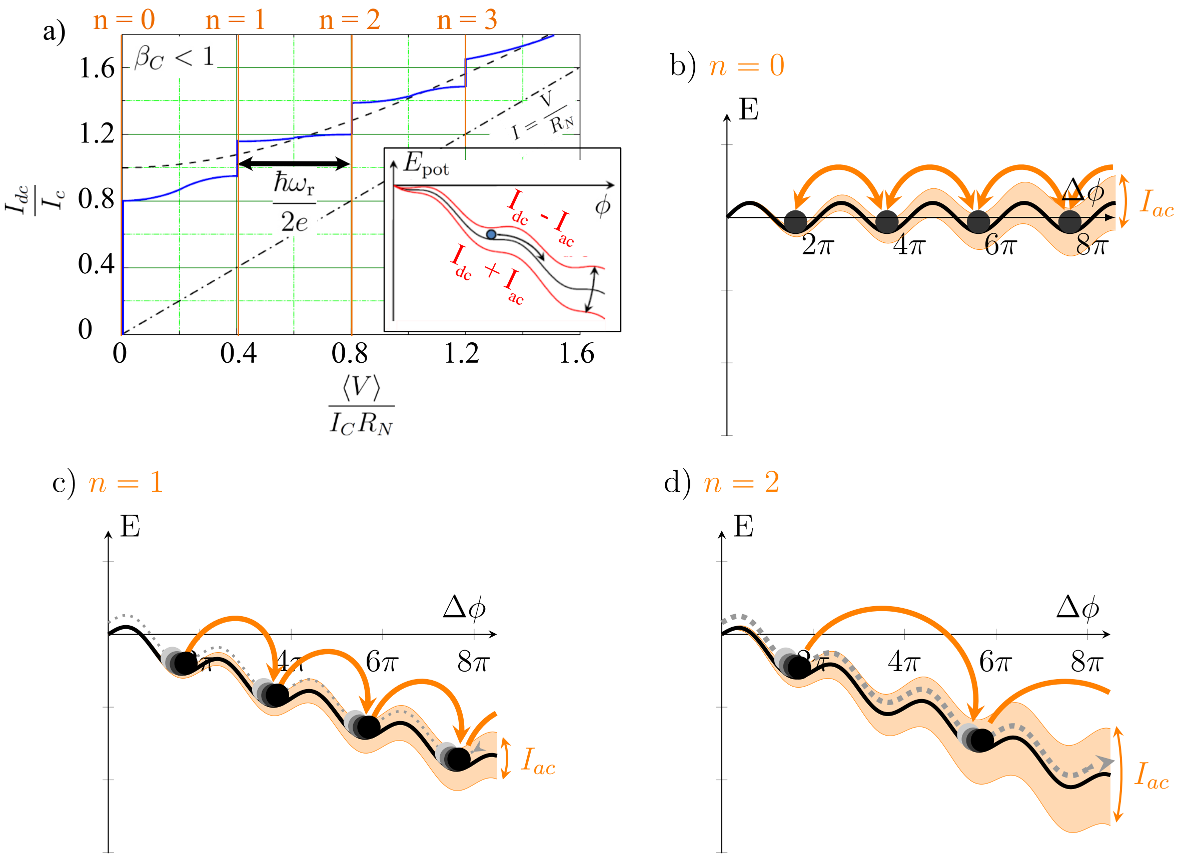

Figure 3.8: Shapiro steps in a washboard potential with a current modulation of $I(t) = I_{dc} + I_{ac} \sin \omega_r t$. a) shows the Shapiro steps in the V(I)C as expected in a noise-free overdamped Josephson junction. b) shows the resonance at zero bias for $n = 0$. The phase particle has no preferential direction but jumps in both directions. Adapted from [77]. c) shows the resonance at $n = 1$ at a finite tilt. The phase particle is resonantly excited over one period of the potential. d) shows the resonance at $n = 2$ where the particle is excited over two periods of the potential.

3.4 Superconducting diode effect

In chapter 8 the effect of single magnetic adatoms on the properties of a Josephson junction is investigated. A non-reciprocity of the retrapping currents is observed in these junctions. The diode-like behaviour of the investigated STM Josephson junctions is found to originate from asymmetric damping properties. Non-reciprocal transport in Josephson junctions has previously been observed in so called Josephson diodes. In these junctions the critical currents become asymmetric which is caused by the superconducting diode effect. The superconducting diode effect and its consequences for Josephson junctions are described in this chapter, to be able to differentiate this effect from the origin of the non-reciprocity in the investigated Josephson junctions,

The superconducting diode effect occurs in material system where inversion and time-reversal symmetry is broken. The critical currents of superconductors that experience the superconducting diode effect depend on the current bias direction. In Josephson junctions this phenomenon results in an asymmetry of the current-phase-relation (CPR) and the effect is observed in non-reciprocal behaviour of the critical currents of the Josephson junction. Josephson junctions experiencing this non-recirpocity are called Josephson diode. Here, first the physical origin of the superconducting diode effect will be explained, before the consequences for Josephson junctions are discussed.

The superconducting diode effect was observed by F. Ando *et al.* [12] d by transport measurements on a superconducting Nb/Ta/V multilayer device in the presence of an external magnetic field perpendicular to the current direction. In this system the critical current depends on the polarity of the current bias and it is possible to switch between the superconducting and resistive state by inverting the direction of the current flow or the direction of the applied magnetic field. This non-linear effect is correlated to simultaneously breaking inversion symmetry and time reversal symmetry. In the system presented by F. Ando *et al.* [12] inversion symmetry is broken by strong Rashba spin-orbit coupling (SOC) in the multilayer stack. Time reversal symmetry is broken by the external magnetic field.

Rashba SOC results in concentrical Fermi surfaces as shown in figure 3.9 a). The spin of the electrons are orthogonal to their wavevectors k so that the spin points in opposite directions for opposite momenta $\sigma(k) = -\sigma(-k)$. In a s-wave superconductor Cooper pairs are formed by electrons with opposite spin and momentum. The Fermi surfaces in figure 3.9 b) show that singlet Cooper pairs consist of electrons on opposite sides of the Rashba cones. In the absence of an external magnetic field the total momentum of the pairs is zero.

The external magnetic field breaks time reversal symmetry in that system by the Zeeman-splitting of the spin states. The two Fermi surfaces shift in opposite directions so that they are no longer centrosymmetric around the same center (see figure 3.9 b)). The energy of the particles become momentum dependent $E(k) \neq E(-k)$

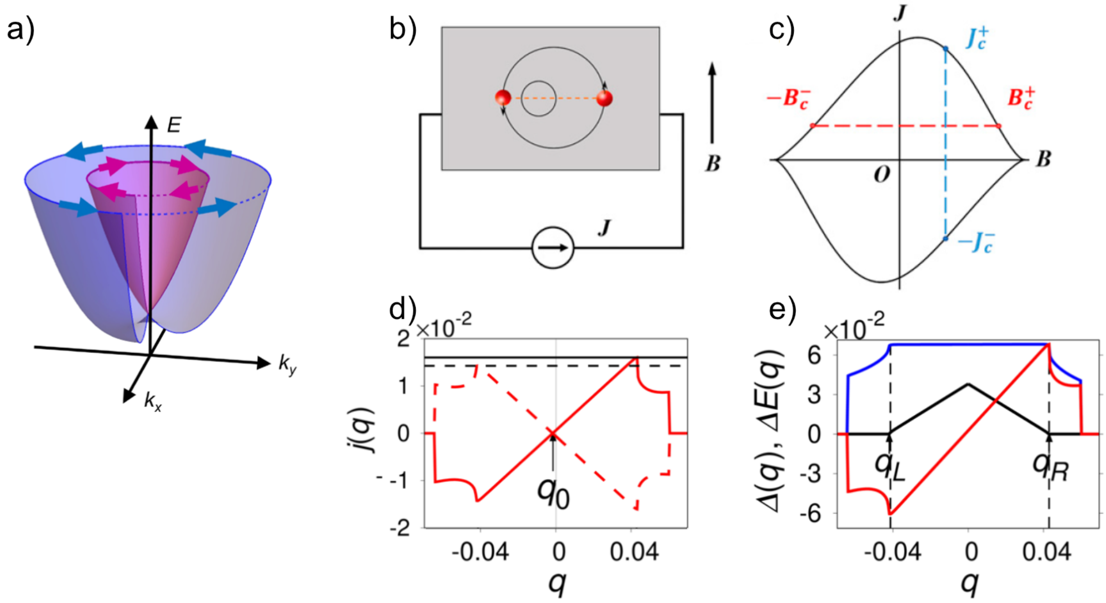

Figure 3.9: The superconducting diode effect in a system where inversion symmetry is broken by Rashba spin orbit coupling and time reversal symmetry is broken by an external magnetic field. In a Rashba system the spin and the momentum are coupled and the Fermi surfaces for the different spin states are shown in a) [89]. b) shows the Zeeman shift of the concentrical Fermi surfaces of the Rashba system in the presence of an applied magnetic field [14]. In c) the phase diagram of the critical current density and critical magnetic field is shown [14]. The curve is slightly skewed so that for the same B-field values different critical current densities are observed depending on the direction of the applied current. d) and e) show the current density in dependence of the Cooper-pair momentum q that is slightly shifted by q_0 in red [13]. Due to this shift the left and right critical Landau momenta (q_L and q_R) are reached for different current densities as indicated by the solid and dashed black line in d) [13]. In e) additionally the coupling energy Δ (blue) and the quasiparticle excitation gap $E(q)$ (black) are shown [13].
Reprinted figure 3.9 d) and e) with permission from [Akito Daido, Yuhei Ikeda, and Youichi Yanase, Physical Review Letters, 128, 037001 2022.] Copyright 2022 by the American Physical Society.

which breaks time reversal symmetry.

Physically this corresponds to Cooper pairs that have a finite momentum q_0 without an applied current. This effect is called helical superconductivity in which an external magnetic field modulates the phase of the order parameter in space $\Delta(r) = \Delta_0 e^{(iq_0 r)}$ [14].

Breaking inversion and time reversal symmetry gives rise to magnetochiral anisotropy

$$R = R_0(1 + \gamma(B \times z) \cdot I). \tag{3.45}$$

This leads to a non-reciprocity of the resistance depending on the direction of the current and magnetic field. γ is the anisotropy parameter which is determined by the Rashba SOC strength.

The diode effect for temperatures close to T_C can be explained by an asymmetry in the Ginzburg-Landau free energy as has been shown by N. F. Q. Yuan *et al.* [14] and as presented in figure 3.9 b) and c). For low temperatures the asymmetry has been derived microscopically by an asymmetry of the Landau critical momenta [13].

An intuitive way of understanding the superconducting diode effect as a result of helical superconductivity is given by the theoretical description of A. Daido *et. al.* [13]. Applying a current to a superconductor provides a finite momentum q along the biasing direction to the Cooper pairs. The Landau critical momentum corresponds to the maximum momentum of the Cooper pairs before breaking superconductivity. Accordingly, the critical current of the material corresponds to the Landau critical momentum at which the kinetic energy of the Cooper pairs breaks the superconducting state. In the case of helical superconductivity, the relation of the current density to the momentum $j(q)$ is shifted by q_0 as shown in figure 3.9 d) and e). The Landau critical momentum is reached for different current bias values depending on the direction of the momentum shift q_0. For that reason, the superconducting diode effect is assumed to be a probe of helical superconductivity [12–14].

Non-reciprocal transport in noncentrosymmetric superconductors caused by the magnetochiral effects has already been observed in 2017 by Y. S. Ryohei Wkatsuki *et al.* [90] and a theoretical description followed a year later [91]. L. Bauriedl *et al.* [92] observed the superconducting diode effect in few layers of $NbSe_2$ and explored the influence of different magnetic field directions on the effect. J.-X. Lin *et al.* [93] investigated the superconducting diode effect in twisted trilayer graphen at zero magnetic field. The sign of the diode effect could be reversed by changing the polarity of an out-of-plain magnetic field that was used for priming the material prior to the measurement. A theoretical description of these zero-field superconducting diodes was given by Scammel *et al.* [94]. J. Yun *et al.* [95] showed the superconducting diode effect in van der Waals superconductor-ferromagnet heterostructures consisting of $NbSe_2$ and $CrPS_4$. Time reversal symmetry is broken by the magnetic proximity effect caused by the magnetic $CrPS_4$ layer. Ferroelectric superconductors such as Cu intercalated $NbSe_2$ layers have been proposed to control the superconducting diode effect by reversibly switching their ferroelectric properties by B. Zhai *et al.* [96]. A phenomenological theory of the superconducting diodes has been derived by J. J. He *et al.* [97]. They described Rashba SOC systems with an external magnetic field by a generalized Ginzburg-Landau method and achieved an analytical description of the experimental findings.

Josephson diode effect

Non-reciprocal critical currents are observed in Josephson junctions in systems for which inversion and time reversal symmetry is broken. The CPR in Josephson junctions becomes asymmetric in the presence of helical superconductivity. In systems with strong SOC and Zeeman coupling an external magnetic field results in a phase shift in the CPR of the Josephson junction. Additionally, higher order harmonics of the sinusoidal dc Josephson equation (eq. 3.1) as considered for short ballistic junctions result in a skewed CPRs. The combination of these two effects results in non-reciprocity of the critical currents with $I(-\phi) \neq -I(\phi)$ as described by A. Costa *et al.* [98].

The skewed CPRs are again a result of helical superconductivity. In [20] M. Davydova *et al.* a Josephson diode was modelled by a normal conducting nanowire crossing a gap between two superconductors. They suggest that the modulation of the order parameter that is associated with the superconducting diode effect induces screening currents at the surface of the superconductors in the presence of an external magnetic field. The normal conducting barrier of the Josephson junction picks up this modulation by the proximity effect. This results in a finite momentum of Cooper pairs across the junction, ie.e helical superconductivity. Andreev bands (see chapter 2.4) that are formed in the normal conducting barrier are now shifted in energy by $\pm v_F q_0$ for left and right travelling charge carriers (electrons and holes), respectively (figure 3.10 a) and b)). From that an highly asymmetric CPR arises with non-reciprocal critical currents (figure 3.10 c)).

C. Baumgartner *et al.* [15] build a Josephson junction array on a 2D superconductor with Rashba spin-orbit coupling. They showed that the magnetochiral anisotropy of the resistance given in equation 3.45 translates into an magnetic anisotropy in the Josephson inductance L_J of the Josephson junction. B. Pal build a Josephson diode from $\mathrm{NiTe_2}$ and observed a large non-reciprocal behaviour of the critical currents in the junction within a weak external magnetic field. Recently, S. Gosh *et al.* [19] realized a Josephson diode at 77 K made from the high-temperature superconductor BSCCO.

Another device has been implemented by H. Wu *et al.* [22] who designed a Josephson diode that is not controlled by an external magnetic field. The time reversal symmetry is suggested to be broken by the physical properties of the barrier which provides an out of plane polarization. The phenomenon is not completely understood and to the best of my knowledge no theoretical description is available at this

point.
To summarize, non-reciprocity in the critical current of a Josephson junction can be caused by Cooper pairs that have a finite momentum at zero bias. For this to occur inversion and time reversal symmetry need to be broken. In this work we focus on the retrapping currents of underdamped Josephson junction. In contrast to the critical current of the junction the retrapping currents are strongly influenced by the damping of the junction. In chapter 8 we show Josephson junctions with broken inversion symmetry resulting in asymmetric damping properties which is sufficient to observe non-reciprocity in the retrapping currents.

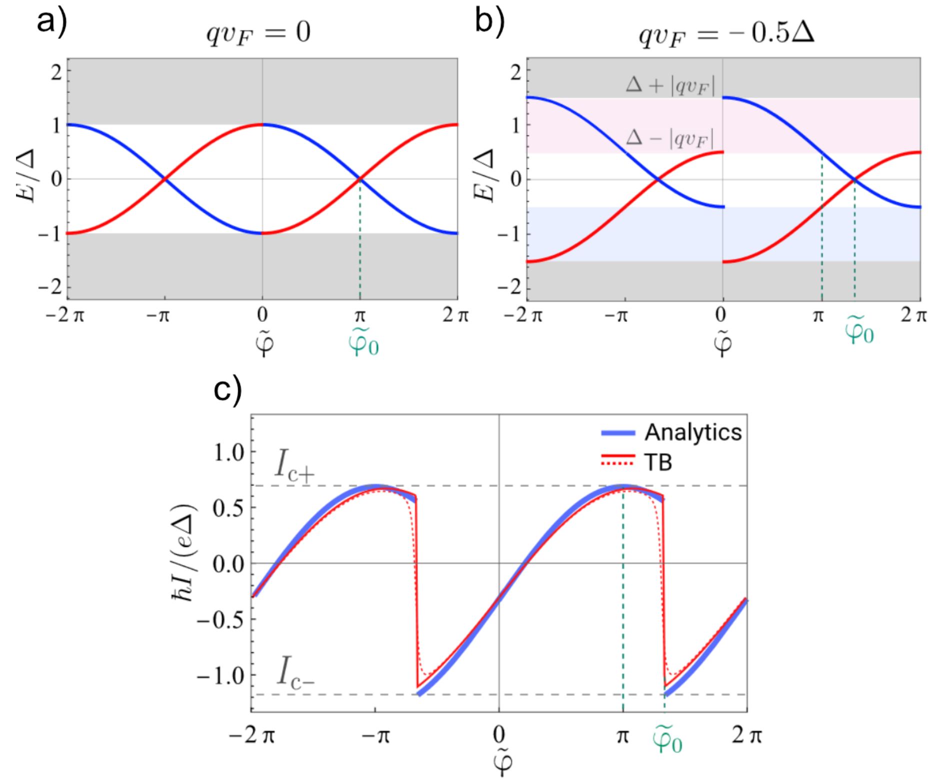

Figure 3.10: Josephson diode effect explained by helical superconductivity. a) shows the Andreev bands for electrons (red curve) and holes (blue curve) with a sinusodial phase dependence. In b) a finite momentum q of the Cooper pairs at zero bias is assumed. The Andreev bands are shifted in energy by $|qv_F|$ in opposite directions for electrons and holes. The simulated CPR is shown in c) where a clear asymmetry of the maximum $|I_{c+}|$ and minimum $|I_{c-}|$ is observed. Graphs from [20]

.

Part II

Experimental methods

CHAPTER 4

SCANNING TUNNELING TECHNIQUES

With a scanning tunneling microscope (STM), surfaces are analysed on the atomic scale. It is not only used for topographical investigations but it is also sensitive to the local electronic structure of the material which is accessible by scanning tunneling spectroscopy (STS). The basic concept consists in quantum tunneling of electrons while scanning the surface with a conductive tip. In this chapter the theoretical basis of scanning tunneling experiments are described and details on the specific methods that were used in this work's experiments are provided. This includes tunneling experiments with superconducting tips and samples as well as the formation of Josephson junctions within an STM. The experimental setup and the procedure of the surface preparation including the deposition of single magnetic adatoms are described.

4.1 Theoretical description of scanning tunneling experiments

Scanning tunneling experiments consist of a conductive tip that is scanned over a conducting surface in close proximity. Energetically the DoS of the tip is separated from the DoS of the surface by an insulating (vacuum) barrier. Quantum mechanically, electrons are described by wavefunctions that exponentially decay into the barrier. If the tip and sample wavefunctions (Ψ_μ and Ψ_ν, respectively) overlap, electrons are able to tunnel through the barrier. To provide a preferential tunnel direction for the electrons that results in a tunneling current, a potential difference between the two electrodes in the form of a bias voltage V_b is applied to the junction. The tunneling probability from a state in the tip at energy E_μ to a state in the sample at E_ν is described by:

$$T_{\mu\to\nu} = \frac{2\pi}{\hbar}|M_{\mu\nu}|^2\delta(E_\nu - E_\mu - eV_b). \tag{4.1}$$

The tunneling matrix element $M_{\mu\nu}$ takes the overlap of the sample and tip wavefunctions into account. The occupation of states is determined by the Fermi distribution function:

$$f(E) = \frac{1}{exp(E - E_F/k_BT) + 1}. \tag{4.2}$$

The tunneling current between tip and sample $I_{t\to s}$ (sample and tip $I_{s\to t}$) is determined by the sum of all transitions between available occupied and unoccupied states:

$$\begin{aligned} I_{t\to s} &= \frac{2\pi e}{\hbar} \sum_{\mu\nu} |M_{\mu\nu}|^2 f(E_\mu)(1 - f(E_\nu))\delta(E_\nu - (E_\mu + eV_b)) \\ I_{s\to t} &= -\frac{2\pi e}{\hbar} \sum_{\mu\nu} |M_{\nu\mu}|^2 f(E_\nu)(1 - f(E_\mu))\delta((E_\mu + eV_b) - E_\nu) \end{aligned} \tag{4.3}$$

The tunneling matrix element is considered to be symmetric with respect to the tunneling direction $M_{\mu\nu} = M_{\nu\mu}$ and to depend only on the energy of the two states involved in the tunneling process. Additionally we use $\delta(E_\nu - (E_\mu + eV_b)) = \delta((E_\mu + eV_b) - E_\nu)$. Equation 4.3 can be rewritten by forming the energy integral over the density of state of the tip $\rho_t(E_\mu)$ and sample $\rho_s(E_\nu)$.

$$I = \frac{2\pi e}{\hbar} \int\int dE_\mu dE_\nu |M(E_\mu, E_\nu)|^2 \rho_t(E_\mu)\rho_s(E_\nu)(f(E_\mu) - f(E_\nu))\delta(E_\nu - E_\mu - eV_b) \tag{4.4}$$

Evaluating one of the integrals using the δ function properties and defining $E = E_\nu$ yields:

$$I = \frac{2\pi e}{\hbar} \int dE|M(E)|^2 \rho_t(E - eV_b)\rho_s(E)(f(E - eV_b) - f(E)). \tag{4.5}$$

Considering temperatures close to zero the Fermi-Dirac distribution becomes a step function (Theta function) so that the integral is different from zero only within the given boundaries of the integral:

$$I = \frac{2\pi e}{\hbar} \int_{E_F}^{E_F + eV_b} dE|M(E)|^2 \rho_t(E - eV_b)\rho_s(E). \tag{4.6}$$

The current through a tunneling junction depends on the density of states of the tip and sample as well as the applied bias voltage and the tunneling matrix element. The Tersoff-Harmann model provides a method to evaluate the tunneling matrix element in more detail.

Tersoff-Harmann model

The tunneling matrix element was first described by Bardeen [99] as follows

$$M_{\mu\nu} = \frac{\hbar^2}{2m} \int d\vec{S}(\psi_\mu^* \nabla\psi_\nu - \psi_\nu \nabla\psi_\mu^*). \tag{4.7}$$

The integral is performed over a surface S that separates the probe and sample area and is located in the vacuum. The rest of the term describes a current from one electrode to the other.
For small voltages and low temperatures, tunneling experiments were described by Tersoff and Harmann in 1985 [100]. They derived a model assuming STM tips to be local spherical potential wells at the very apex, where it is closest to the surface.

The wavefunctions for the sample and tip can be expanded as follows:

$$\begin{aligned} \text{Bloch wavefunction for the sample: } \psi_\nu &= \Omega_s^{-\frac{1}{2}} \sum_G a_G e^{(\kappa^2+|\kappa_G|^2)^{\frac{1}{2}} z} e^{i\kappa_G x} \\ \text{Spherical wavefunction for the tip: } \psi_\mu &= \Omega_t^{-\frac{1}{2}} c_t \frac{\kappa R e^{\kappa R}}{\kappa|r-r_0|e^{\kappa|r-r_0|}} \end{aligned} \tag{4.8}$$

$\Omega_{s/t}$ are the surface and probe volume, $\kappa = \frac{\sqrt{2m\Phi}}{\hbar}$ corresponds to the inverse decay length of the wavefunction into the vacuum with Φ being the workfunction of the material.
The sample is described by a Bloch wavefunction with the reciprocal lattice vector $\vec{G}$ and $\kappa_G = \vec{k_\|} + \vec{G}$ the Bloch wave vector. $k_\|$ is the in-plane momentum of the surface state. The spherical tip is modelled with the center of curvature at r_0 and radius R. a_G and c_t are parameters of the order of unity.
Using the equations 4.8 in equation 4.7 results in:

$$M_{\mu\nu} = \frac{\hbar^2}{2m} \frac{4\pi}{\kappa\sqrt{\Omega_t}} \kappa R e^{\kappa R} \psi_\nu(\vec{r_0}) \tag{4.9}$$

The only variable in this equation is given by the sample wavefunction given in 4.8. Consequently the tunneling matrix element shows an exponential dependence on the tip-sample distance:

$$|M_{\mu\nu}|^2 \propto |\psi_\nu(\vec{r_0})|^2 \propto \exp(-2\kappa z). \tag{4.10}$$

The resulting dependence of the tunneling current (eq. 4.6) on the distance z is used in STM experiments to achieve atomically resolved topographic images. κ corresponds to the decay length and depends on the workfunctions of the materials as well as the form of the barrier.

Scanning tunneling spectroscopy (STS)

In equation 4.6 all available energy states up to the applied bias V_b contribute to the measured current by the integral. To use the scanning probe technique for spectroscopy the contribution of the states needs to be resolved in energy. For that purpose the derivative of the tunneling current in equation 4.6 with respect to the applied voltage is formed[1]:

$$\begin{aligned}\frac{dI}{dV_b} = \frac{2\pi e}{\hbar}(e|M_E|^2\rho_t(E_F)\rho_s(E_F + eV) + \\ \int_{E_F}^{E_F+eV_b} dE\frac{\partial|M_E|^2}{\partial V_b}\rho_t(E - eV_b)\rho_s(E) + \\ \int_{E_F}^{E_F+eV_b} dE|M_E|^2\frac{\partial\rho_t(E - eV_b)}{\partial V_b}\rho_s(E) + \\ \int_{E_F}^{E_F+eV_b} dE|M_E|^2\rho_t(E - eV_b)\frac{\partial\rho_s(E)}{\partial V_b}).\end{aligned} \tag{4.12}$$

This equation is considerably simplified assuming a tunneling matrix element that does not change with energy (constant tip-sample distance z, small voltages $V_b << \Phi_{s,t}$) and a tip density of state that is constant in energy $\rho_t(E) = \rho_t(E_F)$. The last three parts of equation 4.12 vanish and the dI/dV signal simplifies to

$$\frac{dI}{dV} = \frac{2\pi e^2}{\hbar}|M_E|^2\rho_t(E_F)\rho_s(E_F + eV_b). \tag{4.13}$$

At a constant tip-sample distance using a metallic tip the DoS of the sample is directly correlated to the dI/dV signal.

4.2 Experimental setup and measurement techniques

The measurement setup consists of a CreaTec ultra-high vacuum STM system with two separate main vacuum chambers. A photograph of the STM machine is shown in figure 4.1 a) and the location of the preparation and STM chamber is indicated. The cryogenic system is located on top of the STM chamber. The whole setup is mounted on pneumatic feet that reduce low frequency noise from mechanical vibrations.

The preparation and STM chamber each feature an ion sputter pump in combination with a titanium sublimation pump to provide ultra high vacuum in the lower 10^{-10}mbar. Two metal evaporators can be mounted to the preparation chamber to deposit different materials onto surfaces. A sputter gun is connected to the chamber and a Ne gas line is attached by a needle valve to clean the sample by sputtering in a Ne atmosphere. A load lock chamber and turbo pump is located next to the preparation chamber to transfer samples in and out of the vacuum. The system

---

[1] Leibniz integration rule:

$$\frac{d}{dx}\left(\int_{a(x)}^{b(x)} f(x,t)dt\right) = f(x,b(x)) \cdot \frac{d}{dx}b(x) - f(x,a(x)) \cdot \frac{d}{dx}a(x) + \int_{a(x)}^{b(x)} \frac{\partial}{\partial x}f(x,t)dt \tag{4.11}$$

has a fully rotatable, movable manipulator arm with two stages for sample heating. Additionally, the manipulator can be cooled down with liquid Helium (LHe) to suppress diffusion and enable single atom evaporation.

The second chamber includes the STM head and cryogenic system. The manipulator arm reaches from the preparation chambers into the STM chamber. he tip and sample can be transferred between the manipulator and STM head by a wobble stick. The cryogenic system is located on top of the STM chamber and temperatures of 1.3 K are achieved at the STM head by a two stage cooling process. The main cryostat is filled with LHe at 4.2 K and is shielded by an outer cryostat filled with liquid nitrogen (LN_2). A small amount of LHe from that reservoir is filled into a smaller container below the cryostat which is thermally coupled to the STM head. By pumping on this so called 1 K-pot volume the vapour pressure over the surface is reduced. By that, high energetic particles are pumped away from the LHe surface and a temperature of 1.3 K is reached at the STM head. The amount of LHe reduces over time and the 1 K-pot holds for approximately 15 h until it needs to be refilled. The STM tip is controlled by piezoelectric elements which precisely control the x, y and z motion of the STM tip.

The STM head used for the presented experiments features a home built antenna which enables the irradiation with high frequencies (HF). The HF lines from room temperature all the way through the cryostat to the STM head at 1.3 K were previously implemented and a detailed description of the building procedure and characterization of the lines is found in [86]. A HF generator with an output energy between 20 GHz and 40 GHz was used for the irradiation of the junction.

Imaging methods in an STM

Equation 4.10 showed that the tunneling current depends exponentially on the distance of the tip to the sample, provided that the density of states of tip and sample are constant at a given bias voltage. There are two different operation modes that provide atomic resolution of the sample surface (figure 4.1 c)).

The **constant-height scanning method** records the tunneling current while scanning the tip over the surface at a constant z-level height. Any features on the surface changing the sample-tip distance cause a change in the tunneling current and thereby the topography is reproduced.

The **constan-current scanning method** avoids the danger of unexpectedly high features causing the tip to crash into the surface. The method consists of a feedback loop between the measured current and the tip height. Here the tip-sample distance is adjusted according to the measured current. By that the topography is displayed in the z-position of the tip while the current retains a fixed value.

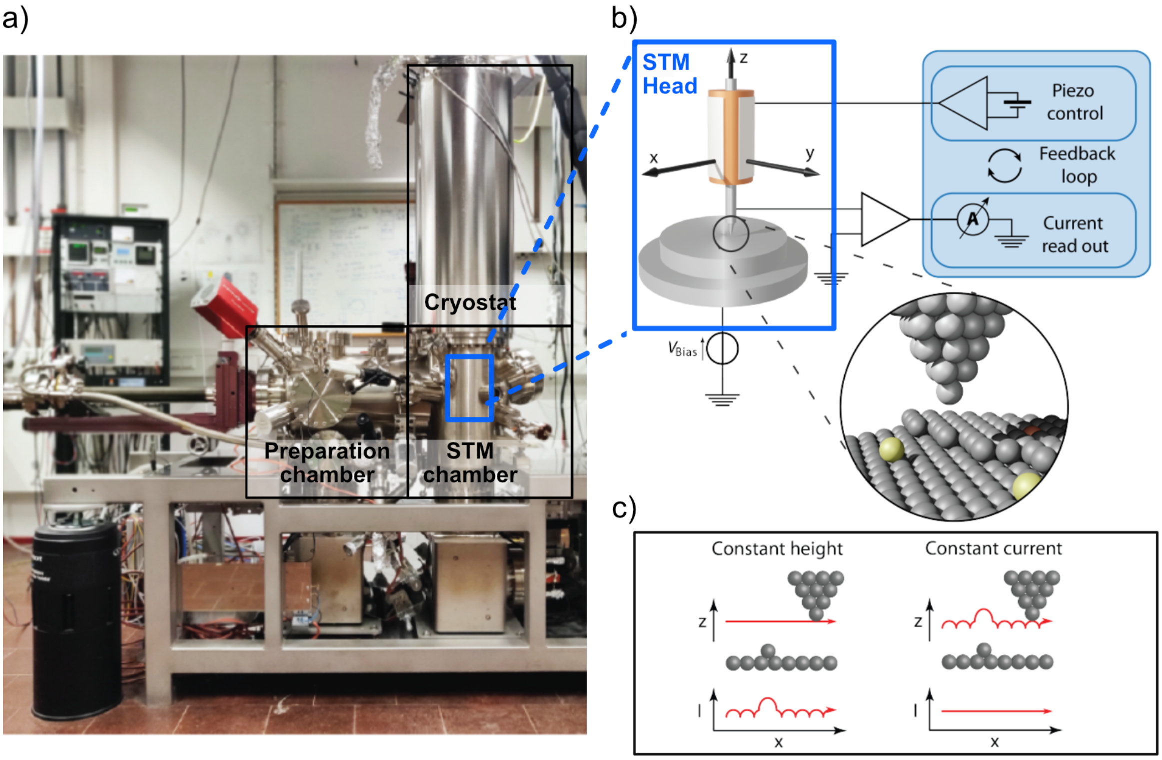

Figure 4.1: Experimental STM setup. The system consists of the preparation and STM chamber as indicated by the black boxes in the photograph in a). On top of the STM chamber the cryostat is located, reaching temperatures of 1.3 K at the STM head. A schematic drawing of the STM head is shown in b). The tip is connected to piezoelectric elements for x,y and z movement. A bias voltage is applied to measure the tunneling current. With this setup atomic resolution of sample surfaces is achieved. In c) two operation methods for scanning topography are indicated. In the constant height scanning method the tunneling current is measured while keeping the z parameter constant. Topographic features appear in the measured current. In the constant current mode the measured current and piezoelectric element control are connected via a feedback loop so that the tip height changes in response to the measured current. In this case the current remains at a set-point value while the tip is tracing topographic features in its z-component. Figure adapted from [86].

Spectroscopy in an STM

In scanning tunneling spectroscopy (STS) the local density of states (LDoS) can be recorded by maintaining a constant tip-sample distance and sweeping the bias voltage. By applying a voltage to the junction the available states up to energies of $E = eV_b$ contribute to the measured tunneling current. Schematic drawings of the tunneling processes between two metal electrodes are shown in figure 4.2 a)-c).

The derivative of the tunneling current with changing voltage is a measure of the convoluted density of state of tip and sample (see chapter 4.1). The dI/dV spectra are measured directly using a lock-in amplifier. The lock-in amplifier modulates the applied voltage by a set amplitude and frequency (usually of around 1 kHz) while it filters for noise at other frequencies at the same time. The response of the tunneling current over an integration time of several milliseconds is a measure of how strongly the current changes in the energy range of the set amplitude.

Sweeping the applied voltage shifts the energy levels of the two electrodes with respect to each other and gives an energy resolved tunneling spectrum. With a metal tip the dI/dV reproduces the local density of states of the sample surface. The energy resolution in this type of junction at finite temperature is determined by thermal broadening given by the Fermi-Dirac distribution (eq. 4.2) which is indicated in orange in figure 4.2. Arrows in figure 4.2 a)-c) indicate tunneling electrons at energies close to E_F. The sharper the step function at E_F the higher the energy resolution of the spectroscopy.

Scanning tunneling spectroscopy can be combined with topography recordings to spatially map features in the density of states stemming from irregularities on the surface e.g. atomic or molecular adsorbates. These maps are recorded by identifying features in the density of states in dI/dV measurements. These features can be probed at a constant tip-sample distance by applying the voltage that corresponds to the energy of the identified feature. For each data point the dI/dV signal is measured by the lock-in amplifier, modulating the bias and measuring the change in the current signal while scanning the tip over the surface. However as has been shown in chapter 4.1, the topography is a convolution of the tip-sample distance and the sample's density of states. For that reason the recorded topography is distorted by features in the LDoS of the sample that appear at energies of the scanning voltage. To circumvent that convolution a multichannel scanning procedure is applied in the so called **constant contour map**. The topography is recorded at energies for which the DoS of the sample is not affected by the surface states under investigation. Subsequently, the recorded topographic trajectory is retraced by the tip line by line while the voltage is set to probe the energy of interest. This procedure ensures a accurate recording of the spatial extend of features in the DoS that is decoupled from the topography.

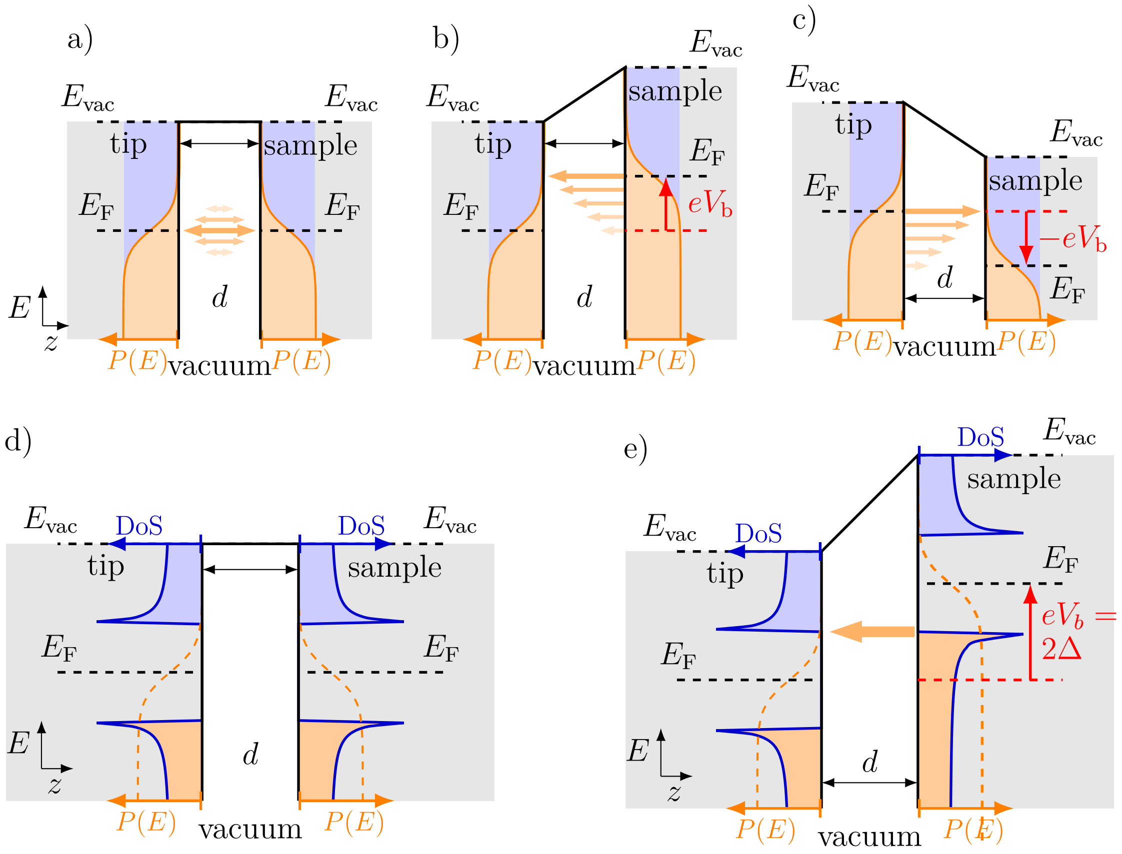

Figure 4.2: Schematic presentation of tunneling processes in STS experiments. The occupation probability $P(E)$ of electron states at finite temperature is indicated in orange as given by eq. 4.2 (empty states are shaded in blue). a)-c) show tunneling process from a metal substrate to a metal tip, with a) $V_b = 0$, b) $V_b > 0$ and c) $V_b < 0$. In a) there is no preferred tunneling direction (I=0). In b) and c) electrons tunnel from the energetically higher electrode to the energetically lower electrode. d) and e) show quasiparticle tunneling processes between superconducting tip and sample for $V_b = 0$ and $V_b = 2\Delta/e$, respectively. As derived in eq. 2.15 the quasiparticle density of states has a gap Δ around the Fermi energy (blue line). There are no available states directly around the Fermi energy so that the transition from occupied to unoccupied states is much sharper than the thermal broadening of eq. 4.2. No quasiparticle tunneling processes occur below voltages of $V_b = 2\Delta/e$ as indicate in e).

STS with superconducting tips

In this work superconducting tips and samples are used for spectroscopy. As previously established the tunneling current is a convolution of the tip and sample DoS. The DoS of a metallic tip is constant in energy and the occupation probability of electron states is given by the Fermi-Dirac distribution function (eq. 4.2). The broadening of equation 4.2 around the Fermi energy is determined by the temperature of the system and limits the energy resolution of the dI/dV spectra.

Tunneling processes between a superconducting tip and sample are schematically displayed in figure 4.2 d) and e). The DoS of a superconducting tip is not constant in energy but features a superconducting gap as was previously introduced in equation 2.15. Due to the lack of single electron states below the coupling energy of the Cooper pairs Δ, no tunneling events are possible below a minimum applied voltage of $V_b = \Delta/e$. For that reason all features in the sample DoS are shifted by Δ in the recorded dI/dV spectra. Accordingly, a superconducting sample that is probed by a tip of the same superconducting material results in a superconducting gap of 2Δ in the dI/dV spectrum.

Using superconducting tips are advantageous for spectroscopy because temperature broadening has a smaller effect on the energy resolution. Due to the energy gap the transition between occupied and unoccupied states is much sharper when convoluted with equation 4.2 at finite temperature as indicated in figure 4.2 d) and e) by orange curves. For that reason thermal broadening of the spectroscopic features is less pronounced when using superconducting tips.

4.3 Preparation of magnetic adatoms on superconducting surfaces

The experiments in this work were conducted on a bulk a Pb(111) crystal. Surface preparation of the crystal is crucial for STM experiments. The goal of the preparation procedure is to achieve large terraces of about 50 nm × 50 nm to enable the analysis of adsorbates on the surface.

Impurities are removed from the Pb surface by a sputtering process in Ne atmosphere. Elevated temperatures of around 100 °C increase the sputtering efficiency and have proven to result in larger terraces on the Pb surface. In a subsequent annealing process the sample is heated to 130 °C where the surface atoms are mobile and reform to the ordered lattice at the surface. This sputter-annealing cycle can be repeated several times to ensure the removal of all surface contamination. The cool down process of the last annealing cycle needs to be slow, so that the surface atoms rearrange in large terraces.

Single magnetic atoms are deposited by electron beam evaporation from a rod or plate of the chosen metals. Electrons are emitted from a filament by applying a current of several mA. The electrons are accelerated towards the target material by a voltage of about 800 V to evaporate the material. The emission current of the ionized material is controlled by the current through the filament and ultimately the material leaving the evaporator generates a flux current of several nA. The sample is transferred from within the cold STM to the manipulator which is cooled down by LHe to reduce lateral diffusion of the atoms that are deposited on the surface. Before transferring the sample into the STM chamber, the transfer tool needs to be pre-cooled on the LN_2 shield of the cryostat to avoid heating the sample during the transfer process.

Cr and Mn are evaporated in quick succession and the evaporation parameters were chosen so that large areas of clean Pb(111) with well separated single atoms of Mn and Cr are achieved. Both atoms are adsorbed on the Pb surface in a metastable adsorption site. The forces acting between tip and sample cause the atom to jump to a more stable adsorption site when moving the tip close to the atom.

In figure 4.3 dI/dV spectra for Cr and Mn in the two adsorption sites are shown as well as topographic images of the two configurations. The topographic images show the Pb(111) surface with well separated single Mn and Cr atoms. Two Ne impurities that originate from the sputtering process during cleaning of the Pb(111) surface appear as dark shapes on the surface. A Pb atom was placed close to this preparation. Single Pb atoms drop from the STM tip onto the Pb surface and can be manipulated laterally. For that purpose the electric field between tip and atom needs to be strong enough to move the atom between adsorption sites. At a bias voltage of about 5 mV and tunneling currents between 8 nA and 20 nA create a sufficiently strong field depending on the exact tip shape. Moving the tip with these parameters towards the Pb atom and subsequently moving to the desired location on the surface drags the atom across the surface. During this procedure the atom is hopping between adsorption sites. While Mn and Cr adatoms arrange randomly on the the surface the Pb atoms are placed deliberately near an area where an Mn and Cr atom are found within a few nm^2.

In 4.3 a) the magnetic atoms are in the as-deposited adsorption site and in 4.3 b) both adatoms were put in the more stable adsorption site by approaching the tip to the atom. The apparent height of the more stable adsorption site is larger and is referred to as the ’up’ adsorption site as compared to the other (’down’) absorption site.

In figure 4.3 c) and e) the dI/dV spectra of Mn and Cr adatoms in the ’down’ adsorption site are shown. Mn and Cr both have five unscreened electrons in their d-shell with the electronic configuration of $[Ar]3d^5 4s^2$ and $[Ar]3d^5 4s^1$, respectively. On the crystal surface both atoms are expected to adsorb in oxidation states (Mn^{2+} [40] and Cr^{1+} [101]). The crystal field of the Pb(111) surface shifts the singly occupied d-orbitals in energy to non-degenerate levels. Spectroscopically, not all YSR states can be distinguished within the resolution of the dI/dV spectra. The YSR states shift in energy and intensity as the adsorption site changes to the ’up’ position as shown in figure 4.3 d) and f).

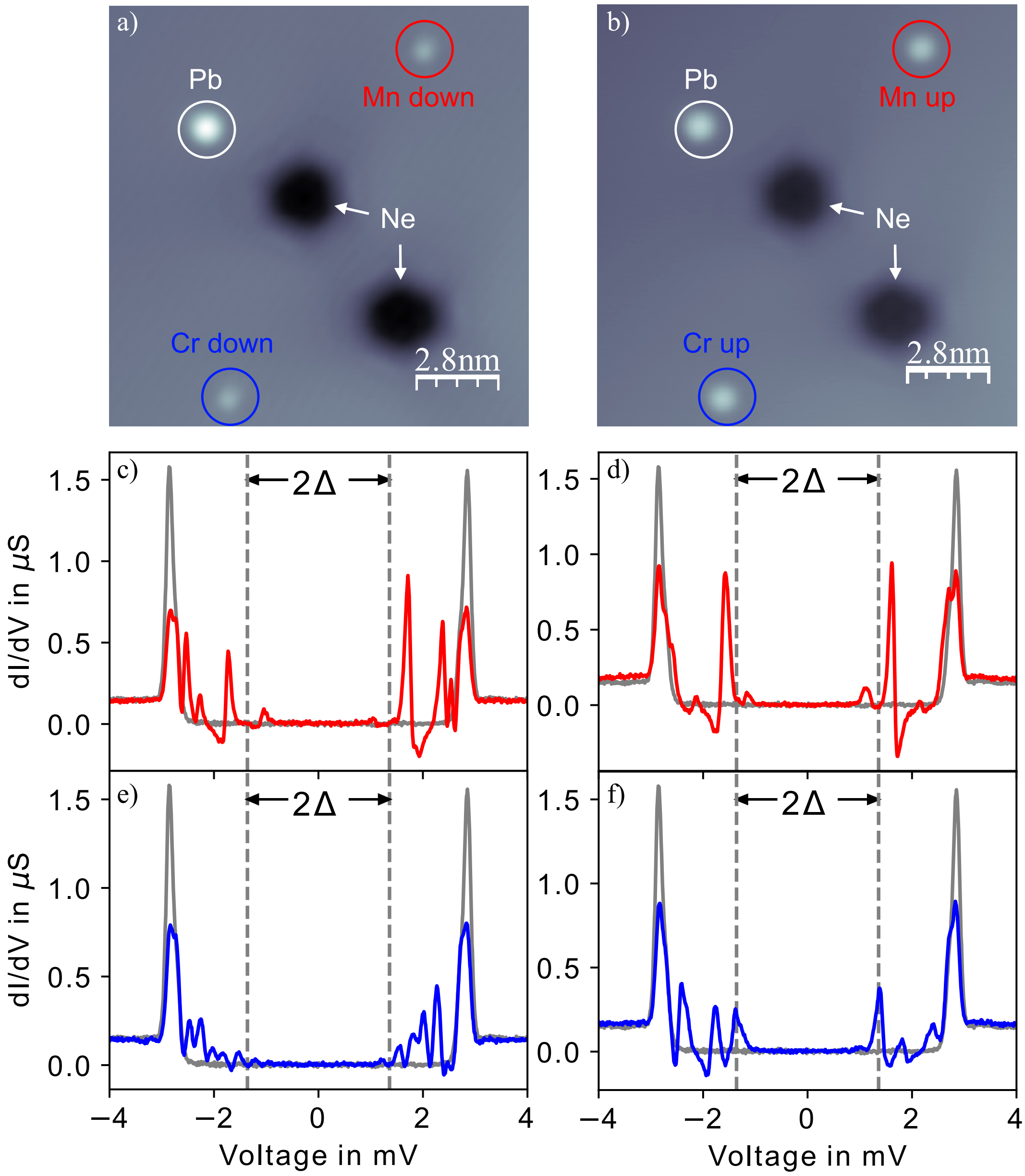

Figure 4.3: Adsorption sites of Mn and Cr adatoms on a Pb(111) surface. The topographic images in a) and b) show a Mn, Cr and Pb atom as well as two Ne impurities. In a) Mn and Cr are in the as-depostited adsorption site and are put into the more stable adsorption site in b) which shows a larger apparent height. The corresponding dI/dV spectra for Mn and Cr in the lower configuration are shown in c) and e) and for the up configuration in d) and f).

The shape of the orbitals of the unscreened electrons can be visualized by mapping the lateral extension of the states on the surface. dI/dV maps are generated by recording the the topography in a constant current measurement and subsequently tracing the profile while probing the LDoS at a specific energy. In figure 4.4 the energies of the most pronounced YSR states in the dI/dV spectra of Mn and Cr are indicated by solid black lines. Tracing the z-profile and probing these energies result in the dI/dV maps also shown in figure 4.4. For both magnetic adatoms the YSR states show a lateral extension on the Pb(111) surface. The specific shapes of the states can be correlated to the orbitals of the d-shell electrons that cause the corresponding YSR state [40, 101].

4.4 Josephson spectroscopy

Josephson junctions are formed in an STM by approaching the superconducting tip to the superconducting surface until Cooper pairs start to tunnel causing a peak in the dI/dV spectra at zero bias. At these high conductances the forces acting on the tip by the electric field become increasingly strong. The tip material (Pb) used in this work is a rather soft material that easily falls apart at these conductances. With low noise levels and sufficiently stable tips topographic images at high conductances reveal the atomic structure of the Pb(111) surface as shown in figure 4.5 a). We found that placing a single Pb atom in the junction stabilizes the tip and prevents it from breaking as easily. Figure 4.5 b) shows the dI/dV spectra with increasing junction conductances measured at 10 mV between 25 µS and 50 µS normal state conductance. The Cooper-pair tunneling peak appears at zero bias voltage and gains intensity the higher the normal state conductance. Additionally, Andreev reflections of the first and second order appear at $E_A = \frac{2\Delta}{(n+1)}$ with n = 1 and n = 2. It is unique to Josephson junctions formed in an STM that the junction conductance is easily tunable by adjusting the distance between the two superconductors.

Josephson tip preparation

The STM tip itself consists of a tungsten wire that is mounted to a holder that is controlled by piezoelectric elements. To remove any foreign material contaminating the tip or impairing its stability, field emission is performed. For that purpose high voltages of 100 V are applied between tip and sample. By moving the tip closer to the surface the measured field emission current increases. The forces that act on the material both electric and thermal remove material from the tip. The process is repeated until a stable tunneling current can be established without the tip changing. Subsequently, the tip is coated by a sufficiently thick layer of superconducting material from the sample to produce a full superconducting gap. For that purpose a voltage of 10 V is applied while allowing for a current flow of a few micro Ampere. The tip is indented into the surface of the sample by several nm while moving in x

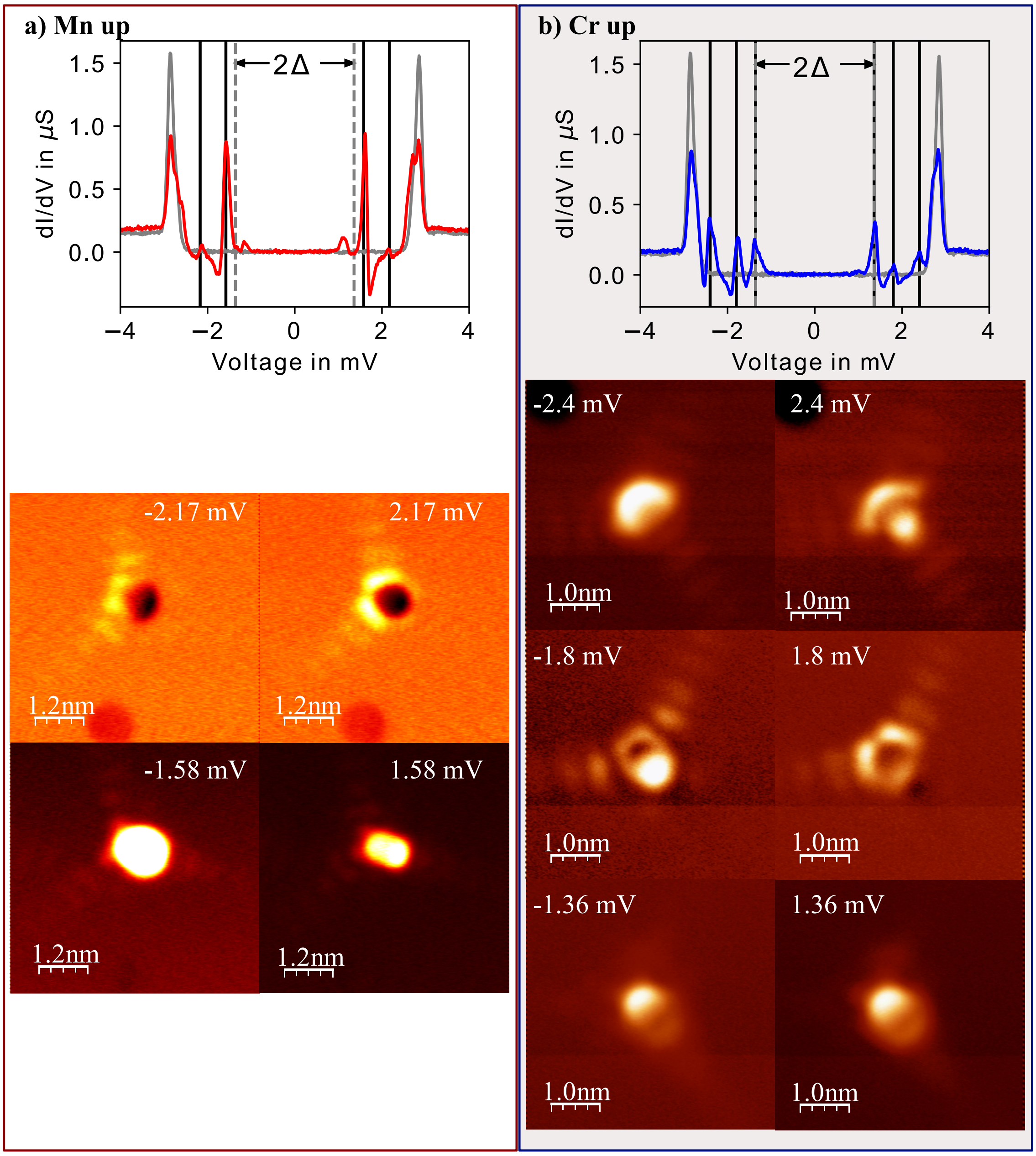

Figure 4.4: dI/dV maps of YSR states. dI/dV maps for Mn and Cr in the up configuration are shown in a) and b). The YSR energy states are identified in the dI/dV spectra and indicated by lines. The maps visualize the shape of the orbitals of the unscreened electrons causing the specific YSR states.

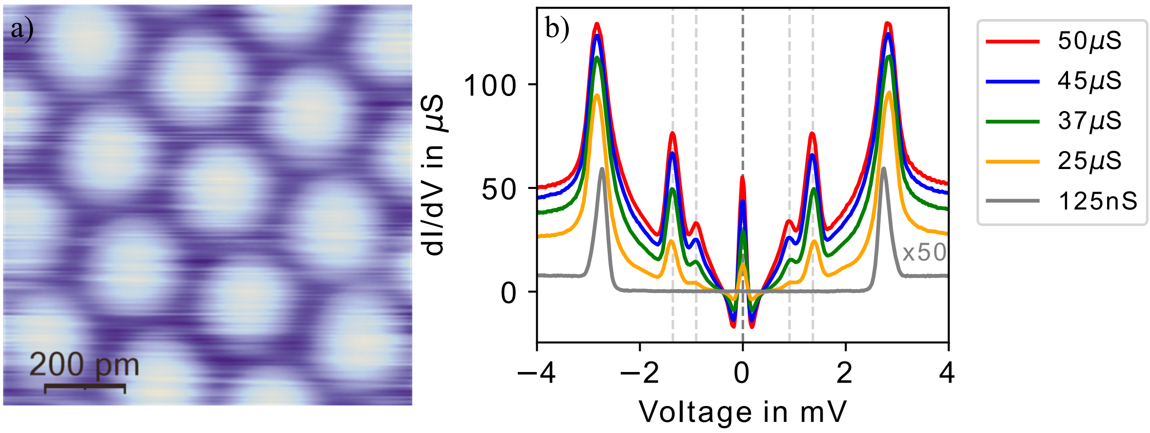

Figure 4.5: dI/dV-spectra on a Pb(111) surface with junctions conductances between 125 nS (setpoint: 4 mV, 500 pA, $V_{rms} = 15\,\mu V$) and 50 µS (setpoint: 10 mV, 500 nA, $V_{rms} = 15\,\mu V$). a) shows an atomic resolution image of the Pb(111) surface scanned at high junction conductances with a very stable tip. b) shows dI/dV spectra at different junction conductances measured at 10 mV. The intensity of the Josephson peak and Andreev reflections increases with increasing junction conductance.

and y direction as well. Smaller indentations of a few hundred pm are subsequently employed to sharpen the tip and ensure the stability. This process is repeated several times until the tip is superconducting and has a round apex round.
For Josephson spectroscopy the tip needs to fulfil very high stability standards to withstand the strong electric and atomic forces that act at the necessary junction conductances. The tip is further stabilized by approaching the tip carefully to smaller clusters or single atoms of Pb until the tip and surface remain unchanged at the desired parameter of the measurement. Approaching the tip to the bare Pb surface is more likely to cause changes of the tip than approaching to topographic features on the surface. Sometimes small clusters or single atoms drop from the tip, which can be used for the experiments described below.

Josephson junction setup

Conventionally in STS the DoS is probed by varying a voltage bias at a fixed tip-sample distance (chapter 4.2). As explained in detail in chapter 3, Cooper-pair tunneling sustains a current flow without a voltage drop across the junction. Applying an external voltage inherently prevents the zero-voltage state of the junction and destroys phase coherence. That effect is captured in the dc and ac Josephson equations (eq. 3.1 and 3.4). An applied voltage, directly imposes a variation of the phase difference across the junction over time.

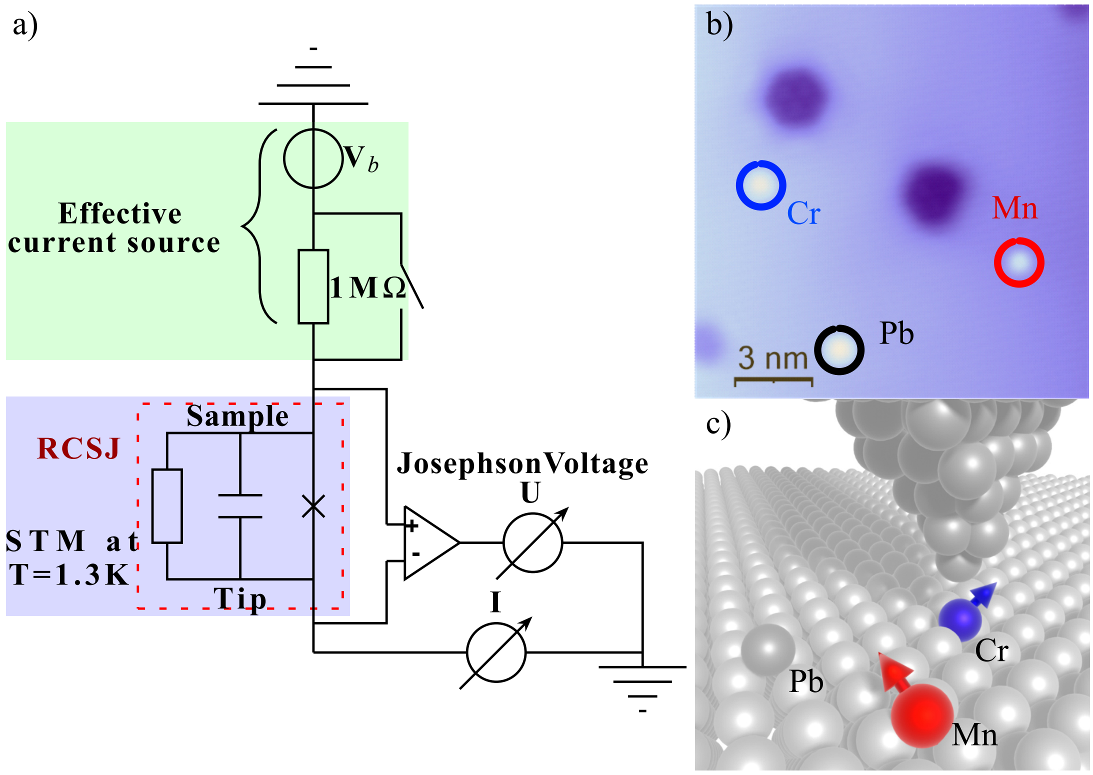

Figure 4.6: a) Josephson spectroscopy setup. To measure Josephson spectroscopy in current bias a 1 MΩ resistor is added to the bias line resulting in an effective current bias. A switch that bypasses the resistor is used to switch between voltage and current bias. A differential amplifier is employed to measure the voltage drop over the junction. b) Topographic image of a Pb(111) surface with single atoms of Pb, Mn and Cr. c) Schematic image of the STM setup with three different species of atoms on the Pb surface.

For that reason, in our experiments we aim at applying a current bias to our STM junction. This is achieved by implementing a 1 MΩ resistor in the bias line of the STM as shown in the circuit diagram in figure 4.6. The resistor is much larger than the Josephson junction resistance and the voltage drops primarily over this resistor and effectively becomes a current bias. To easily change the measurement mode from a voltage to a current bias a switch is included that bypasses the resistor. The voltage drop at the junction is measured and amplified by a factor of 10^3 with a differential amplifier.

Measurement procedure

Josephson spectroscopy is quite delicate with respect to tip stability and piezoelectric creep. Moving the tip in the z-direction by the piezoelectric elements results in a creep that depends on the distance of movement and declines over time. To get a well resolved VI-curve with reasonable high switching currents the junction conductance needs to be as high as 50 µS ($V_b = 10\,\mathrm{mV}$, $I_{set} = 500\,\mathrm{nA}$). If not indicated otherwise in the text, normal state conductances were set at a bias voltage of 10 mV which is well outside the superconducting gap of Pb. Switching and retrapping events are of statistical nature so that a few hundred repetitions of VI measurements are necessary. During these repetitions the feedback is turned off and the tip remains in very close proximity to the atom without corrections in the z-direction. Piezoelectric creep can cause the tip to crash into the surface on the timescales of the measurements. For that reason long waiting times after moving the tip over large features in x and y direction or after retracting the tip in z-direction are necessary before successfully performing Josephson spectroscopy.

As previously explained temperatures of 1.3 K are achieved by pumping on a small amount of liquid Helium in the 1 K-pot. After about 15 h the liquid Helium in the 1 K-pot runs empty and needs to be refilled. For that the tip needs to be retracted by about 30 nm to prevent crashing the tip. Careful planning of measurement schedules is necessary since after retracting the tip, waiting times of about 6 h are necessary for piezoelectric creep to diminish enough to safely employ Josephson spectroscopy. This leaves a time window of about 8 h to safely measure the prepared atoms without endangering the preparation.

For the actual measurements the atom of interest is approached to the desired junction conductance. Low noise is required to properly regulate with the feedback loop at currents as high as 500 nA.

The feedback loop employs proportional-integral-derivative (PID) control. To regulate at high conductances it is necessary to reduce the proportional parameter to a few hundred fm, so that small spikes in the current don not cause the tip to over regulate. After waiting a few minutes to stabilize the current at the desired junction conductance, the Josephson routine is started. For that, a Labview program was employed to automatically turn off the feedback loop before it switches from the voltage bias to the current bias method by opening the bypass switch so that the the applied voltage drops over the 1 MΩ resistor. After waiting a few minutes to stabilize the circuit the current is swept backward and forward while the voltage is measured by the differential amplifier. 500 to 2000 repetitions are usually recorded before the STM is set back to the voltage bias mode and the feedback loop is reestablished.

CHAPTER 5

DATA ANALYSIS

In this chapter the data processing and statistical analysis of Josephson spectroscopy will be explained. The analysis in this work was done by self written python programs. The routines and original data sets of the results published in [1] can be found in [102].

Systematic influences at high conductances need to be accounted for when applying a current or a voltage bias to the Josephson junction. The line resistance of the leads to the junction become large in comparison to the junction resistance. Specifically in the voltage-biased junction the influence of the line resistance becomes noticeable. In contrast, the resistance of the leads does not significantly influence the the current-biased junction as the 1 MΩ series resistor dominates the line resistance. This is no longer true outside the Cooper-pair tunneling regime, where the in-gap junction resistance is high.

In the current-biased Josephson junctions the phase dynamics result in statistical escape events. For that reason many repetitions need to be recorded for a statistical analysis of the events. As the repetitions take time the junction conductance may change during the measurement due to piezoelectric creep which is highly dependent on the history of the tip movement prior to the measurement. Other effects like a drift that occurs in the voltage amplifier and biasing offsets need to be accounted for.

For measurements in the presence of high frequency irradiation the damping of the HF-lines need to be established to accurately determine the amplitude of the irradiation at the junction. For that purpose the splitting of the conductance peaks need to be simulated by the approach of P. K. Tien and J. P. Gordon for photon-assisted tunneling as explained in chapter 3.3.

5.1 dI/dV spectroscopy at high conductances

The dI/dV spectra in an STM junction are measured directly by modulating the applied voltage and recording the relative change of the IV-signal by a lock-in amplifier (chapter 4.2). The lock-in frequency was usually set to values between 800 Hz and 950 Hz optimizing the noise level at different frequencies and the amplitude for the dI/dV spectra shown in this thesis was set to $V_{rms} = 15\,\mu\text{V}$. The relative values obtained by the lock-in amplifier need to be regauged into physical values by comparison to the numerical derivative of the directly measured I(V)-curves. A linear fit of the dI/dV signal plotted over the numerical derivative of the I(V)-curves gives the parameter to connect the measured lock-in signal to the physical values of the measured conductance.

In figure 5.1 a) dI/dV spectra at low and high conductances are shown. Dashed lines indicate the gap values of $\pm\Delta = \pm 1.37\,\text{meV}$ and $\pm 2\Delta = \pm 2.74\,\text{meV}$. It is observed that the coherence peaks located at $\pm 2\Delta$ are shifted considerably as the junction conductance increases. At junction conductances of more than 50 µS the line resistance can no longer be neglected. The resistance of the wires leading down to the junction is dominated by a high frequency filter with an internal resistance of 1.3 kΩ. The voltage drop at the junction V_{junction} is calculated from the applied voltage V_b by considering the voltage drop at the measured current I_{meas} over an estimated series resistance that corresponds to the resistance of the wires R_s ($V_{\text{junction}} = V_b - I_{\text{meas}} \cdot R_s$). In figure 5.1 b) the original and corrected dI/dV spectra at high conductances are shown. The coherence peaks of the corrected data are much closer to the expected values when considering an overall series resistance of $R_s = 1.6\,\text{k}\Omega$. For that reason the dI/dV spectra are corrected for the series resistance throughout this thesis. A slight apparent discrepancy of the coherence peak position can be explained by the fact that Pb is a two-band superconductor [26]. The intensities of the inner gap coherence peak is very high on Pb(111) at low conductances. The intensity weight appears to shift towards the higher gap value as we approach the surface.

5.2 Statistical analysis of Josephson spectroscopy

In chapter 3.1 the fundamentals of Josephson junction were explained. The RCSJ model with the tilted washboard potential picture is a useful tool to understand the phase dynamics of a Josephson junctions.

In figure 5.2 a) an exemplary voltage-current characteristic (I(V)C) of a STM Josephson junction at 50 µS is shown for an upwards and downwards sweep of the current bias. Two step-like features for each sweep direction can immediately be distinguished, where the junction transitions between the Cooper-pair tunneling regime and the normal conducting regime. The transition from the normal regime to the Cooper-pair tunneling regime is indicated by green colors and is recognized

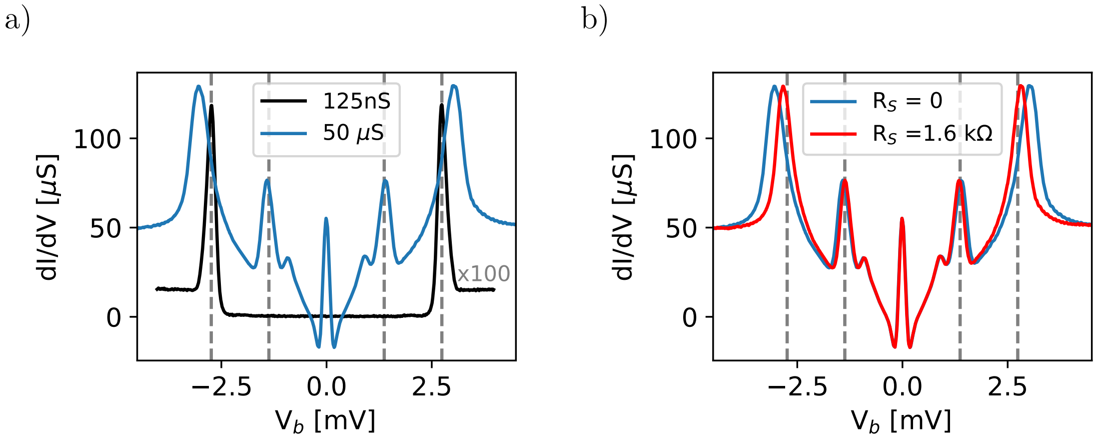

Figure 5.1: Systematic correction of dI/dV spectra. a) shows dI/dV spectra on Pb(111) at high and low junction conductances. As previously explained Andreev reflections and the Josephson peak appear at high conductances. Dashed lines indicate the once and twice the superconducting gap values. A shift of the coherence peaks occurs at high conductances due to the series resistance of the lines. In b) the high conductance data was corrected by a series resistance of 1.6 kΩ (red curve). The coherence peaks match the expected value of 2Δ by this correction.

as the **retrapping current $\boldsymbol{I_{\mathrm{re}}}$**. The opposite transition from the Cooper-pair tunneling regime to the normal regime is occurs at the **switching current $\boldsymbol{I_{\mathrm{sw}}}$** and is indicated by blue dashed lines in figure 5.2 a). The I(V)C show highly hysteretic behaviour since switching and retrapping events occur at different absolute current values.

Within the Cooper-pair tunneling regime a finite voltage is measurable due to phase diffusion within the trapped state of the junction (chapter 3.1). The slope of the I(V) curve within that regime gives a measure of the phase diffusion within the junction and is quantified by the **phase-diffusion conductance $\boldsymbol{G_{\mathrm{PD}}}$** .

The escape and retrapping events of current-biased Josephson junction are statistical parameter and influenced by the properties of the phase dynamics and the noise in the junction. For each junction at least a few hundred and up to 2500 I(V)Cs were recorded to determine the distribution of the events. In figure 5.2 b) seven exemplary curves are shown. It is observed that the statistical variation of switching currents is higher than the variation of retrapping currents.

To analyse the high amount of I(V)Cs a python program was written to automatically determine the characteristic features of the Josephson junctions, namely the switching and retrapping current as well as the phase-diffusion conductance. To determine I_{sw} and I_{re} the derivative of the curves (shown in figure 5.3 a)) was formed as shown in figure 5.3 c). The steps are clearly visible as high peaks in the derivative. For junctions with a higher noise level gaussian smoothing of the curves prior to forming the derivative was necessary to reliably identify the peaks.

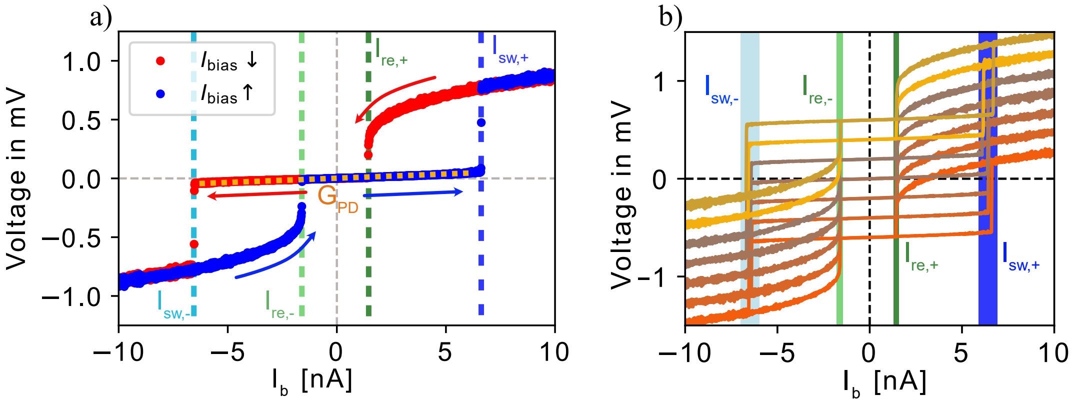

Figure 5.2: An exemplary V(I)C of a pristine Pb-Pb junction at a normal conductance of 50 µS. In a) sweep directions are distinguished by red and blue colors. Switching and retrapping currents of the hysteretic curve are indicated by dashed lines. The phase-diffusion conductance is measured by the slope in the low-voltage regime as indicated by the orange dotted line. b) shows several V(I)Cs recorded for the same junction. The curves are set off in the y-direction for visibility. The statistic behaviour of switching and retrapping events is indicated by differently coloured areas.

The values that were determined by that method are subsequently presented in a histogram as presented in figure 5.4 a). The absolute values of the currents for retrapping and switching events are shown for the two sweep direction for better readability.

A few systematic influences are recognized during the course of these measurements. For instance the voltage amplifier that was used to record the voltage has a slow drift that shift the curves on the voltage scale. That drift was corrected by determining the zero-crossing of the linear fit that was performed to determine G_{PD} for each of the curves. Another systematic error consists in a small bias offset that is recognizable when looking at the statistics of the histogram shown in 5.4 a) where an offset between the two sweep directions for switching as well as retrapping events is visible. This offset was corrected by determining the mean retrapping current for both sweep directions. In chapter 8 we will find asymmetries in the histograms in the presence of magnetic adatoms. For these data sets a reference measurement on a pristine Pb-Pb junction was performed. The exact bias offset was determined in the pristine junctions and applied for the corresponding measurements on the magnetic atoms.

Another systematic influence on the Josephson junctions consists in piezoelectric creep. Depending on the range of movement that the tip experienced before the measurements (e.g. large area scans) piezoelectric creep may be stronger or weaker and can occur in the lateral as well as in the z-direction. During the measurement

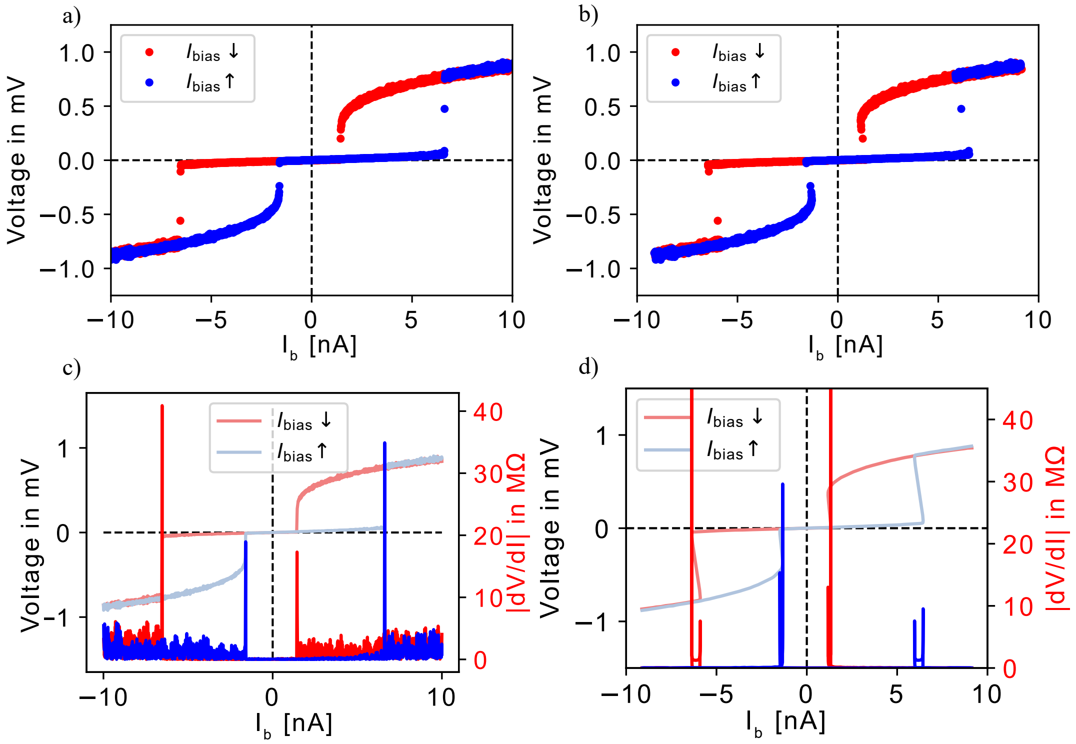

Figure 5.3: Analysis of I(V)Cs. a) shows an exemplary I(V)C that was measured for a Josephson junction with a normal state conductance of 50 µS. Sharp transitions between the Cooper-pair tunneling and the normal regime are seen for each sweep direction (red and blue curves). b) shows the same curve but corrected for the voltage drop recorded in the resistive regime of the junction. The curve becomes slightly skewed. c) shows the derivative of the V(I)C in a). The peaks clearly indicate the transitions between regimes, i.e. switching and retrapping events. The derivative of the V(I)C shown in b) is plotted in d). Due to the non-monotonic behaviour of the V(I)C the peaks in the derivative are not unambiguous and transitions between tunneling regimes are harder to identify.

procedure it was taken care that the creep does not cause the tip to touch the surface for the chosen junction conductances. However as the tip creeps closer to the surface the junction conductance changes during the time of a measurement which can take up to 20 minutes. In figure 5.4 b) the time evolution of the histogram for the switching events is presented. The measured data was divided into batches of 200 sweeps and the resulting histograms are slightly set off on the y-scale. The average phase-diffusion conductance is indicated for each of the histograms. It is clearly shown that there is a systematic increase of the conductance that correlates to an increase of the average switching currents over time.

Physically the change of the junction conductance changes the Josephson energy $E_\mathrm{J}$of the junction and for that reason holds information on the junction properties. For that reason the switching and retrapping events can be plotted over the phase-diffusion conductance. This method allows for a better resolution of the influence of the junction conductance on the Josephson junction properties.

The strength of piezoelectric creep depends on the range in which the STM tip was moved prior to the measurement. For that reason piezoelectric creep affects the junction's normal state conductance differently strong. To correlate the characteristics of a Josephson junction to a specific normal state conductance it is possible to correct for the creep effect during the course of a measurement. In figure 5.4 the procedure to correct a histogram for the changing normal state conductance. The effect of the piezoelectric creep is illustrated for the histogram shown in figure 5.4 a). As an example for the effect of piezoelectric creep the histogram of the extracted switching currents in figure 5.4 a) was divided into sets of 200 sweeps that were recorded over time in figure 5.4 b). A systematic increase of the swithcing current over time can clearly be observed. This broadens the overall histogram significantly as shown in gray in the background of figure 5.4 b). To correct for this change of the normal state conductance over time without loosing the information of the statical events the phase-diffusion conductance G_PD was extracted for each V(I)C. The inset of figure 5.4 c) shows the phase-diffusion resistance ($R_\mathrm{PD} = \frac{1}{G_\mathrm{PD}}$) over the time of the measurement. The gray dots show the uncorrected data which are fitted by a curve that corresponds to a power-law function ($f(x) = ax^b + c$) in order to phenomenological extract the overall change of phase-diffusion resistance over time. The fitted curve was used to correct the data for the effect of piezoelectric creep as shown in the orange data in the inset of figure 5.4. It was assumed that the switching and retrapping currents are affected by the creep by the same amount as the phase-diffusion resistance and were corrected by the same relative change over time. The resulting histogram is shown in figure 5.4 c) which shows a much narrower distribution compared to the uncorrected histogram in figure 5.4 a).

Another issue arises in the current-biased measurements when recording the I(V)Cs as shown in figure 5.3, due to the low conductance that is measured in the resistive state of the junction. In the absence of Cooper-pair tunneling the junction's conductance is determined by Andreev reflections which actually results in a very high resistance for currents that are within the superconducting gap. It was found that this resistance is no longer negligible compared to the bias line resistor R_B of the setup. It is possible to correct the current at the junction I_{junction} for the non-negligible voltage drop in that area V_{measure} ($I_{\text{junction}} = I_b - \frac{V_{\text{measure}}}{R_B}$) resulting in the V(I)C shown in figure 5.3 b). This was found in a later analysis of the results and was not yet accounted for in [1]. This correction was used for the data shown in chapter 7 and in chapter 6 but is not included in chapter 8.

In figure 5.3 d) the derivative of the corrected I(V)C is shown. Due to the shift in the bias current two peaks appear instead of one for each event. For these peaks to be clearly distinguishable strong Gaussian filtering needs to be applied. The resolution and intensity of these peaks strongly depend on the noise in the junction and the density of data points during the transitions. For that reason the python program for the automatic detection of switching and retrapping events becomes unreliable and has not been yet optimized to analyse this more complicated data. In appendix B preliminary results of the analysis of the data sets that were used in chapter 3.4 are presented which show that while this correction quantitatively changes the results, it does not change the qualitative description nor the physical interpretation of the data.

5.3 HF irradiation of tunneling junction

An antenna is located near the STM junction for the irradiation with HF between 30 GHz and 40 GHz. For the details of the setup and characterization see [86]. In this section we will briefly explain the analysis and simulation of voltage-biased dI/dV tunneling spectra. Details on the current-biased junctions with HF irradiation are presented in chapter 7. Experimentally the same junction was measured with a current bias and subsequently with a voltage bias for each step of the HF amplitude for comparison.

The frequency of the HF irradiation ω_r that is applied to the antenna of the STM remains at a fixed value for each experiment and the amplitude of the signal V_{ac} is increased step by step for each recorded spectrum. In figure 5.5 a Pb-Pb junction at a junction conductance of 200 nS is shown as an example. At this low junction conductance only the coherence peaks appear in the dI/dV spectrum in the absence of the irradiation (shown in black in 5.5 c)). As the amplitude of the irradiation is increased the coherence peaks start to split due to the absorption of photons from the HF-field. With increasing amplitude more photons can be absorbed and the coherence peaks split in several distinct peaks. This is shown in the stacked color plot in 5.5 a) where the HF amplitude is plotted on the y-scale and over the voltage bias V_b on the x-scale. Colours indicate the conductance that is measured for each dI/dV spectrum. The coherence peaks are single-electron tunneling processes and for that reason split in steps of $E_{HF} = n\hbar\omega_r = eV_b$. In figure 5.5 c) the splitting of the coherence peaks is shown by comparing the dI/dV spectrum in the absence

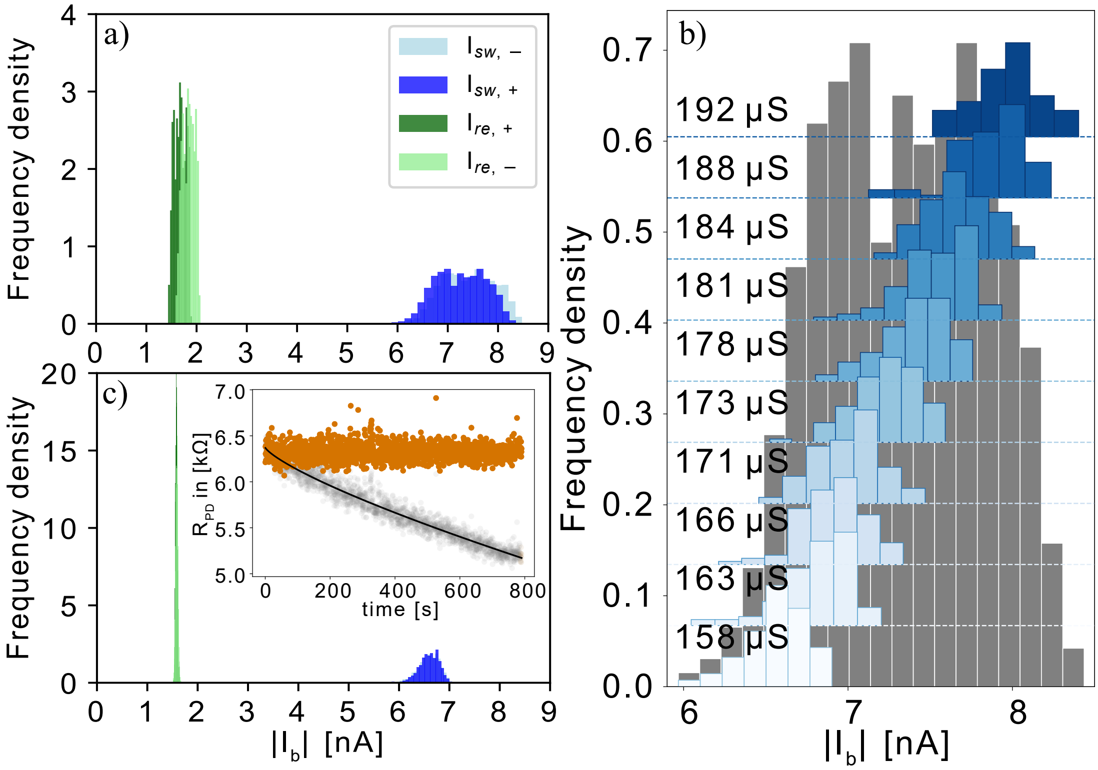

Figure 5.4: Histograms of I_{sw} and I_{re} of a Pb-Pb junction over 2000 sweeps. a) shows the histogram of absolute values of I_{sw} and I_{re} for both sweep directions as determined from 2000 single V(I) sweeps. b) shows the influence of piezoelectric creep on I_{sw} as the the tip-sample distance over time changes. For that purpose the histogram shown in the background in gray was divided into sets of 200 sweeps and the individual histograms were plotted with a slight offset for readability. The average phase diffusion conductance for each of the histograms indicated at the side. To compensate for the change of the junction conductance the phase diffusion resistance was plotted over time in the inset of c). In gray the original data is shown which was fitted by a power-law dependence and corrected for the change over time (orange data). Transferring this relative change of the phase-diffusion resistance to the measured I_{sw} and I_{re} results in the much sharper histogram shown in c).

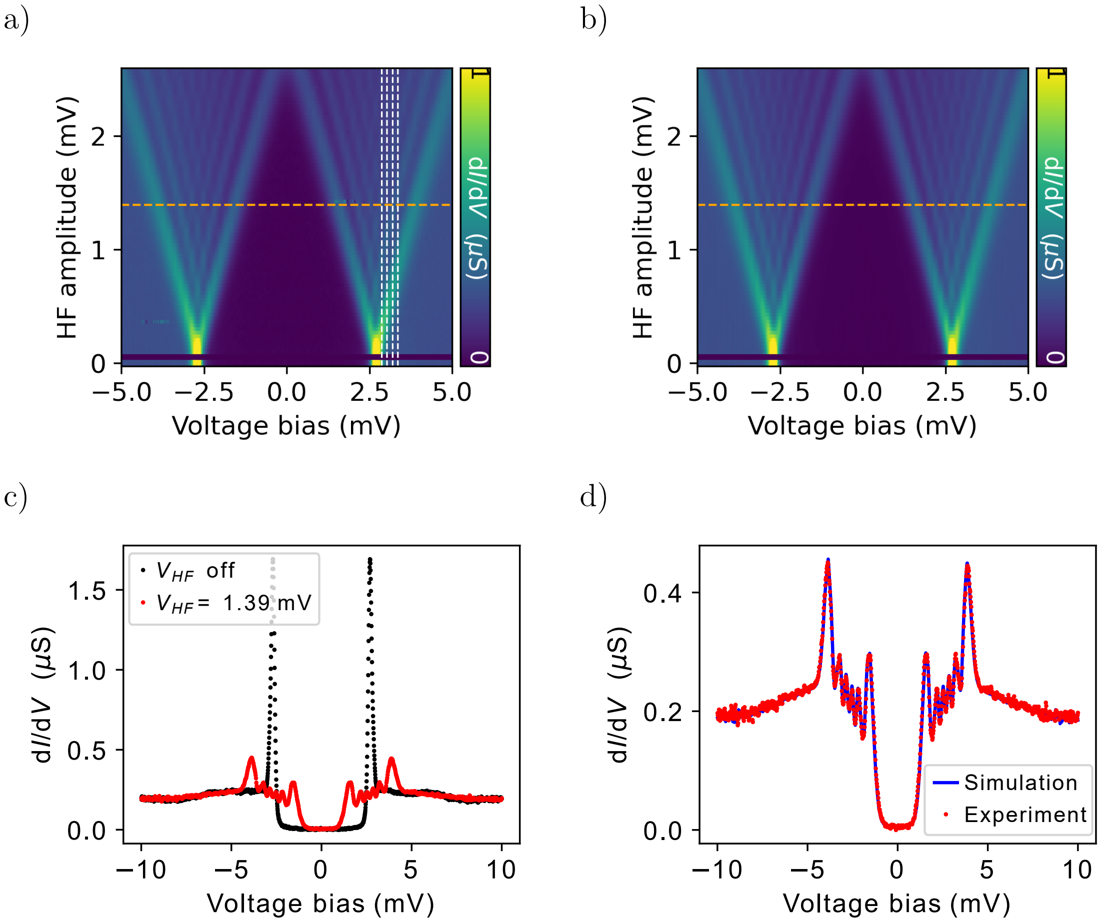

Figure 5.5: Superconducting tunneling junction under HF irradiation of $\omega_r = 40$ GHz at a normal state junction conductance of 200 nS. The coherence peaks split due to photon-assisted tunneling as can be seen in the stacked color plot in a). White lines indicate the spacing of the peaks as expected for single electron tunneling processes $eV_b = \hbar\omega_r$. b) Shows the simulation of the splitting of the coherence peaks with the model of P. K. Tien and J. P. Gordon. c) compares the dI/dV spectrum in the absence of irradiation to the spectrum under irradiation with an amplitude of 1.39 mV. In d) the measured and simulated dI/dV spectra with an amplitude of 1.39 mV are compared.

of external irradiation to the same junction with an applied field of 40 GHz and an amplitude of 1.39 mV.

The process of absorbing single photons by the tunneling electrons is known as photon-assisted tunneling. Photon -assisted tunneling was described P. K. Tien and J. P. Gordon [49]. With their model, which is described in detail in chapter 3.3, the spliting of the coherence peaks can be accurately simulated with the dI/dV spectrum recorded in the absence of HF irradiation as an input parameter. The simulation is shown in figure 5.5 b). The damping of the irradiation from room temperature to the STM junction can vary between measurements depending e.g. on the LHe level in the cryostat. The amplitude that reaches the junction is influenced by the damping of the HF line. The damping can be determined in a recursive way by comparing the signal that was measured for a certain set point amplitude with the simulation. The damping parameter is adjusted in each iteration until the measured and simulated signal match. By simulating the splitting of the coherence peaks the damping is determined for each experiment. In figure 5.5 d) the simulated and experimental data is compared for 40 GHz and 1.39 mV amplitude. The simulated data fits perfectly to the measured data.

Increasing the junction conductance up to 50 µS Andreev reflections and the Josephson peak appear. The data is treated according to the description in chapter 5.1. When the HF irradiation is applied all peaks in the spectra start splitting as shown in figure 5.6 a). From a certain amplitude the peaks start to overlap and it becomes difficult to interpret the splitting of the peaks. Again the dI/dV spectra without external irradiation is compared to the irradiated junction at 40 GHz and 0.9 mV amplitude in figure 5.6c). The simulation is compared to the experimental data in 5.6 d) and shows good agreement. Due to the overlap of the different peaks the match between simulated and experimental data is not as perfect as for the pure single-electron processes in figure 5.5 d). In figure 5.6 b) the simulation of the data set is shown. Previously we discussed single-electron tunneling processes of the coherence peaks. Now we see that the Andreev reflections and Josephson peak split with a different spacing. This is expected as the for these processes multiple electrons need to tunnel simultaneously and photons are absorbed in sets of two. Theoretically this has been derived by [51] and [50] and the model has been explained in chapter 3.3. As now two charge carrier tunnel the spacing of the peaks changes and is now expected to be $E_{HF,2e} = n\hbar\omega_r = 2eV_b$. This can be incorporated into the simulation by separating regimes for which two-electron processes are expected from the regimes where single electrons tunnel. Simulating the splitting of these areas separately and subsequently putting them back together results in a reasonable good agreement of experiment and simulation. Some small artefacts appear in the color plots of the simulation where the two regimes meet.

As we are particularly interested in the Josephson spectroscopy a zoom-in on the Josephson peak is shown in figure 5.7 a). The simulation is shown in 5.7 b). The spacing of the splitting peaks is indicated by white lines and matches the expected spacing for two electron peaks. As soon as the splitting Andreev reflections overlap with the Josephson peak the individual peak are difficult to distinguish. The simulation almost perfectly reproduces the experimental results.

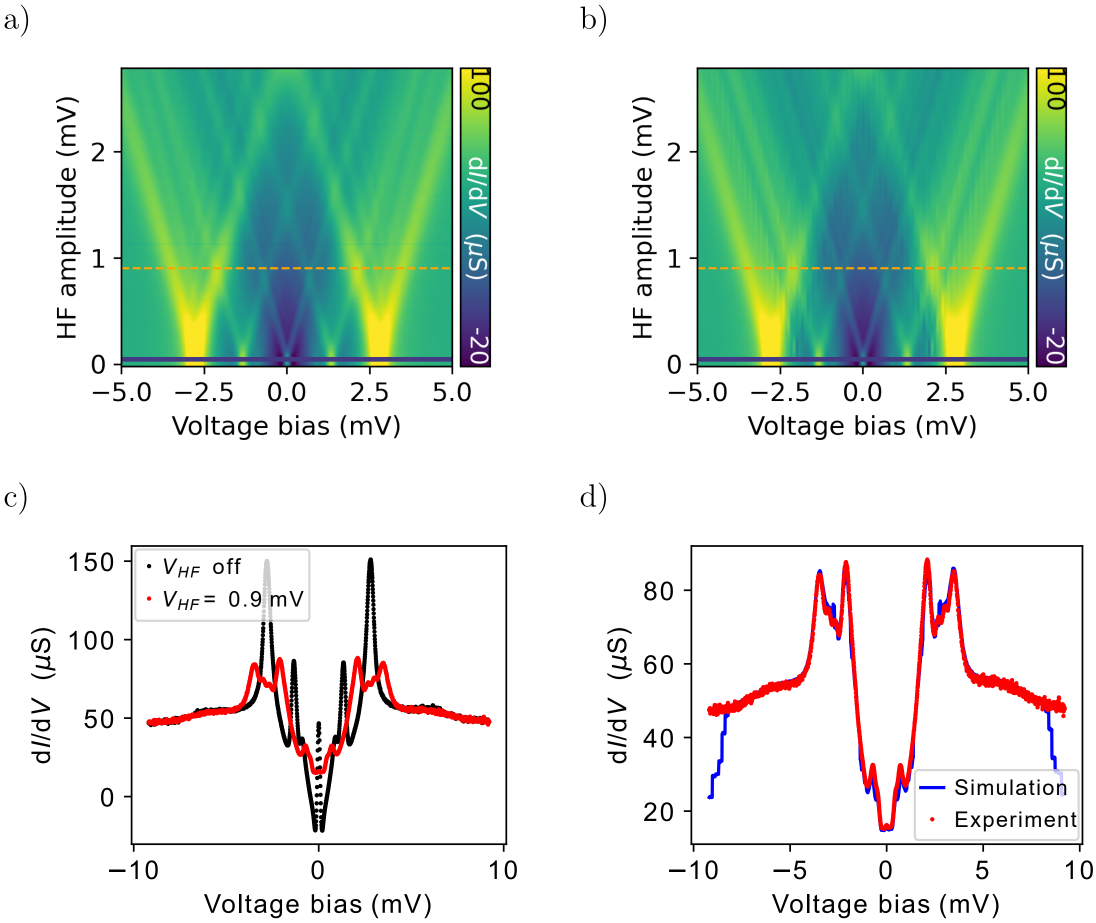

Figure 5.6: Superconducting tunneling junction under HF irradiation of $\omega_r = 40\,\mathrm{GHz}$ at a normal state junction conductance of 50 µS. The coherence peaks, Andreev reflections and Josephson peak split due to photon assisted tunneling as can be seen in the stacked color plot in a). Andreev reflections and Josephson tunneling consist in two-electron tunneling processes which results in a splitting of $2eV_b = \hbar\omega_r$. For the simulated spectra in b) two-electron and single-electron processes were treated individually. c) compares the dI/dV spectrum in the absence of irradiation to the spectrum under irradiation with an amplitude of 0.9 mV. In d) the measured and simulated dI/dV spectra with an amplitude of 0.9 mV are compared.

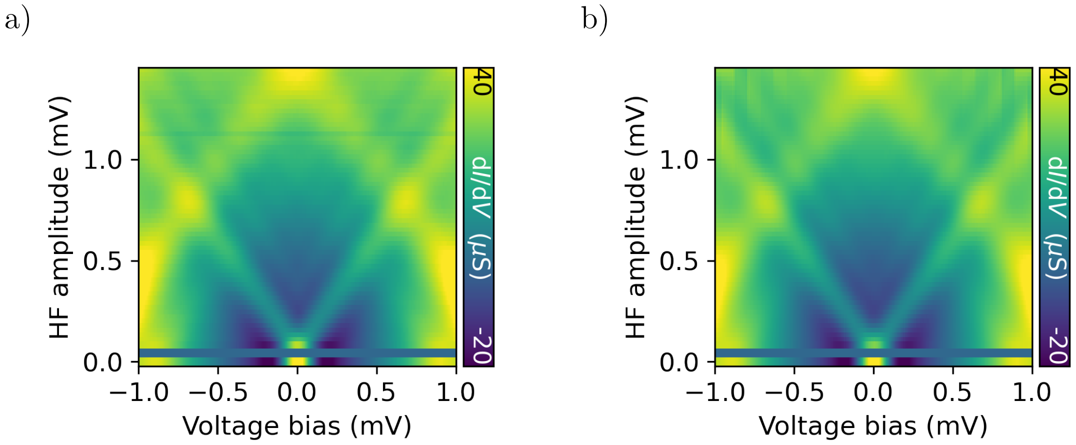

Figure 5.7: A zoom-in on the Josephson peak from the data set shown in figure 5.6. a) shows the experimental data and b) the simulation of the two-electron process.

Part III

Results and Discussion

CHAPTER 6

CHARACTERISTICS OF PRISTINE PB JOSEPHSON JUNCTIONS

The experimental findings of pristine Pb-Pb STM Josephson junctions are presented in this chapter. The RCSJ model with the tilted washboard potential picture is useful to describe the phase dynamics of the current-biased Josephson junction. The details of the RCSJ model are described in chapter 3.1. P(E)-theory takes the probability of exchanging energy with the environment into account and is governed by the impedance of the circuit. For details see chapter 3.2.

To measure the characteristics of a Josephson junction, the junction can be biased by a voltage or a current. According to the Josephson equations there are fundamental differences between the two biasing methods in particular regarding the phase dynamics. The basics of the RCSJ model and the *tilted washboard potential picture* are summarized in the beginning of this chapter (for more details see chapter 3.1). Subsequently, the measured V(I)Cs of a current-biased junction and the I(V)Cs of a voltage-biased junction are described separately to understand the influence of noise and the damping on the junction characteristics. Finally, the phase dynamics of the measured I(V)Cs and V(I)Cs are compared to discuss the coupling to the environment for the two cases.

6.1 The tilted washboard potential picture

The RCSJ model and its mechanical analogon of the *tilted washboard potential* has been described in detail in chapter 3.1. This section is designed as short summary of the main features that are captured by this model.

The RCSJ model gives an intuitive picture of the junctions phase dynamics by translating the properties to the mechanical analogon of a mass particle in the *tilted washboard potential* (see chapter 3.1 figure 3.2). A supercurrent through the junction depends on the phase difference between the two electrodes according to the dc Josephson equation ($I_S = I_C \sin(\phi(t))$).

A voltage drop across the junction contradicts the zero-resistance state of superconductivity and causes the phase relation between the electrodes to change in time ($V = \frac{\hbar}{2e}\frac{d\phi}{dt}$). This in turn results in the ac-Josephson effect which consist in an oscillating current with a voltage dependent frequency, given by the Josephson frequency ($\omega_J = \frac{2e}{\hbar}V$). For more information on the ac Josephson effect in the *tilted washboard potential* picture see appendix A. The RCSJ model describes the properties of Josephson junctions by adding a resistive and a capacitive term in parallel to the Josephson junction to the equivalent circuit (see chapter 3.1 figure 3.5 a)). The current through the circuit can be described by the following equation:

$$I(t) = I_C \sin(\phi(t)) + \frac{\hbar}{2eR}\frac{d\phi(t)}{dt} + \frac{C\hbar}{2e}\frac{d^2\phi(t)}{dt^2} + \delta I \tag{6.1}$$

This is equivalent to the equation of motion of a mechanical particle in a *tilted washboard potential* landscape (see chapter 3.1). The potential of this system is given by $\nabla U = I_C \sin(\phi(t)) - I(t)$ which results in an oscillatory potential landscape that is tilted in the presence of an applied current. In this analogy the location of the particle is given in terms of the phase difference between the two superconductors $\phi(t)$. The dissipative contribution $I_R = \frac{\hbar}{2eR}\frac{d\phi(t)}{dt}$ corresponds to the energy loss of the moving particle. The capacitive term $I_D = \frac{C\hbar}{2e}\frac{d^2\phi}{dt^2}$ captures the movement of the particle around an equilibrium position. Noise fluctuations are considered by δI. The velocity of the phase particle is given by the change of the phase over time which is proportional to a voltage drop across the junction. A steady motion of the particle along the potential landscape results in an oscillating current with the Josephson frequency ω_J. With increasing current, the tilt of the washboard potential effectively reduces the height of the potential maxima until they disappear at the critical current I_C where the particle runs freely down the potential landscape and the Josephson junction turns normal conducting.

When Cooper pairs tunnel coherently the phase particle remains in a minimum of the potential without moving in a preferential direction. The particle oscillates around this equilibrium position with its plasma frequency which is given by $\omega_p = \sqrt{\frac{\hbar I_C}{2eC}}$ with no bias applied.

6.2 Current-biased junctions

The V(I)C of a current-biased Josephson junction is shown in figure 6.1 a). It shows distinct features that can be explained within the *tilted washboard potential* picture. The different regimes are highlighted in green, blue and orange in the measured V(I)C. The current was swept in both directions, from negative to positive values and vice versa.

Increasing the current starting from zero a small but finite voltage is measured (green area). The slope of the V(I)C is caused by phase diffusion and quantified by the *phase-diffusion conductance* G_{PD} . A sudden jump to higher voltage values is observed at the *switching current* I_{sw}. As explained in chapter 3.1 phase diffusion occurs in **overdamped Josephson junctions**. The junction is considered to be overdamped when the phase particle in the washboard potential looses momentum due to dissipation in the system, i.e. starting from a maximum of the potential landscape, dissipation prevents the phase particle from overcoming subsequent maxima. In figure 6.1 b) concept of phase diffusion is depicted in the washboard potential picture. In the presence of noise fluctuation the occasional phase slip can occur in the trapped state. The provided energy enables the particle to overcome a maximum of the potential landscape. The strong dissipation in the system causes the phase particle to be retrapped in one of the next minima. These phase slips give the phase particle a preferential direction along the tilt of the potential landscape and for that reason a finite voltage is measured.

The resistive branch is highlighted in blue in figure 6.1 a). In this regime the phase particle is in the running state as depicted in 6.1 c). The measured switching currents are well below the expected critical current which indicates *premature switching*. Premature switching is a property of **underdamped Josephson junctions**. In underdamped junctions the phase particle does not loose momentum in the running state, i.e. the particle gains enough energy within one period of the potential landscape to overcome subsequent maxima. Premature switching occurs in the presence of noise fluctuations as soon as the phase particle receives enough energy to overcome the first potential maximum. In the absence of damping the running state is sustained without loosing momentum.

The transition from the running state to the trapped state occurs at the *retrapping currents* I_{re}. In figure 6.1 a) retrapping currents occur at much lower values than the switching currents. This hysteretic behaviour is another signature of underdamped Josephson junctions. Starting in the running phase the particle's inertia enables the particle to overcome subsequent maxima. Retrapping currents at small but finite current values may occur due to noise fluctuations. The switching and retrapping transitions are indicated in figure 6.1 d).

In chapter 3.1 the properties of the phase dynamics of Josephson junctions are categorized as underdamped or overdamped, depending on the Steward McCumber parameter $\beta_C = \frac{2e}{\hbar} I_C R_N C$ being larger or smaller than 1, respectively. To explain

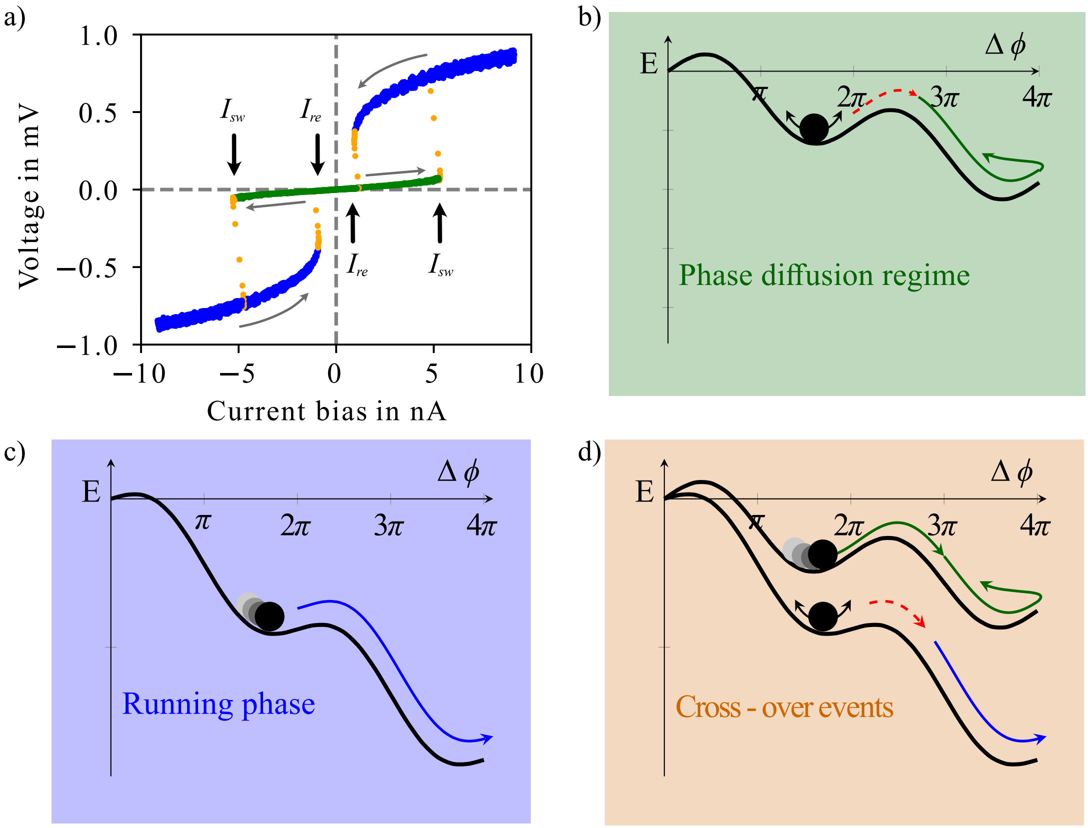

Figure 6.1: Current-biased Josephson junction. a) shows a measured V(I)C at 50 µS. Colours indicate different regimes of the phase state. b)-d) washboard potential for different scenarios indicating the different regimes of the phase states. b) indicates the phase particle in the predominantly trapped state with occasional phase slips giving rise to the finite slope in the V(I)Cs. c) shows the phase particle in the running phase. d) displays the cross over scenarios for retrapping and switching events.

the observation of hysteretic behaviour, premature switching and phase diffusion in the same junction the RCSJ model needs to be adjusted to capture frequency-dependent damping.

The apparent contradiction of a junction that simultaneously shows underdamped and overdamped properties has been resolved by R. L. Kautz and J. M. Martinis [81] by the introduction of **frequency-dependent damping**. By adding an additional RC-component to the existing RCSJ model the damping differs depending on the frequency of the signal. In the predominantly trapped state the particle's movement is determined by frequencies in the order of magnitude of the plasma frequency ω_p. The frequency of the continuous motion of the particle does not have an oscillatory contribution, i.e. the dominant frequency is close to zero. According to this model, the junction's quality factor Q becomes frequency-dependent and results in much higher damping for high frequencies than for low frequencies (chapter 3.1, figure 3.5 b)). This results in phase diffusion for the predominantly trapped particle while the running particle experiences low damping which causes premature switching and hysteresis. Frequency-dependent damping captures the properties of the current-biased V(I)Cs.

6.3 Voltage-biased junctions

The transitions between states in the I(V)Cs in a voltage-biased junction are fundamentally different from the current-biased V(I)Cs as shown in figure 6.2 a). Different regimes are indicated in green, blue and orange colors. At small applied voltages a steep slope in the I(V)C is observed as indicated in geen in figure 6.2 a). High currents are measured at these low voltage values indicate Cooper-pair-related tunneling events. A peak in the curve is reached at V_{sw} from where the tunneling of Cooper pairs is prevented. A reduction of the current is indicated in orange as the junction transitions to the high resistive state. A minimum is reached at finite voltage values V_{re}.
At first glance it is surprising that Cooper pairs may even tunnel when a voltage is applied since it enforces a constant movement of the phase particle along the potential. In the absence of dissipation the junction directly transitions to the resistive state as a consequence. As explained in chapter 3.2, coherent Cooper-pair tunneling is not possible with an applied external voltage. However, Cooper-pair tunneling has been observed for voltage-biased junctions in several experiments [35, 45, 84] and has been explained by incoherent Cooper-pair tunneling in the absence of phase coherence [47, 84] (see chapter 3.2).

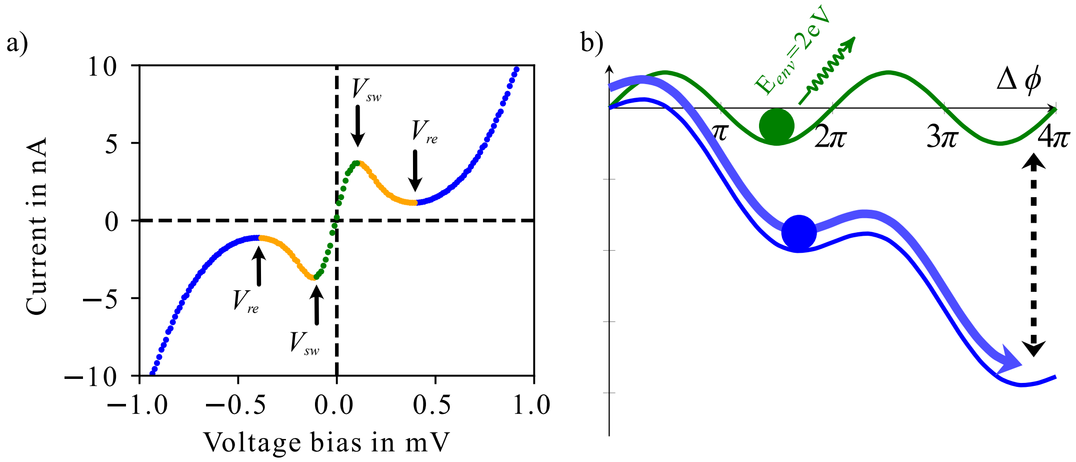

Figure 6.2: Voltage-biased Josephson junction. a) Measured I(V)C with an applied voltage of the same 50 µS junction as in figure 6.1. Colours indicate different regimes. b) P(E)-theory in the washboard potential picture. Whenever energy is dissipated via the environment the phase particle is trapped and Cooper pairs may tunnel (green curve). When there is a voltage drop across the junction the phase is changing in time running down the potential landscape (blue). The ratio of occupancy of the two states is determined by the probability with which the environment absorbs energy (P(2eV)). The average tilt of the potential gives the measured current.

The concept of incoherent Cooper-pair tunneling is based on the interaction of the Josephson junction with the environment in junctions where $E_C >> E_J$. The energy that is provided to the junction by the applied voltage is dissipated elsewhere in the circuit allowing individual Cooper pairs to tunnel through the barrier. The process depends on the probability to dissipate enough energy to allow for a Cooper pair to tunnel and is commonly described by P(E)-theory [46, 47, 84, 85]. The coupling to the electromagnetic environment is given by the impedance $Z(\omega)$ and strongly depends on the details of the measurement setup.

P(E)-theory has been derived in chapter 3.2 and results in I(V)Cs that can be described by

$$I(V) = \frac{\pi e E_J^2}{\hbar}[P(2eV) - P(-2eV)] \text{ [46].} \tag{6.2}$$

The probability function for Cooper-pair tunneling $P(2eV)$ takes the form

$$P(E) = \frac{1}{2\pi\hbar}\int_{\infty}^{\infty} dt \exp(4J(t) + \frac{i}{\hbar}Et) \tag{6.3}$$

where J(t) is the phase-phase correlation function and contains the information of the environmental impedance. $P(2eV)$ gives the probability that the dissipated energy results in the transmission of a Cooper pair through the junction.

With increasing voltage a higher amount of energy $E_{\mathrm{CP}} = 2eV_b$ needs to be transmitted to the environment for each tunneling Cooper pair. As derived in more detail in chapter 3.2 the impedance determines the probability to tunnel Cooper pairs for varying applied voltages. The higher the impedance the more energy can be dissipated and Cooper pairs can tunnel for higher applied voltages. Accordingly, the peak in figure 6.2 at V_{sw} is expected to shift towards higher voltages with increasing impedance (see also figure 3.6).

An attempt to translate these characteristics into the washboard potential picture is shown in figure 6.2 b). Biasing a junction with a voltage changes the control mechanism of the tilted washboard potential picture. Instead of controlling the tilt of the washboard potential by a current, the average velocity of the phase particle is fixed by the external voltage. In the washboard potential picture a voltage drop across the junction corresponds to a phase particle that continuously moves along the potential landscape (ac Josephson effect see appendix A). Without a voltage drop the phase particle remains in the trapped state. The idea of P(E)-theory is that Cooper-pair tunneling is allowed as long as the energy applied to the system of $E = 2eV$ is dissipated to the environment elsewhere. Translating that to the washboard potential implies that the phase particle fluctuates between the running and the trapped state. When the energy provided by the applied voltage is dissipated, the particle is trapped and a Cooper pair can tunnel as depicted in the the green curve of figure 6.2 b). When energy dissipation is not possible the particle goes into the running state as shown in blue in figure 6.2 b). The ratio of occupancy of these two states is determined by the probability function (P(2eV)) as described above.

6.4 Interaction of Cooper-pair tunneling processes with the environment

In the previous sections a Josephson junction discussed for the current- and the voltage-biased case separately. While for the current-biased junction the wahsboard potential provides a good explanation for the observed features, P(E)-theroy was used to explain the I(V)Cs measured with a current bias. Both descriptions rely on the interaction of the junction with the environment. In this section the two biasing methods are compared for Josephson junctions that were formed with different STM tip preparations which results in different noise levels.

In figure 6.3 the characteristics of two Josephson junctions from different preparation are shown. Both junctions were measured with a current and a voltage bias to compare the characteristic features. In figure 6.3 a) and b) the histograms of switching and retrapping currents extracted from the current-biased V(I)Cs are presented for 2000 sweeps in the forward and backward sweep direction. The data was corrected for a bias offset and piezoelectric creep as described in chapter 5.2. Immediately it can be seen that the average switching currents differ significantly for the two data sets. Since both junctions were measured at the same normal state conductance the switching events are noise induced. The exact form of the tip apex influences the noise level in the junction and thereby the extracted switching currents. The higher the noise level in the junction the lower the switching current. Accordingly, the junction with lower switching currents in figure 6.3 a) is considered to have a higher noise level than the junction shown in figure 6.3 b) where the switching events occur at higher currents.

Single V(I)Cs for each of the two junction are compared to the I(V)Cs of the voltage-biased junction in figure 6.3 c) and d). Switching events are indicated by blue symbols, diamonds for the voltage-biased junction and circles for the current-biased case. Retrapping events are marked by orange symbols, again diamonds and circles distinguish the voltage- and current-biased junction. In figure 6.3 c) the characteristics of the junction with the higher noise level are shown. The switching currents are much smaller for the voltage-biased junction (blue diamonds) in comparison to the current-biased junction (blue circle) in this junction. Additionally, the slope of the curve in the Cooper-pair tunneling regime in the current-biased junction corresponds to a phase-diffusion conductance of about $G_{\mathrm{PD}}= 100\,\mu\mathrm{S}$ while the conductance in the voltage-biased junction is half as high with around $G_0 = 50\,\mu\mathrm{S}$. The characteristics of the junction with a lower noise level are shown in figure 6.3 d). The two curves recorded with a current and voltage bias are much more similar. The phase-diffusion conductance in the current-biased junction is determined to be around $G_{\mathrm{PD}}= 130\,\mu\mathrm{S}$ while the conductance in the Cooper-pair tunneling regime for the voltage-biased junction is about $G_0 = 110\,\mu\mathrm{S}$. The voltage-biased junction shows a lower conductance in the Cooper-pair tunneling regime than the current-biased junction for both noise levels. However, the differences are much less pronounced in the junction with

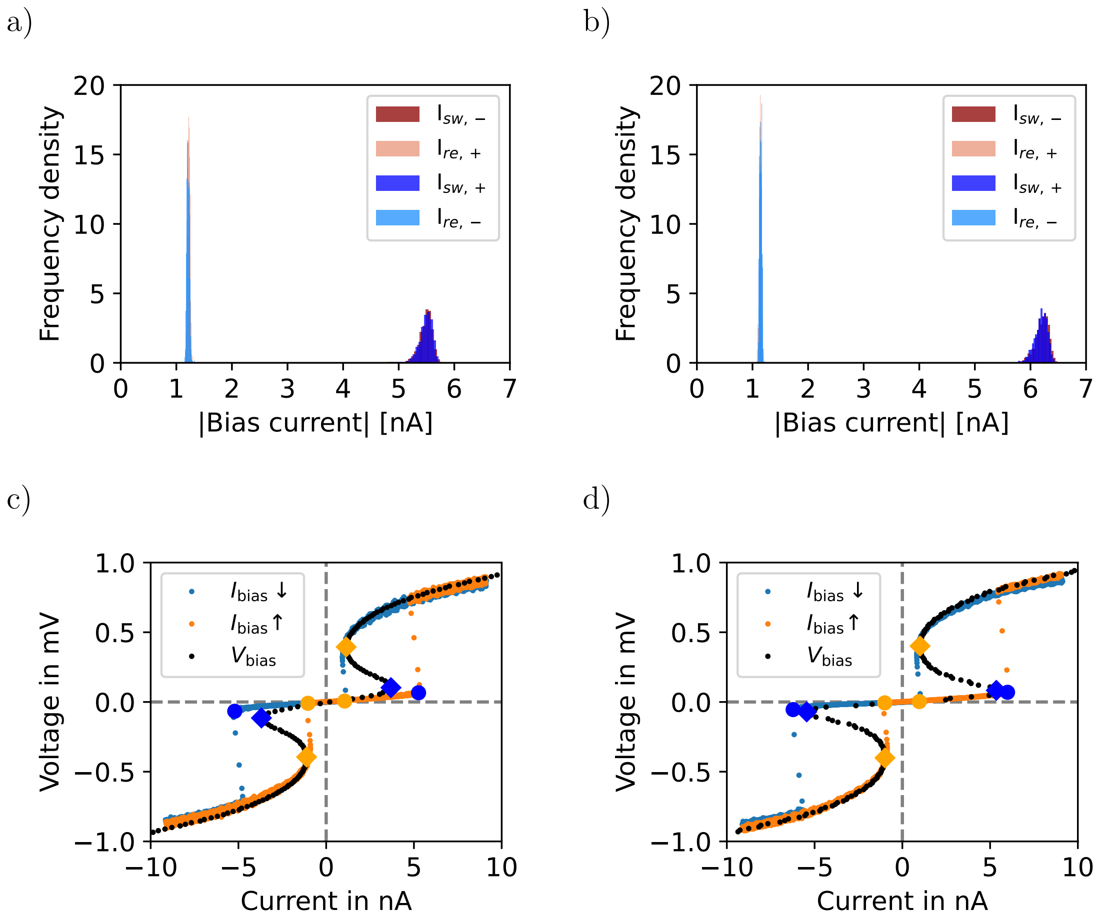

Figure 6.3: Two Pb-Pb Josephson junctions at 50 µS normal state conductance measured with tips from different preparations. The statistical analysis of current-biased measurements is shown in the histograms in a) and b). Absolute values of I_{sw} are larger for the junction in b) which indicates a lower noise level in that junction compared to the junction presented in a). In c) and d) single voltage-biased I(V)Cs are compared to current-biased V(I)Cs. Switching events are indicated by blue symbols and retrapping events by orange symbols. Diamond shapes indicate events in the voltage-biased junction and circles are chosen for the events in the current-biased junction.

a lower noise level.

From the previous discussion a shift of the peak in the voltage-biased I(V)C to higher voltages as well as the change in slope can be explained by an increase of the probability to dissipate higher energies to the environment (see P(E)-theory in chapter 3.2). Furthermore, it was discussed that in the current-biased junction the slope in the phase-diffusion regime is dominated by noise fluctuations (see damping properties in chapter 3.1). The difference between the voltage- and current- biased measurements in figure 6.3 c) indicates that the influence of noise fluctuations on the junction characteristics depends on the biasing method. At lower noise levels the biasing methods yield much more similar results as shown in figure 6.3 d) compared to the junction with a higher noise level in figure 6.3 c). Voltage-biased Josephson junctions seem to be affected more strongly by an increasing noise level.

However aside from the noise level of the junction, the bias sweep rates can influence the phase dynamics of the junction. Especially for the current-biased measurements the sweep rate is expected to influence the observed switching events. Due to the statistical nature of escape events the waiting time at each current value influences the probability for a switching events to occur. While the current of the presented measurements was swept with a high rate of 270 nA/s the voltage bias was swept with a much lower rate of 2 mV/s. Investigating the influence of different sweep rates on the characteristics of current- and voltage- biased measurements is an interesting prospect for future investigations.

6.5 Normal state conductance dependence of Josephson characteristics

One of the main advantages of forming Josephson junctions in an STM is the control of the junction conductance by simply changing the tip-sample distance. The switching currents of current-biased Josephson junctions for varying normal state conductances where extracted from 500 sweeps. In figure 6.4 a) the average switching currents and standard deviation for a range of normal state conductances are shown for two sets of current-biased measurements with two different tip preparations. Both data sets show slightly different switching currents due to different noise levels. For a strictly current-biased junction in the absence of noise fluctuations switching currents are expected to scale with the critical current of the junction as derived by V. Ambegaokar and A. Baratoff [78] as expressed in equation 3.3 and explained in chapter 3.1. This is clearly not the case for the Josephson junctions formed in an STM. The fits in figure 6.4 a) assume a quadratic dependence of the switching current on the normal state conductance. According to equation 6.2 derived by P(E)-theory a quadratic dependence of the current on the Josephson energy is expected for Josephson junctions that are strongly coupled to the environment. The Josephson energy is directly proportional to both the critical current and thereby to the normal state conductance.

Extracting the phase-diffusion conductance G_{PD} that is measured as the slope of the V(I)-curves in the low-voltage regime shows that I_{sw} and I_{re} depend linearly on G_{PD} for both data sets (figure 6.4 b)). The slope of I_{sw} over G_{PD} corresponds to a characteristic voltage at which the junction switches to the resistive state. This voltage reflects the average energy that the junction is able to dissipate before the junction switches into the resistive state. The junction switches at the same voltage value for all measured normal state conductances, i.e. the same amount of energy is dissipated.

6.6 Frequency-dependent damping and P(E)-theory

Previously we discussed the characteristics of the current and voltage-biased junctions separately. The RCSJ model is well suited to explain the phase dynamics of the current-biased junction while the P(E)-theory shows good agreement with the voltage-biased characteristics. We also saw that both biasing methods may give similar results when extracting switching and retrapping currents. The switching currents are affected by the noise level in the junction, however, the voltage-biased curve is influenced differently from the current-biased curve. In addition, we found that the switching events of the current-biased junction follow a quadratic dependence on the normal state conductance which is a strong indication that the junction

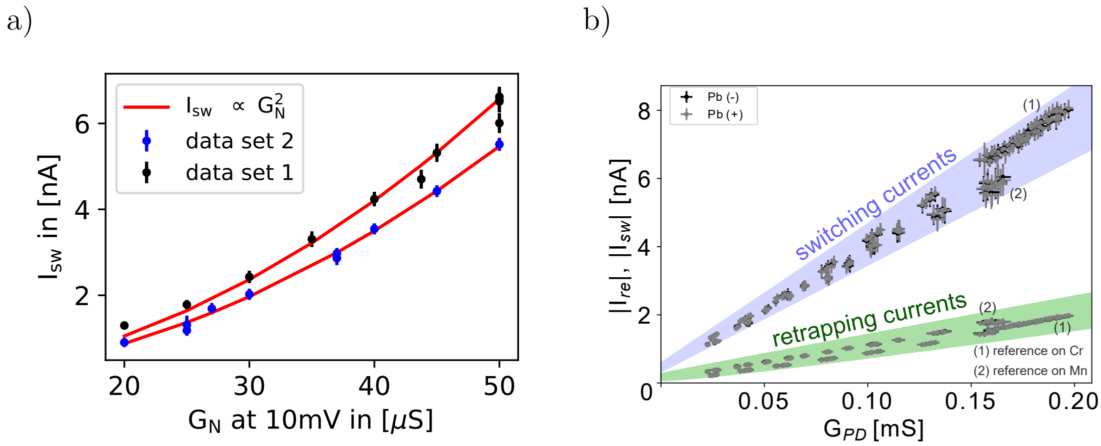

Figure 6.4: Dependence of Josephson junction characteristics on the normal state conductance. Two datasets of Josephson junctions at various normal state conductances (set point current at 10 mV) were recorded with different tip preparations. In a) the dependence of the switching currents on the normal state conductance shows a quadratic dependence. Plotting the switching and retrapping currents over the phase-diffusion conductance in b) shows a linear dependence.

couples to an environmental impedance.

The treatment of the voltage-biased curve with P(E)-theory was explained in the washboard potential picture. It is assumed that the junction constantly fluctuates in and out of the Cooper-pair tunneling state depending on the possibility to dissipate energy to the environment. This effect results in an average tilt of the washboard potential picture that corresponds to an average current that is measured at finite voltages. In the current-biased junction energy is dissipated via damping in the phase-diffusion regime in the washboard potential picture. In this case the energy is also dissipated to the environment.

For a better understanding of the mechanisms that dominate the phase dynamics in the junction an equivalent circuit of our measurement setup is shown in figure 6.5. In this circuit we include the wire impedance by an $R_W C_W$-link in the bias line which we call $Z_W(\omega)$. Additionally we include another $R_S C_b$-component that governs frequency-dependent damping as suggested by R. L. Kautz and J. M. Martinis [81] for current-biased junctions in parallel to the junction ($Z_f(\omega)$). A large resistor R_B is included in the bias line which can be bypassed by a switch. A current bias is achieved by opening the bypass switch.

Including R_B in the circuit affects the properties of the circuit significantly. For the current-biased junction the resistance of the wires R_W is negligible compared to the series resistor R_B. However the parallel $R_S C_b$-component in parallel to the junction strongly influences the outcome. As described in chapter 6.2 this component causes the damping of the junction to be frequency dependent and thereby explains the observed features of the V(I)Cs. The $R_S C_b$-component can be regarded as a way to interchange energy with the environment in the current-biased junction.

On the other hand, in the voltage-biased junction, R_W dominates the impedance of the bias line. The parallel components, however, do not influence the voltage drop at the Josephson junction. The line impedance is responsible for the energy dissipation before reaching the Josephson junction itself.

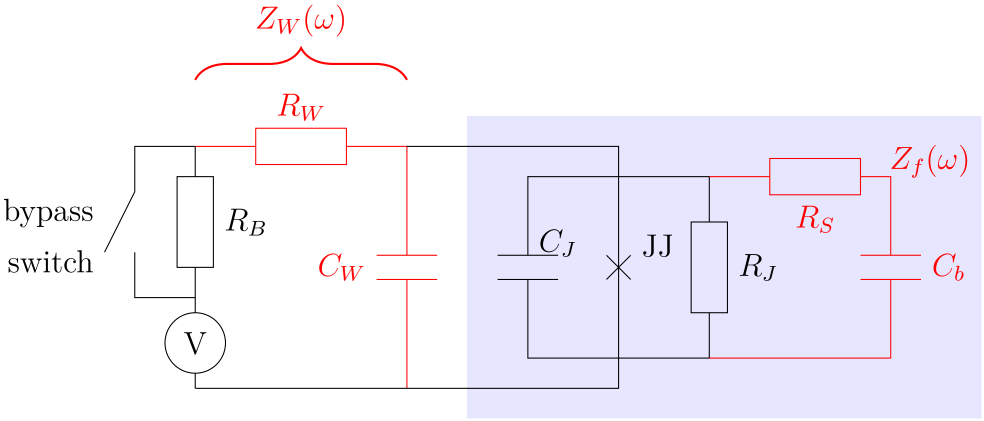

Figure 6.5: Equivalent circuit of the measurement setup including the impedance of the wires $Z_W(\omega)$ and the impedance of the electromagnetic environment of the junction $Z_f(\omega)$.

CHAPTER 7

HIGH FREQUENCY IRRADIATION OF JOSEPHSON JUNCTIONS

High frequency (HF) irradiation was applied to the STM Josephson junctions by an antenna located near the junction. Frequencies (ω_r) between 30 and 40 GHz were applied. As discussed in chapter 3.3 voltage-biased STM junctions absorb energy from the irradiation by photon-assisted tunneling. Tunneling charge carriers absorb photons from the HF-field, opening additional discrete tunneling channels. This results in a splitting of the peaks of the dI/dV spectra as resonance conditions are met when the energy difference across the junction matches the energy of the photons generated by the HF-field ($eV_{\mathrm{dc,bias}} = n\hbar\omega_r$). Several photons n can be absorbed as the amplitude of the irradiation increases.

It has been shown that the process of photon-assisted tunneling can be reproduced accurately by the model of P. K. Tien and J. P. Gordon [49]. For Josephson junctions the model is adjusted to transfer particles with a charge of 2e instead of one electron (see chapter 3.3 and [50, 51]). In chapter 5.3 it has been shown that this model is well suited to simulate the splitting of the coherence peaks as well as the resonances due to Andreev reflections and Cooper-pair tunneling [52].

It was discussed in chapter 3.3 that if there is phase coherence across the Josephson junctions Shapiro steps instead of photon-assisted tunneling are observed. Shapiro steps are resonant excitations of the time-dependent phase difference across the junction. As discussed in the chapter 6 the voltage- and current-biased junction differ in their interaction with the environment and show differences in their phase dynamics.

This chapter aims at understanding the interaction of the HF-field with the current-biased Josephson junctions as well as the differences compared to voltage-biased Josephson junctions in the presence of HF irradiation. First the theoretical concepts of photon-assisted tunneling and Shapiro steps will be revisited. Subsequently, the experimental findings for a current-biased junction at 60 µS with HF irradiation of

40 GHz are presented. For experimental details and the data analysis see chapter 5.3. The current-biased spectra are compared to measurements that were performed in parallel with a voltage bias.

7.1 Concepts of photon-assisted tunneling and Shapiro steps

The excitations of Josephson junctions under the influence HF irradiation were explained in detail in chapter 3.3. It was found that incoherent absorption of photons by the tunneling charge carrier results in photon-assisted tunneling while the resonant interaction of the phase particle with the electromagnetic environment results in Shapiro steps. Here, the relevant physical picture to understand the experimental results is briefly summarized again.

Photon-assisted tunneling of Cooper pairs

Photon-assisted Cooper-pair tunneling processes treat Cooper pairs as individual particles with twice the electron charge that absorb or emit photons from the HF-field during the tunneling process. It is assumed that the timescale of subsequent tunneling events is much larger than the phase coherence time. The model of P. K. Tien and J. P. Gordon for single-electron processes suits Cooper-pair tunneling events by assuming particles carrying twice the electron charge [50, 51]. Additional tunneling channels are accessible as a discrete number of photons is absorbed. The amplitude of the HF irradiation determines the number of photons that can be absorbed by the junction. According to the Tien-Gordon equation for Cooper pairs the measured current is modelled by

$$I(t) = \sum_n J_n^2(\frac{2eV_{ac}}{\hbar\omega_r}) I_{qp}^0(V + \frac{n\hbar\omega_r}{2e}). \tag{7.1}$$

Steps in the measured current occur whenever the voltage bias corresponds to multiples of the photon energy ($2eV_{dc,n} = n\hbar\omega_r$). The square of the Bessel-functions (J_n) determines the height of the current steps. It has been shown that the measured dI/dV curves in dependence of the irradiation amplitude can accurately be reproduced by this model (see chapter 5.3)[86].

Shapiro steps in Josephson junctions

Shapiro steps consist in sharp resonances whenever the Josephson frequency ($\omega_J = \frac{2e}{\hbar}V(t)$) matches multiples of the modulation frequency $n\omega_r = \omega_J$. The Josephson frequency corresponds to the velocity of the phase particle following the periodicity of the washboard potential. In the V(I)Cs the resonances are observed as plateaus

at discrete voltage values of $V_{dc,n} = n\frac{\hbar\omega_r}{2e}$. Resonance conditions are met for integer values of n which is equivalent to the number of periods in the washboard over which the phase particle is resonantly excited. As has been found in chapter 6 the phase dynamics in a Josephson junctions are influenced by the interaction of the junction with the environment. In this section voltage and current- biased junction are treated separately. For the current-biased junction different damping regimes inlfuence the observation of Shapiro steps
When a **voltage-biased** junction is modulated by an ac-signal the time dependent voltage takes the form

$$V(t) = V_{\mathrm{dc,bias}} + V_{ac}\cos(\omega_r t) = \frac{2e}{\hbar}\frac{d\phi}{dt} \tag{7.2}$$

with the HF amplitude V_{ac} and frequency ω_r. This results in a complex expression for the time dependent phase difference:

$$\phi(t) = \frac{2e}{\hbar}(V_{dc}t + \frac{V_{ac}t}{\omega_r}\sin(\omega_r t) + \phi_0) \tag{7.3}$$

With the dc Josephson equation $I(t) = I_C \sin(\phi(t))$ the current-voltage characteristics can be expanded by Bessel functions $(J_n(x)))$. Solving the equation results in current steps at discrete voltage values at $V_{dc,n} = n\frac{\hbar\omega_r}{2e}$. The current can take values between $I_{qp} - I_C J_n(n\frac{V_{ac}}{V_{dc}}) < I(V_{dc,n}) < I_{qp} + I_C J_n(n\frac{V_{ac}}{V_{dc}})$ for each voltage value, where I_{qp} corresponds to the quasiparticle current and I_C the critical current of the junction.
With a dc **current bias** $I_{\mathrm{dc,bias}}$ applied to the junction, the external HF-field modulates the signal by $I(t) = I_{\mathrm{dc,bias}} + I_{ac}\sin(\omega_r t)$. In the washboard potential picture this corresponds to a periodic modulation of the washboard potential's tilt with the frequency ω_r and amplitude I_{ac}. Resonances appear when the HF frequency matches the Josephson frequency of the moving phase particle, effectively locking the speed of the phase particle to multiples of the potential's periodicity. Experimentally, this results in measuring resonances at discrete voltage values of $V_{dc,n} = n\frac{\hbar\omega_r}{2e}$. Depending on the amplitude of the HF irradiation the number of available resonances n varies as the particle may resonantly be excited over several maxima of the washboard potential landscape.
In chapter 3.3 Shapiro steps in a current-biased junction were discussed in the two scenarios of over- and underdamped junctions. In figure 7.1 the expected V(I)Cs for the two cases are presented.
In the noise-free current-biased **overdamped junction** the particle in the trapped state cannot be excited resonantly as the phase has no preferential direction. When the applied dc current reaches $I_b = I_{\mathrm{sw}} - I_{ac}$ the junction switches to the resistive state due to the ac modulation. As soon as the phase particle is able to escape the potential minimum the voltage increases with increasing current bias which now allows the junction to reach resonant conditions at $V_{dc,n}$. This results in voltage

plateaus at increments n of $\frac{\hbar\omega_r}{2e}$ in the normal state V(I)C of the junction, shown in the blue curve of figure 7.1.

Noise induces escape events that lead to phase diffusion in the otherwise trapped state in overdamped junctions. When the resulting average voltage meets the resonance conditions a voltage plateau occurs for an increasing applied current.

Assuming an **underdamped junction** the discrete resonant excitations of the phase particle induced by the HF-field are equally stable for any applied current below I_{sw} as the system does not loose energy due to damping. The phase particle may assume any discrete velocities that are within the resonance conditions. Experimentally, the system transitions sharply between discrete voltage resonances as shown in the red curve in figure 7.1. The history of the system determines the resonance of the phase particle, i.e. the inertia of the phase-particle determines its velocity within the HF-field. That means that for each applied current the measured voltage can take values of $V_{dc,n}$ with n depending on the HF amplitude. This causes hysteretic behaviour between sweep directions of the current bias as the transition between steps depend on the previous state. These transitions are also subject to statistical influences.

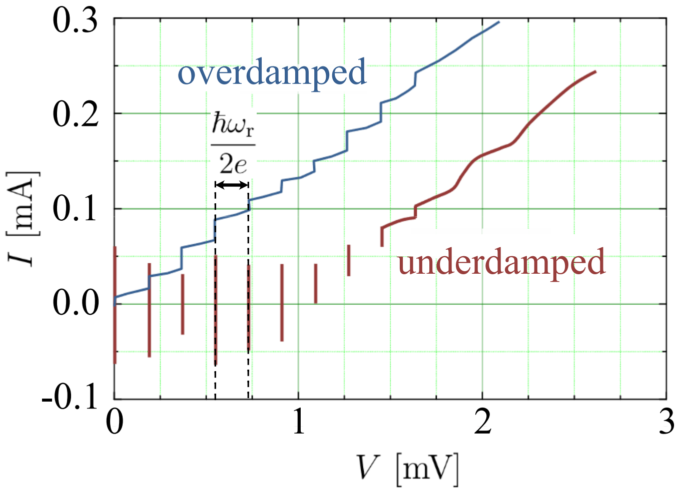

Figure 7.1: Shapiro steps in an overdamped and underdamped current-biased junction. The overdamped junction corresponds to the blue curve and the underdamped junction to the red curve. Both curves show steps at the same voltage values. For the overdamped junction the transitions are well defined as the voltage increases gradually until another resonance condition is met. For the underdamped junction multiple resonances are available for the same current bias values. The transitions between resonances are not well defined and depend depend on the history of the system. Adapted from [77].

7.2 Resonances in current-biased Josephson junctions

A Pb-Pb Josephson junction at 60 µS normal state conductance was investigated under 40 GHz HF irradiation. More data on junctions with varying HF frequencies are summarized in appendix C. In figure 7.2 exemplary V(I)Cs are shown for varying amplitudes of the HF-field. The presented curves are averaged over 100 sweeps to capture the statistics of the events.

In figure 7.2 a) the V(I)C in the absence of irradiation is shown. The charactersitics of the junction change significantly as soon as the HF irradiation is applied. In figure 7.2 b) the V(I)C under HF irradiation for a small amplitude is shown. Immediatly a reduction of the switching current and an increase of phase diffusion in the Cooper-pair tunneling regime is observed in comparison to the junction in the absence of irradiation. At the same time the absolute values of the retrapping currents increases effectively reducing the observed hysteresis between biasing directions. These are effects that can be explained by an increase of the noise level in the junction and indicate that escape events are enabled by the incoherent absorption of energy from the HF-field.

Upon further increasing the HF amplitude two resonances appear at positive and negaitve voltage values as shown in figure 7.2 c). In a current-biased junction a step in the V(I)C marks the transitions between discrete voltage resonances at $V_{dc,n} = n\frac{\hbar\omega_r}{2e}$, with n depending on the amplitude of the HF irradiation. The current value at which the junction transitions between voltage plateaus depends on the direction of the applied current, i.e. a hysteresis of the step is observed with respect to the sweep direction. Additionally, it is observed that the plateaus at finite voltage are not flat as expected for coherent absorption of the HF irradiation in a current-biased Josephson junction but have a finite slope. The observed slope on the plateaus is related to the incoherent interaction with the environment resulting in additional escape events causing phase diffusion.

The voltage values of the observed plateaus appear to increase continuously with increasing amplitude (figure 7.2 c)-e)). This indicates that transitions between voltage resonance with higher values of n occur. In figure 7.2 f) second resonance is observed at zero voltage. The transitions between the voltage resonances still show hysteretic behaviour.

As the amplitude further increases, more voltage plateaus are observed with higher increments of n. Four plateaus are recognizable in figure 7.2 g) and five plateaus in figure 7.2 h). However, the transitions show less and less hysteresis until it vanishes completely.

Single V(I) curves as presented in figure 7.2 can be summarized in a stacked color plot as shown in figure 7.3. The two sweep directions are plotted individually in figure 7.3 a) and b). for an increasing amplitude of the HF irradiation. To highlight the transitions between the voltage plateaus the derivative of the V(I) curves

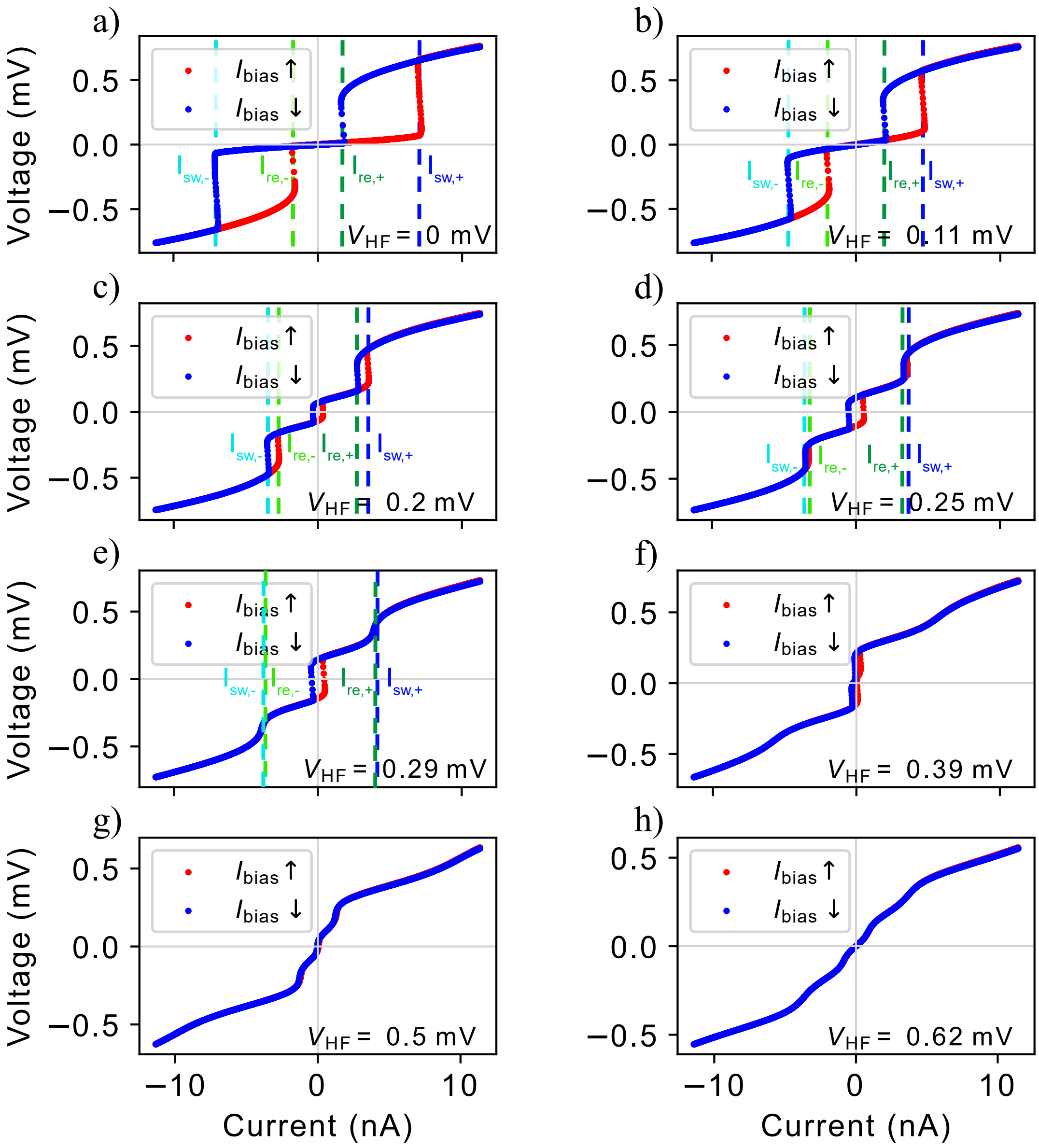

Figure 7.2: Example I(V)Cs for different HF amplitudes at 40 GHz of a 60 µS Josephson junction set at 10 mV. The curves show the average of 100 sweeps to capture the statistics of the process. The spectra were chosen to highlight the hysteresis that is observed for the HF induced steps as well as the switching currents.

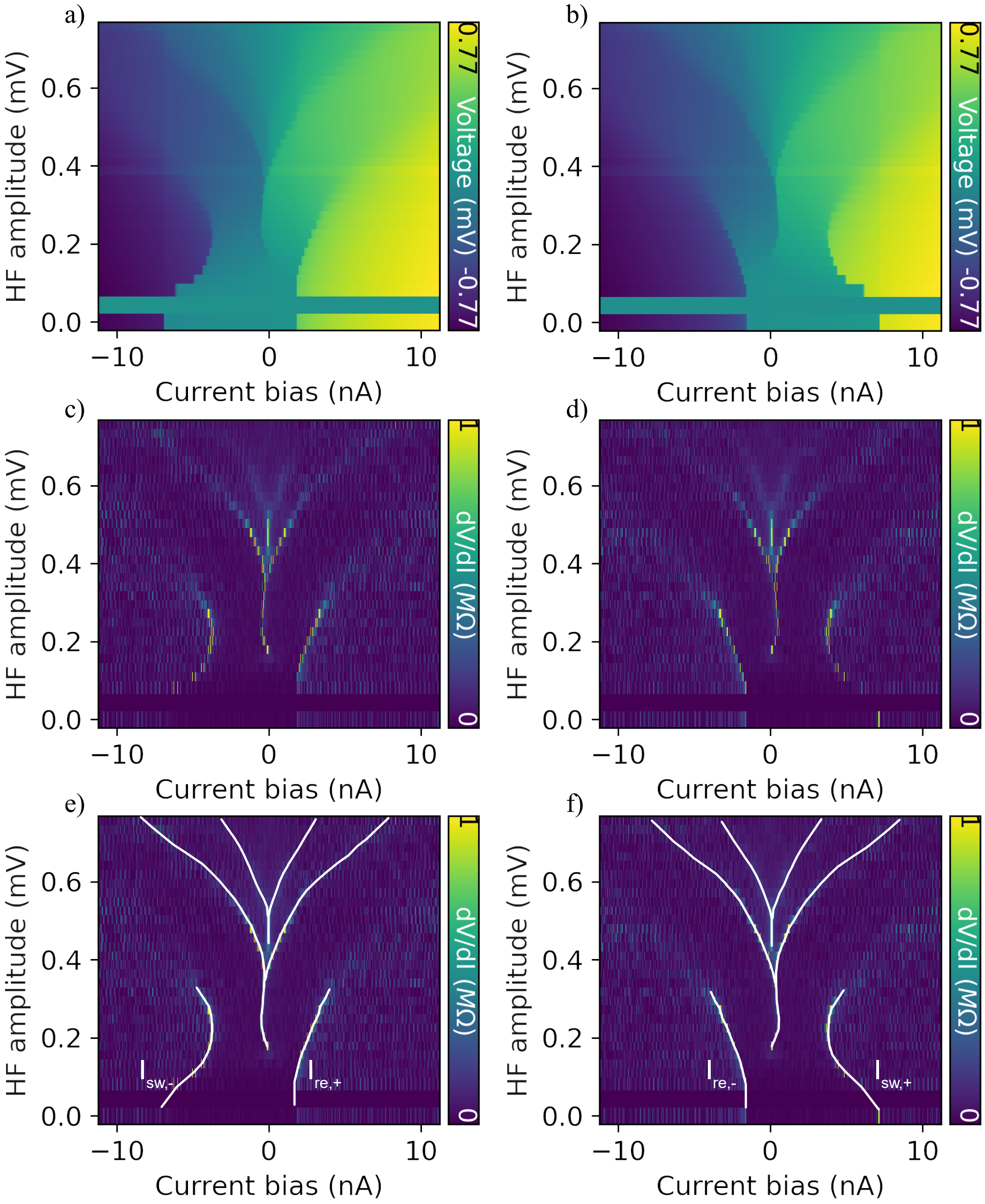

Figure 7.3: 2D-colormaps of current-biased Josephson junctions irradiated by 40 GHz irradiation. a) and b) show a stacked color plot of the V(I)Cs for decreasing and increasing current sweeps, respectively. To highlight the voltage steps occurring in the spectra a the derivatives of the same data is shown in c) and d). In e) and f) guides to the eye are added for the steps occurring with increasing amplitude.

is plotted in figure 7.3 c) and d).

Guides to the eye are included in figure 7.3 e) and f). With increasing HF amplitude the values of switching currents start to continuously decrease for both sweep directions while the retrapping currents increase. Consequently, the difference between switching and retrapping currents becomes less pronounced until it vanishes. Once both events happen at similar current values they start shifting towards larger current values as the HF amplitude increases and eventually smear out. The disappearance of the hysteresis can be a result of an increasing noise level in the junction. As the first resonance appears in figure 7.3 hysteresis for the transition between voltage steps is observed as a curvature in opposite directions for the forward and backward sweep. The spectra become more symmetric as the amplitude increases. Hysteresis indicates the presence of phase coherence in the junction. In the washboard potential picture the inertia of the phase particle results in the direction dependence of the transition between resonances. As described in the beginning of this chapter hyseresis is observed for underdamped junctions. Additonally, zero-voltage crossings are observed in the V(I)Cs in figure 7.2 c) to e), i.e. the transition between resonances occurs at slightly positive current values for the upwards sweep while the transition of the downward sweep happens at slightly negative values. In literature these kinds of steps are known as zero-crossing steps and are observed in underdamped Josephson junctions [6, 87, 88].

The hysteretic transition between resonances indicates phase coherence and is expected to be observed in underdamped Josephson junctions. At the same time however, the voltage resonances are not sharp and show signs of phase diffusion as explained above. Phase diffusion is related to the incoherent absorption of energy from the electromagnetic environment. It is found that phase diffusion increases with increasing irradiation frequency and at the same time switching currents reduce and retrapping currents increase. These features can be correlated to an increasing noise level in the junction and indicate incoherently tunneling Cooper pairs.

Similar effects have been observed in literature. T. F. Q. Larson *et al.* [103] investigated current-biased graphene-based Josephson junctions and observed hysteretic zero-crossing steps. Y. Koval *et al.* [104] observed Shapiro steps at the same time as phase diffusion in Nb/AlO$_x$/Nb Josephson junctions. They observed an enhancement of the phase diffusion by the application of the electromagnetic field while at the same time resonances with a finite slope appeared.

7.3 Comparison of voltage- and current-biased junctions under HF irradiation

In chapter 6 we discussed differences between the voltage- and the current-biased characteristics of STM Josephson junctions. The phase dynamics of the junctions are influenced differently by external fluctuations. It was suggested that while for the voltage-biased junction the in-line impedance dominates the characterisitcs of the junction while the parallel impedance is more relevant for the current-biased case.

Previous experiment have shown photon-assisted tunneling in voltage-biased STM Josephson junctions. The measured data is well reproduced by the adjusted model

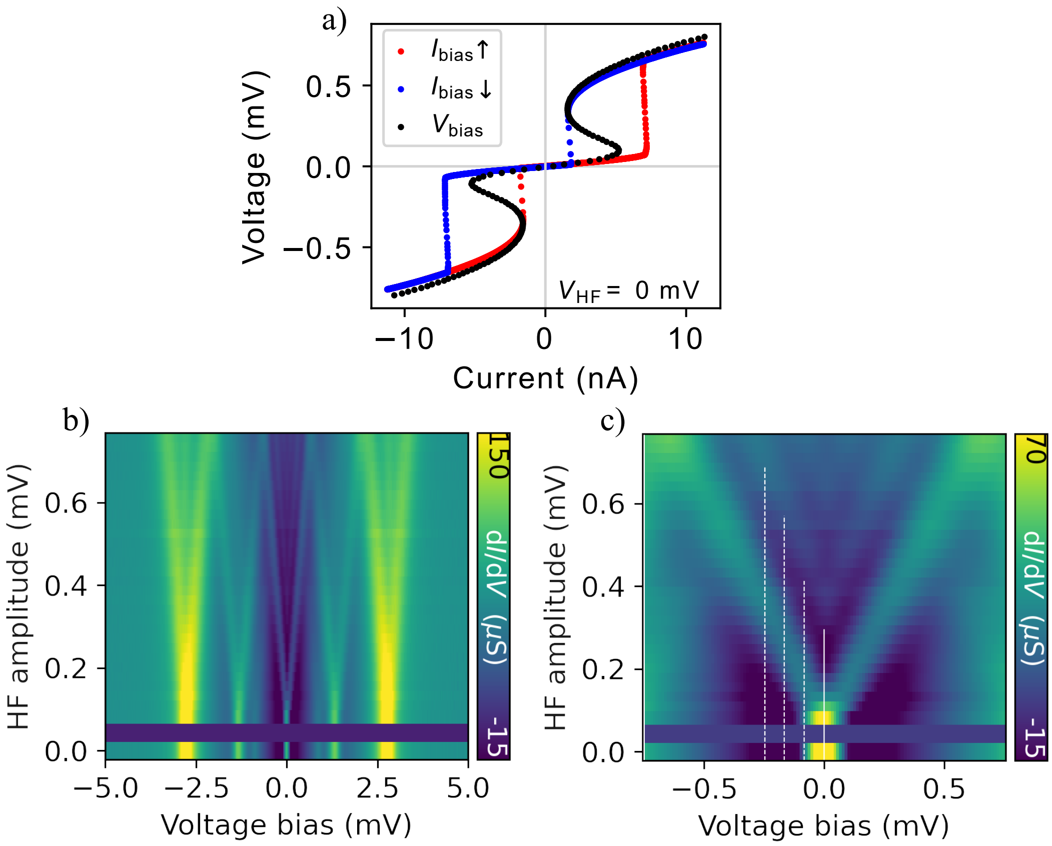

Figure 7.4: HF irradiation of the voltage-biased Josephson junction at 60 µS. a) shows a comparison of the voltage- and current- biased junction in the absence of HF irradiation. b) and c) show the color plots of the voltage-biased dI/dV spectra with increasing HF amplitude at 40 GHz irradiation. b) shows the whole superconducting gap and the splitting of the coherence peaks, Andreev reflections and Josephson peak. c) is a zoom-in on the Josephson peak displaying the resonances in more detail. White dashed lines indicate the resonances with $V = n\frac{\hbar\omega_r}{2e}$.

by P. K. Tien and J. P. Gordon as has been shown in chapter 5.3. In this section the behaviour of current- and voltage-biased Josephson junctions under the influence of HF irradiation are compared.

As the current-biased junction in the presence of HF irradiation was already described in detail in the previous section we will focus first on the voltage-biased junction under the influence of HF irradiation. In figure 7.4 a) the stacked color plot of the full-range dI/dV spectra recorded on the junction with 60 µS normal state conductance is shown. The coherence peaks, the Andreev reflection peaks and the Josephson peak split with increasing HF amplitude. It was already discussed in chapter 5.3 that the peaks all split in accordance with the Tien-Gordon model when taking into account the number of tunneling particles. A zoom-in on the Josephson peak reveals the splitting of the zero-voltage peak with a spacing of $V_{dc,n} = n\frac{\hbar}{2e}\omega_r$ (white lines in figure 7.4 c)).

To compare these resonances to the spectra obtained with an applied current bias, selected curves for both biasing methods are presented in figure 7.5. The orange dashed lines indicate the spectra that were chosen for the comparison in the stacked color plots of the voltage- and current- biased junction (figure 7.5 a) and b), respectively). The discrete values of $n\frac{\hbar\omega_r}{2e}$ are indicated by white lines in figure 7.4 a). The first resonance is clearly seen in figure 7.5 c) for both current- and voltage- biased junction. The switching current is still slightly reduced for the voltage-biased junction in comparison to the current-biased junction. At the first resonance at $\pm\frac{\hbar\omega_r}{2e}$ a step occurs in both current and voltage bias similarly.

As the amplitude increases, the next resonance appears at $\pm 2\frac{\hbar\omega_r}{2e}$ (figure 7.4 d)). With both biasing methods a zero-crossing step is observed as the voltage stays positive (negative) when the current reverses sign from positive (negative) to negative (positive). In the current-biased junction this results in the observed hysteresis between forward and backward sweep while for the voltage-biased junction this results in a non-monotonic behaviour of the curve between the two steps as observed in figure 7.5 d). It also seems that the slopes of the individual steps differ slightly for the two biasing methods. As observed already in figure 7.4 a) the slope in the low-voltage state of the junction is governed by different impedances for the current- and voltage- biased measurements. The same seems to apply the slope of the curves under HF irradiation.

For higher applied current and voltage biases the curves do not completely overlap which is a bit surprising as no differences between current- and voltage- biased measurements are expected outside of the Cooper-pair tunneling regime. It may be an artefact of the current biasing method as the junction resistance at these values becomes closer to the bias line resistor. Other than that the current and voltage-biased curves in figure 7.5 e)-h) are all quite similar as the HF amplitude is increased further and more steps appear at the expected voltage values. The only difference being the hysteresis in the current-biased steps that is not reproduced by the voltage-biased curves.

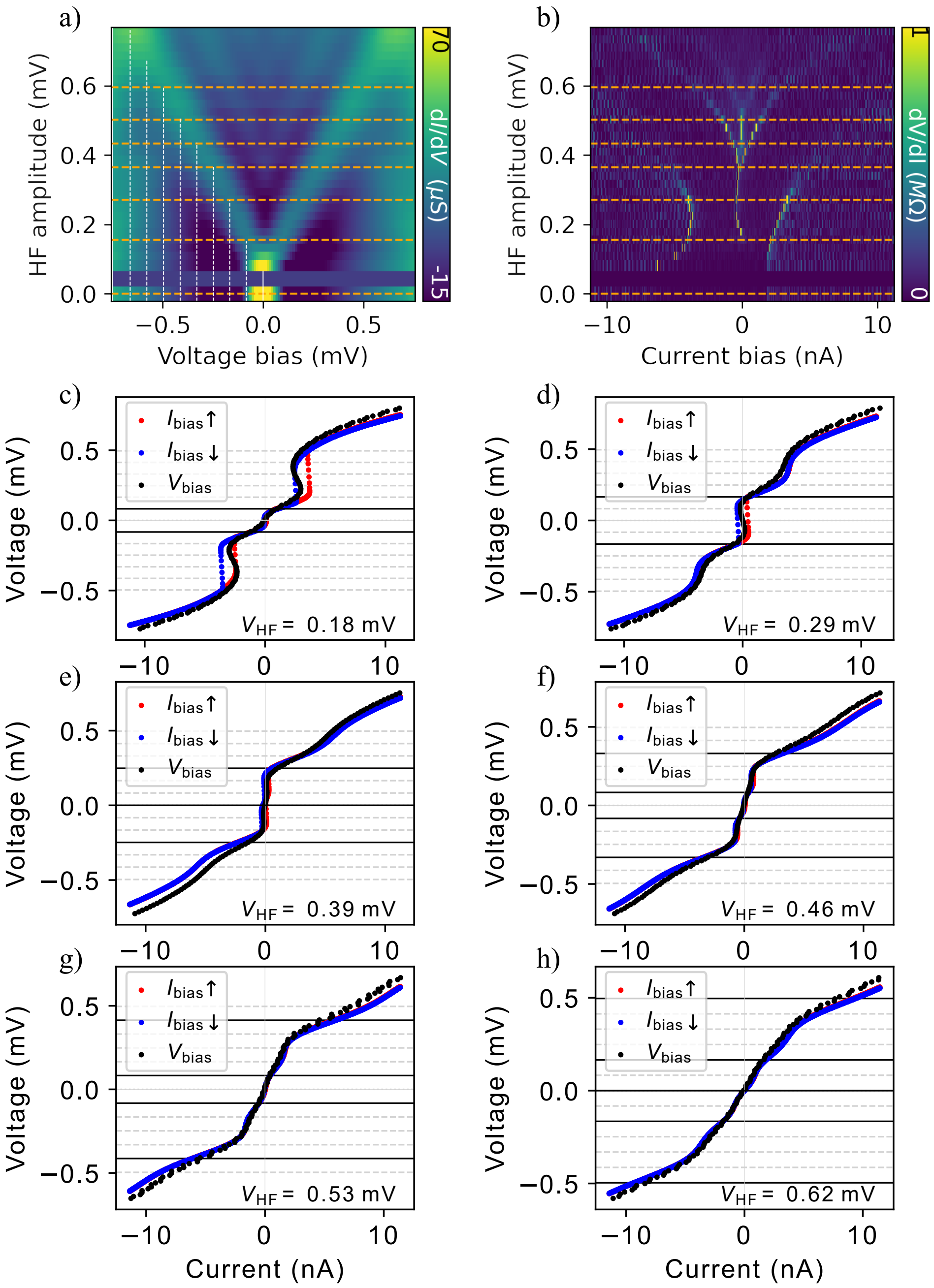

Figure 7.5: Comparison of I(V)Cs and V(I)Cs of the 60 µS junction for different HF amplitudes at 40 GHz. a) and b) show the color plots of the voltage-biased dI/dV spectra and the derivative of the current-biased spectra respectively in dependence of the HF amplitude. Orange lines indicate the location for which example spectra are plotted below in c) to h). White lines indicate $V_{dcn} = n\frac{\hbar}{2e}\omega_r$ with $n = 1...8$. Spectra were selected to highlight the steps within the spectra. c) to h) show examples of current- and voltage- biased characteristics for comparison. Dashed lines indicate V_{dcn} while the solid lines highlight the step voltage for the chosen amplitude.

The fact that the I(V)Cs and V(I)Cs behave quite similarly when the HF is applied indicates that the occurrence of the steps is not an effect of phase coherence across the Josephson junction. Since the model of P. K. Tien and J. P. Gordon results in a good agreement with the measured data, incoherent photon-assisted tunneling of Cooper pairs is the most likely source of the observed steps. However, the hysteretic behaviour of the current-biased junction indicates a phase correlation between tunneling events. This together with the slightly different slopes observed for the individual steps indicates that there might be some phase coherence that is strongly masked by the noise within the junction. The timescales of this coherence is probably very short lived and can only be observed with a free running phase as provided by the current-biased junctions.

CHAPTER 8

MAGNETIC ADATOMS IN JOSEPHSON JUNCTIONS

Most of the results presented in this chapters are published in:

> Martina Trahms, Larissa Melischek, Jacob F. Steiner, Bharti Mahendru, Idan Tamir, Nils Bogdanoff, Olof Peters, Gaël Reecht, Clemens B. Winkelmann, Felix von Oppen and Katharina J. Franke,
> *"Diode effect in Josephson junctions with a single magnetic atom"*,
> Nature **615**, 628-633 (2023).
> `https://doi.org/10.1038/s41586-023-05743-z` [1].

The original data and self-written Python routines used for the analysis can be found in [102].

As discussed in chapter 2.3 magnetic adatoms on a superconducting surface induce YSR states. Figure 8.1 a) and c) show dI/dV spectra measured on single Cr and Mn adatoms. For both atoms three different YSR states can be resolved in STM experiments (indicated by greek letters). Potential scattering results in electron-hole asymmetry and causes different intensities of the peaks for electron and hole tunneling processes on the positive and negative bias side. By approaching the tip to the surface of the substrate the normal state conductance of the junction can be controlled. At a normal state conductance of 50 µS the dI/dV spectrum of pristine Pb-Pb junction shows multiple Andreev reflections as displayed in the background of figure 8.1 b) and d). In the presence of YSR states, additional multi-particle tunneling processes become available. The following processes occur but cannot be assigned unambiguously due to the finite energy resolution of the experiments:

- Andreev reflections by the coherence peaks at $E_A = 2\Delta/n$ (n > 2...)
- resonant Andreev reflections at $E_{\mathrm{A,resonant}} = \epsilon_{\mathrm{YSR}} + \Delta$
- Andreev reflections through YSR states at $E_{\mathrm{A,YSR}} = \epsilon_{\mathrm{YSR}}$

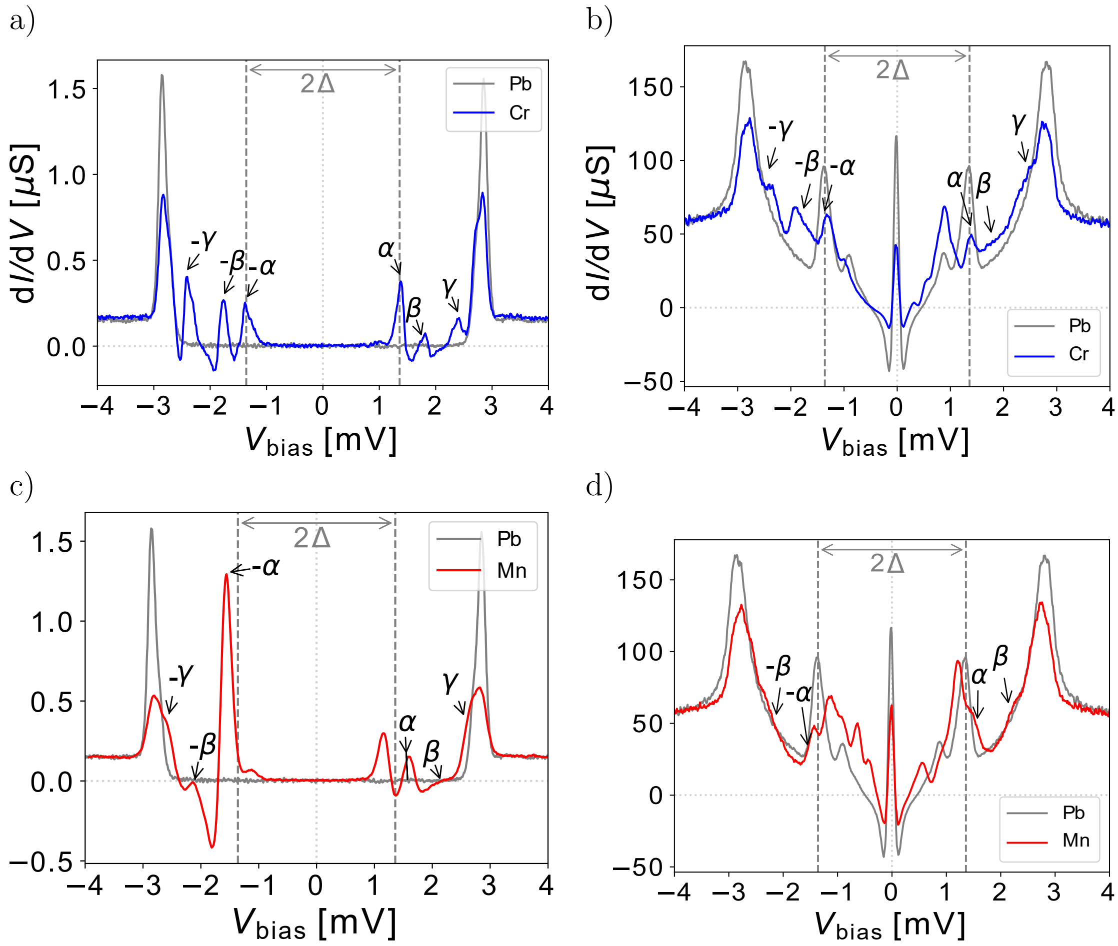

Figure 8.1: dI/dV spectra recorded on single Mn and Cr adatoms in the up configuration on the Pb(111) surface for high and low junction conductances. YSR states are indicated by α, β and γ. In the background reference measurements on a pristine Pb-Pb junction are shown. In a) and c) single electron tunneling processes are dominant at a normal state conductance of $G_{\mathrm{N}} = 0.125\,\mu\mathrm{S}$ for Cr and Mn adatoms, respectively. Asymmetric intensities of the peaks are observed in both spectra due to electron-hole asymmetry. In b) and d) dI/dV spectra at $50\,\mu\mathrm{S}$ are shown where multiple particle tunneling processes play a major role. Andreev reflections cause additional peaks. The asymmetry of the intensity is still present though the weight is distributed differently due to resonant Andreev reflections through the YSR states. Reproduced from [1].

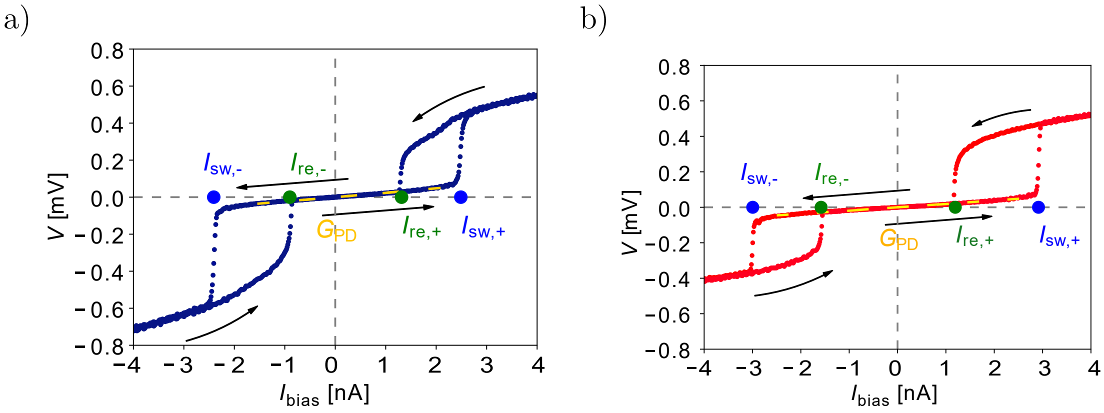

Figure 8.2: Exemplary V(I)Cs at $G_N = 50\,\mu S$ measured on a) Cr and b) Mn. Sweep directions are indicated by arrows and switching and retrapping events by blue and green symbols, respectively. The slope in the phase-diffusion regime is marked by a yellow dashed line. Reproduced from [1].

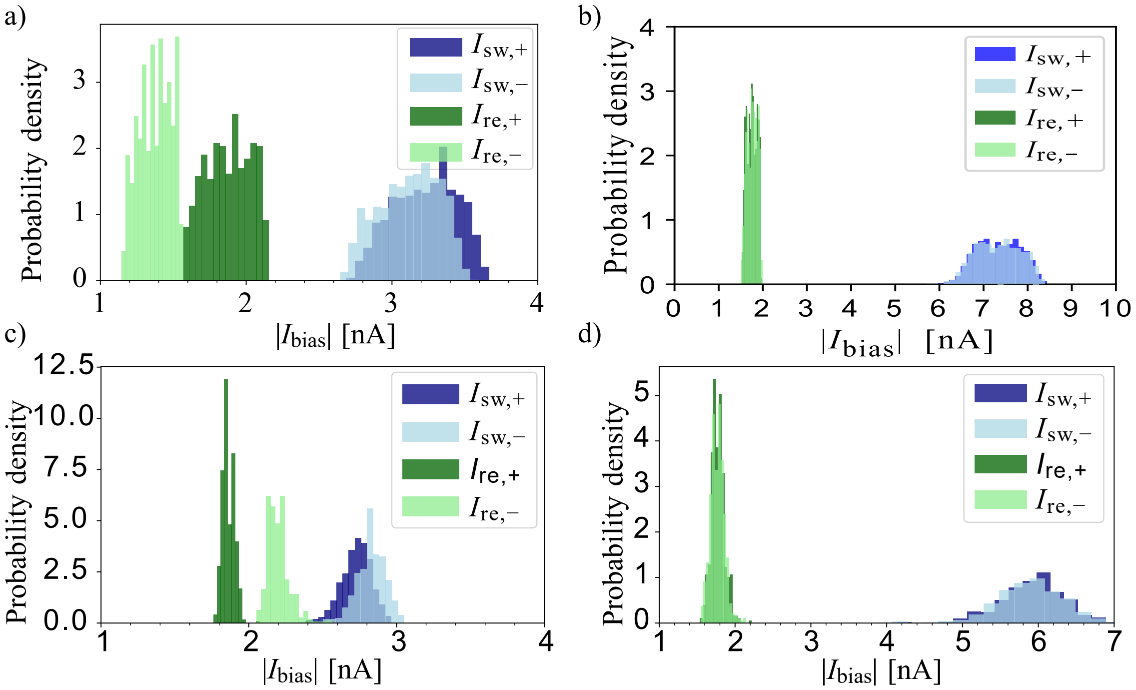

Figure 8.3: Exemplary histograms of switching and retrapping events at $G_N = 50\,\mu S$ measured on a) Cr (2000 sweeps) and c) Mn (500 sweeps) and their respective reference measurement on a pristine Pb junction shown in b) and d). For better visibility the absolute current values are shown and different colors to distinguish the positive bias values from the negative bias values. Asymmetric retrapping currents are observed. Reproduced from [1].

- Cooper-pair tunneling peak at $E = eV_b = 0$

Resonant Andreev reflections through YSR states cause a reversal of the intensities weights for the YSR state energies at positive and negative bias upon increasing the junction conductance. For more details see Peters *et al.* [52].

Here we focus on the Josephson peak at zero bias where Cooper pairs tunnel directly through the STM junction. Josephson spectroscopy was performed by applying a current bias and measuring the voltage across the junction at high normal state conductances as explained in chapter 5. Exemplary V(I)Cs are presented in figure 8.2 on Cr and Mn adatoms. The switching and retrapping events are indicated by blue and green symbols. The phase-diffusion conductance was derived from the slope at low currents indicated by the yellow dashed line.

As discussed previously, the switching and retrapping currents are statistical events and highly influenced by noise. For that reason, 500 sweeps were recorded on Mn and 2000 sweeps on the Cr adatom and their Pb reference in both sweep directions. To discuss the influence of the magnetic impurities on the Josephson junction's properties switching and retrapping currents were extracted from the single V(I)Cs and and the resulting histograms are shown in figure 8.3. For these histograms no creep correction was performed which leads to a broad distribution especially for the longer measurement of 2000 sweeps on Cr (for details see chapter 5.2).

In chapter 6 the characteristic features of the V(I)Cs especially regarding switching and retrapping events as well as phase diffusion were discussed for pristine Pb-Pb junctions. The switching currents in the presence of magnetic adatoms are reduced in comparison to the pristine junctions at the same normal state conductances as can be seen by comparing figure 8.3 a) to b) and c) to d). In addition to that, an asymmetry of switching and retrapping events with respect to the current sweep direction is observed in the presence of the magnetic adatoms. This non-reciprocity is particularly pronounced in the retrapping currents, though small differences are also observed in the average switching events. The origin of this non-reciprocity will be discussed in detail in the following sections. First we will focus on comparing the switching currents of the pristine junctions to the switching currents of junctions containing magnetic adatoms.

Due to piezoelectric creep the junction conductance changes over time as the statistics are recorded for several minutes broadening the histograms (see chapter 5.2). While we cannot determine the normal state conductance between measurement sweeps, we can measure the phase-diffusion conductance for each individual V(I)C. The phase-diffusion conductance is correlated to phase slips caused by the noise fluctuations. The strength of the phase-diffusion conductance depends on the amount of noise and the height of the potential maxima in the washboard potential picture. High noise levels and low potential maxima result in more phase slips and a reduction of the phase-diffusion conductance. The normal state conductance directly influences the Josephson energy and by that the height of the potential maxima. For that reason, the phase-diffusion conductance helps us keep track of changes in the normal state conductance over time.

The extracted switching currents are plotted over the phase-diffusion conductance in the presence of Mn and Cr adatoms and are compared to the reference measurements on the pristine Pb-Pb junctions in figure 8.4. A linear dependence between phase-diffusion conductance and switching currents is observed for the Josephson junctions. The phase-diffusion conductance G_{PD} and switching currents I_{sw} are reduced in the presence of magnetic atoms compared to the reference measurement on pristine Pb junctions at the same normal state junction conductance. The observed linear dependence in these curves indicates that all junctions switch at similar critical voltages for identical STM tips.

One of the reasons for the reduction of I_{sw} and G_{PD} consists in a local disturbance of the superconducting order parameter by the coupling of the magnetic moments to the superconducting condensate. Another reason for the enhanced phase diffusion may be an increase of the noise level induced by single particle scattering processes induced by the YSR states of the magnetic adatom. A higher noise level increases the probability for escape events to occur and also cause a reduction of the switching currents.

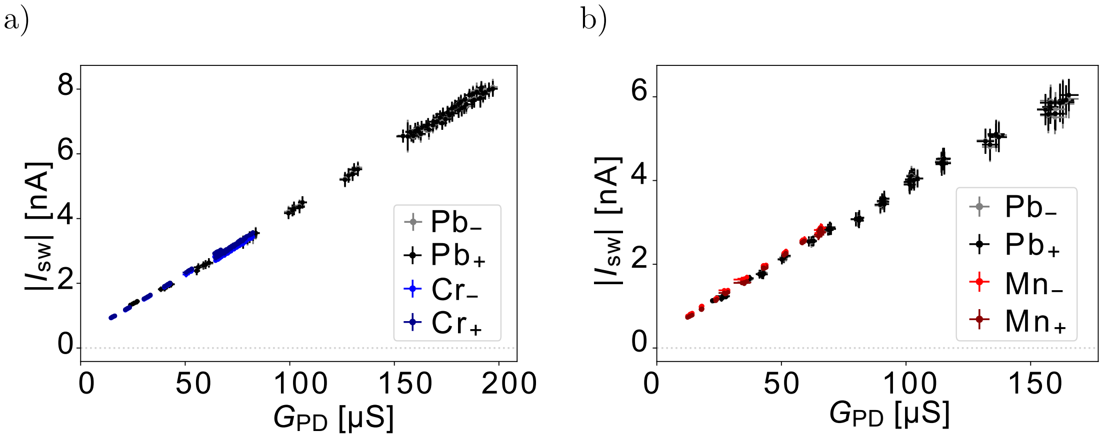

Figure 8.4: Switching currents I_{sw} for Josephson junctions on a) Cr and b) Mn atoms in dependence of the phase-diffusion conductance G_{PD} in comparison to pristine Pb-Pb junctions . Normal state conductances were set up between 25 µS and 50 µS. G_{PD} and I_{sw} are suppressed in the presence of magnetic adatoms. Reproduced from [1].

8.1 Josephson characteristics in proximity to Mn adatoms

As discussed in the previous section, magnetic adatoms in a Josephson junction reduce the switching currents of the V(I)Cs. In chapter 4.3 dI/dV maps of the Cr and Mn are shown. The lateral extension of the YSR states stems from the anisotropic crystal field of the Pb(111) surface that lifts the degeneracy of the unpaired d-orbital electrons of the magnetic atoms. As has been explained in chapter 4.3, the YSR states of Mn on Pb extent laterally, displaying the orbital configuration of the magnetic moments. Here, we investigate if the spatial extent of YSR states can be

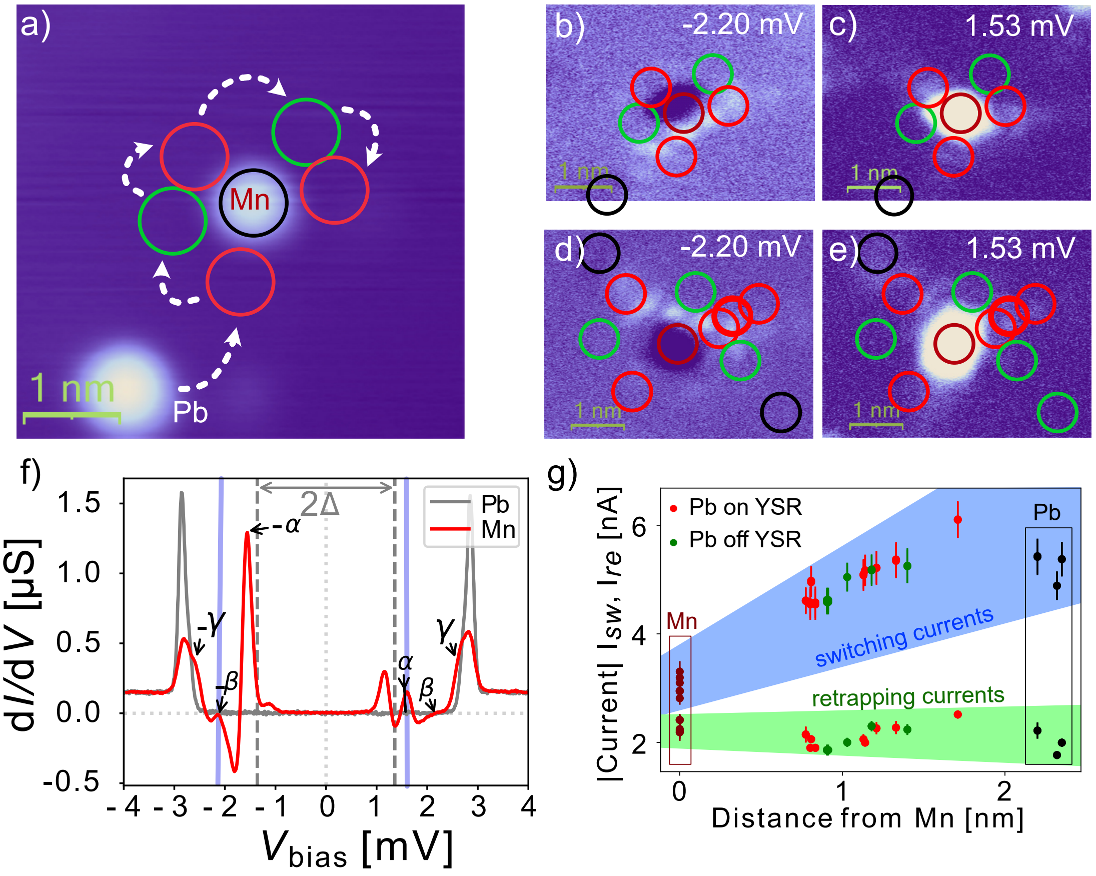

Figure 8.5: A Pb atom was manipulated to different locations around a Mn adatom as depicted in the topographic image in a). Two different Mn adatoms were investigated and the dI/dV maps are shown for each in figure b), c) and d), e) for two of the YSR peaks as indicated in the dI/dV spectrum in f). Circles indicate positions in which Josephson characteristics were recorded on the Pb atom. Colours distinguish if the atom was positioned on top of the YSR extension branch (red) or in-between branches (green). In g) the resulting switching and retrapping currents are plotted in dependence of the distance between Pb and Mn atom.

resolved in Josephson spectroscopy.

The presence of single magnetic atoms stabilizes the junctions at high conductances (see chapter 4.3). A single Pb atom was manipulated to different locations in close proximity to the Mn atom to measure the local variations of Josephson spectroscopy as indicated in figure 8.5 a). In figure 8.5 b) - e) the dI/dV maps for the YSR state energy are presented for two different Mn atoms on the Pb(111) surface. The YSR state energies were determined by the spectrum shown in 8.5 g). Circles of different colors indicate the location at which measurements were performed, red and green colors indicate if the location was considered to be on a YSR branch or in-between branches, respective.

The average switching and retrapping currents for the positions around the two presented atoms are summarized in figure 8.5 f). Within the resolution of our measurements there is no visible influence of the measurement being taken on a YSR branch or not. A slight reduction of the switching currents can be observed with decreasing distance between Pb and Mn atoms. From figure 8.5 f) the area of influence of the Mn atom on the Cooper-pair condensate of around 1 nm can be roughly estimated. This is in agreement with the Fermi wavelength that was was estimated from the periodicity of the scattering patterns observed for Mn on Pb(111) by M. Ruby et al. [40]. The resolution of the presented data is limited by the adsorption site of the Pb atoms next to the Mn adatom. A direct correlation between the single-particle scattering processes of electrons and holes to the reduction of switching currents of the Josephson junction cannot be made with a high degree of certainty.

8.2 Non-reciprocity of retrapping currents

The histograms in figure 8.3 show that the absolute values of the retrapping currents of junctions in the presence of magnetic atoms depend on the sweep direction of the current bias. The asymmetry is observed in exactly opposite directions for junctions containing Cr and Mn atoms. Furthermore, it is completely absent in Josephson junctions that feature a non-magnetic Pb adatom. In figure 8.6 the extracted switching and retrapping currents are shown in dependence of the phase-diffusion conductance. The switching currents do not show as significant an asymmetry as the retrapping currents.

The non-reciprocal behaviour of the junction's retrapping current is clearly shown in figure 8.7 were the difference of the retrapping currents of different sweep directions $\Delta I_{\mathrm{re}} = I_{\mathrm{re},+} - |I_{\mathrm{re},-}|$ is presented in dependence of G_{PD}. Figure 8.7 a) clearly shows that for Cr the retrapping currents on the positive bias side are larger while for the Mn atom the retrapping current on the negative bias side has the larger value. In comparison, the reference measurements on the pristine Pb junction do not show any asymmetry at all.

The asymmetric behaviour of retrapping currents has been observed in several ex-

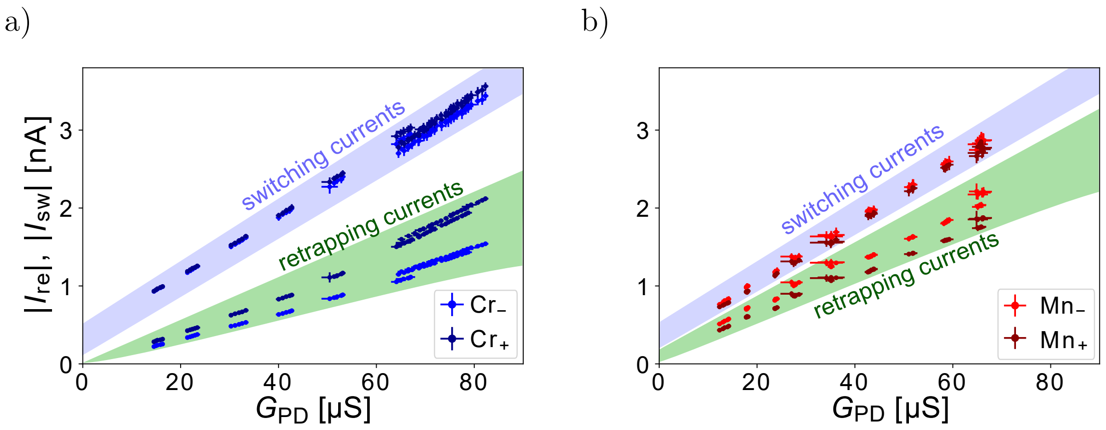

Figure 8.6: Switching and retrapping events in the presence of magnetic adatoms. In a) and b) switching and retrapping currents for Cr a) and Mn b) are presented in dependence of G_{PD}. Each point represents the average over 100 sweeps, the values change systematically over time due to piezoelectric creep. In both cases a clear asymmetry of the retrapping currents is visible. Reproduced from [1].

periments using different tip and sample preparations. The results for these measurements are summarized in figure 8.7 c) and d) for Cr and Mn, respectively. The same trends are observed for all of these experiments while the reference measurements on the pristine junctions do not show any asymmetry. Quantitatively the exact values of retrapping and switching currents depend on the noise level within the junction which may change between preparations. Some of the data with less pronounced asymmetries can be attributed to a change of the adsorption site of the magnetic atom by the forces acting between tip and sample.

The retrapping events mark the transition from the resistive to the predominantly trapped state of the junction. In the washboard potential picture the phase particle in the running state is recaptured in a minimum for a specific tilt of the potential landscape. The damping of the particle particle is determined by the resistance of the junction in the running state. The tilt of the washboard potential for which the particle is retrapped strongly depends on the inertia of the phase particle and its damping just before it is retrapped. The inertia is determined by the damping properties of the junction. In figure 8.8 the effect of damping on the junction is shown schematically in the washboard potential picture. The shape of the gray spikes indicate the asymmetric damping properties when the applied current tilts the potential in opposite directions.

To explain this difference in damping the YSR states that are induced by the magnetic adatoms need to be considered in detail. The damping of the Josephson junction is equivalent to the conductance of the junction in its resistive state. As discussed in chapter 2.3 and shown in figure 8.1 the dI/dV spectra become highly asymmetric with respect to their intensity in the presence of YSR states. Potential

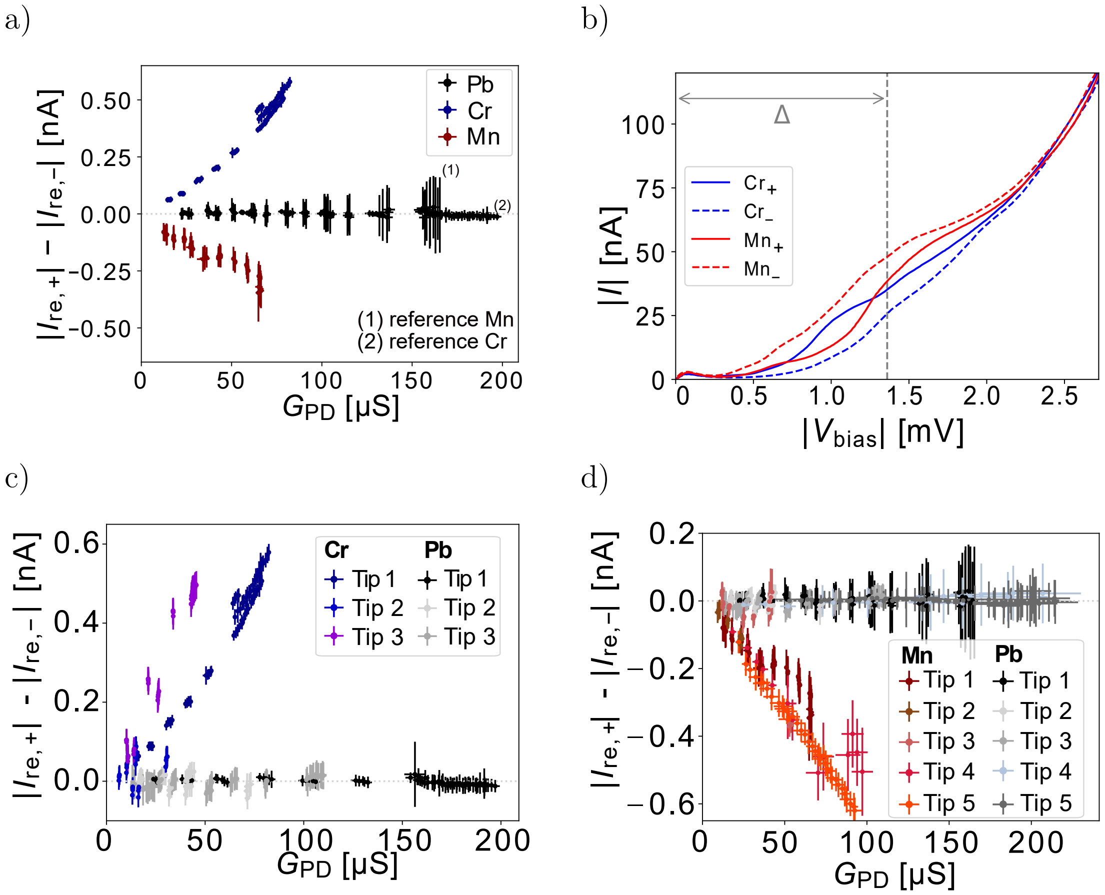

Figure 8.7: Non-reciprocity in the presence of Mn and Cr adatoms. In a) the asymmetry of I_{re} for Cr and Mn in comparison with the reference Pb-Pb junction is shown. The asymmetries are established in opposite directions for Cr and Mn and are absence in Pb. b) shows the I(V)Cs on a larger scale measured in voltage bias. An asymmetry of the measured currents on the positive and negative bias sides are observed. The non-reciprocity of the retrapping currents is observed in several data sets with STM tips from different preparations as shown in c) and d) for Cr and Mn, respectively. Though the quantitative value is affect by noise and varies between measurements, the diode effect is observed regardless of the specific setup. Slight variations may occur if the adsorption site of the atom was not sufficiently stable. Reproduced from [1].

scattering in the presence of the magnetic adatoms results in different tunneling probabilities for electrons and holes into the YSR states. This asymmetry is particularly strong for the lowest lying energy state in both cases of Cr and Mn adatoms (figures 8.1 a) and c)). The intensity weights are higher for opposite polarities of the applied voltage for the two types of atoms. For Cr the peak on the positive side is much larger than on the negative side while for Mn the probability to tunnel into the YSR state on the negative is much higher. As we approach the magnetic adatoms the intensity weights are inverted due to resonant processes through the YSR states. At high normal state conductances the quasiparticle current within the superconducting gap of the junction is large due to the occuance of Andreev reflections as described in the beginning of this chapter. As some of these tunneling processes are conveyed through the YSR states the electron-hole asymmetry translates to small energies close to the Josephson peak. On the Cr adatom (figure 8.1 b)) that results in a larger spectral weight for small energies on the positive bias side compared to the negative bias side while the opposite weight distribution is observed for the Mn adatom (figure 8.1 d)).

To emphasize the effect of electron-hole asymmetry the absolute values of the I(V)Cs for both atom species are shown in figure 8.7 b). The absolute values of the measured currents on the positive side are much larger than on the negative side for Cr and the opposite is true for the Mn adatom. Comparing these results with the asymmetries observed for the retrapping currents in figure 8.7 a) shows a relation of the asymmetric conductance through the YSR states due to electron-hole asymmetry to the damping properties of the Josephson junction.

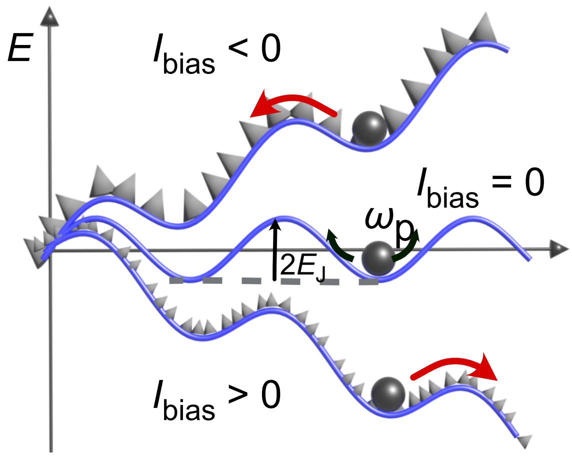

Figure 8.8: Schematic representation of the washboard potential for positive and negative bias values with different damping properties causing the nonreciprocity of the retrapping currents. Reproduced from [1].

8.3 Non-reciprocity of switching currents

In the beginning of this chapter it was established that the switching currents as well as the conductance in the predominately trapped state decrease in the presence of magnetic atoms. In figure 8.4 it was observed that the junctions switch at the same voltage as the pristine Pb junction. Additionally, a slight asymmetry for switching events at positive and negative applied currents is observed for Cr and Mn adatoms which is not present for pristine Pb-Pb junctions (figure 8.3). Following the previous argumentation, the asymmetry that we observe in the switching currents originates from the same effect as the asymmetry in the retrapping currents. In the phase-diffusion regime the phase particle constantly switches between the running and trapped state. As previously discussed, the voltage in the resistive state differs for positive and negative bias values, due to the electron-hole asymmetry induced by the magnetic adatoms. The voltage measured in the phase-diffusion regime is averaged over the time the particle spends in the running and the static phase. In the presence of a magnetic adatoms, the particle escapes to different resistive conditions in the running phase on either bias polarity. This results in different voltages that are measured for the same bias value on the positive and negative side which affect the damping of the phase particle in the washboard potential. Due to the asymmetric quasiparticle conductance the switching events occur at different current values.

The described asymmetry of I_{sw} is not resolved in every junction in the presence of magnetic atoms. A reason for that might be a change in the escape mechanism depending on the noise level in the junction. Strong noise fluctuations may give the escaping particle more excess energy and cause the particle to escape immediately. The effects caused by the damping conditions might not be resolved next to these spontaneously occurring fluctuations.

8.4 Calculation of V(I)Cs with asymmetric damping properties

Theoretical calculations were performed by L. Melischek and J. F. Steiner in the group of Prof. F. von Oppen at Freie Universität Berlin. They reproduced the non-reciprocity observed in experiments by using asymmetric quasiparticle currents but assuming a completely symmetric CPR with $I_S(\phi) = I_C \sin(\phi)$. The results described here are published in [1] and a more elaborated theoretical study of diode-like behaviour in Josephson junctions and their symmetry requirements can be found in [105].

The equation describing the Josephson junction derived from the RCSJ model contains a fluctuation term that in our experiment is dominated by Johnson-Nyquist-noise δI_F. Including this fluctuation term equation 3.13 becomes a stochastic differential equation (Langevin equation) with respect to the phase of the Josephson

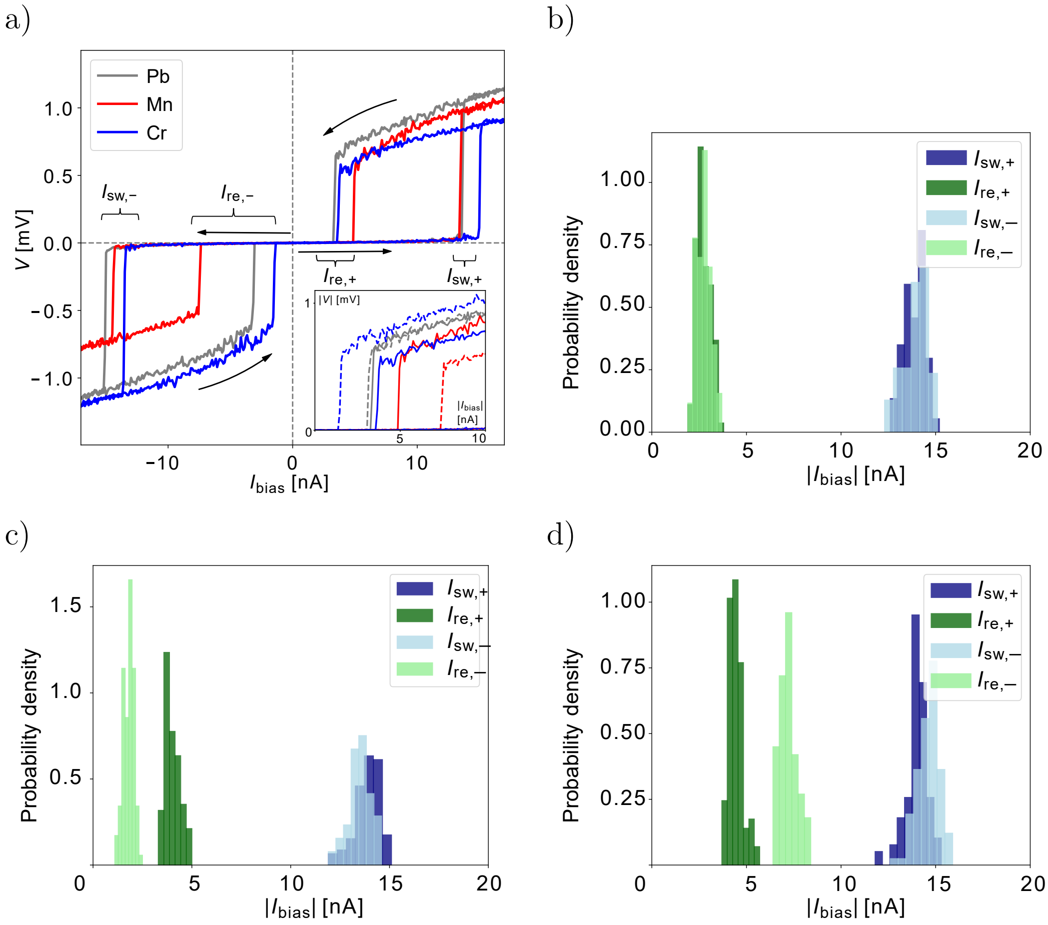

Figure 8.9: Simulated Josephson characteristics for Pb, Cr and Mn adatoms. In a) V(I)Cs were simulated by theoretical calculations including an adjusted RCSJ model to capture the influence on the damping of the junction by the asymmetric YSR intensity. Histograms of the statistics of the simulated V(I)Cs are shown for b) Pb, c) Cr and d) Mn junctions. The simulated histograms fit very well to the experimentally observed statistics and reproduce the asymmetry of the retrapping currents. Reproduced from [1].

junction which are solved by Monte Carlo integration.

In chapter 3.1 frequency-dependent damping was introduced by the addition of an R_sC_b-component to the RCSJ model (figure 3.5 b)). Taking this R_sC_b-component into account, the total dissipative current through the junction I_d consist of two parts:

$$I_d(V) = I_R + I_{\text{freq}}. \tag{8.1}$$

$I_R = V/R_N$ corresponds to the quasiparticle current and $I_{\text{freq}} = (V - V_s)/R_s$ is the frequency-dependent current through the resistor of the R_sC_b-component. V is the measured voltage drop across the junction and V_s the voltage drop at the capacitor C_b. The Johnson-Nyquist noise in the junction is determined by the noise of the two resistors R_N and R_s (δI_R and δI_{R_s}).

The quasiparticle current I_R is extracted from the experimental data. A phenomenological approach was chosen to separate the contribution from the Josephson current

$$I_J(V) = A\frac{V\delta V}{V^2 + \delta V^2} + B\frac{V^3\delta V}{(V^2 + \delta V^2)^2} \tag{8.2}$$

and the quasiparticle current

$$I_R(V) = CV + DV^2 + EV^3. \tag{8.3}$$

Determining the fit parameters (A, B, C, D, E) allows for isolating the Josephson contribution and removing it from the experimental data obtaining the bare quasiparticle current [106].

With these considerations single traces of V(I)Cs can be simulated as shown in figure 8.9 a). Simulating a few hundreds of these curves captures the statistical nature of the involved processes and results in the histograms for switching and retrapping events in figure 8.9 b) - d). By extracting the quasiparticle currents from the experiments information on the junction properties enter the simulation. In particular, the asymmetric conductance measured in the normal state of the junction in the presence of a magnetic adatom directly reproduces the asymmetric retrapping behaviour. This can be observed by comparing the histograms of the simulated V(I)Cs for Pb, Cr and Mn in figure 8.9 b), c) and d) to the histograms measured in the experiments (figure 8.3). A qualitative agreement between the simulations and experiments is observed. The non-reciprocity of the retrapping currents for the Josephson junctions containing Mn and Cr is well reproduced. The direction of the non-reciprocities in the Josephson junctions depends on the asymmetry of the conductance in the resistive state. No asymmetries are observed for the non-magnetic Pb atom in the junction.

A small asymmetry of the switching currents is observed as well. The asymmetry of the switching current is determined by noise fluctuations at the normal state resistor δI_R which influences the statistics of the escape process. The asymmetric normal state conductance causes asymmetric fluctuations as well.

A symmetric CPR enters the calculations and the observed asymmetry originates purely from the in-gap quasiparticle conductance. The asymmetry of the conductance in the presence of the magnetic adatoms is caused by electron-hole asymmetry. As explained in chapter 2.3 the electron-hole asymmetry is an effect related to the potential scattering of the adatom and results in different tunneling probabilities into YSR states with electrons or holes. All details and further information on the calculations and theoretical considerations can be found in [105].

8.5 The Josephson diode effect

In the presented experiments magnetic impurities on a superconducting surface break inversion symmetry due to the electron-hole asymmetry of the YSR states so that $I(V) \neq I(-V)$. This causes non-reciprocities mainly in the retrapping currents with a small asymmetry also being observed in the switching currents of the Josephson junctions formed on the atoms. This diode-like behaviour however has different origins than the Josephson diodes discussed for example in [98], [20] and [15]. For more details on the theoretical background on the Josephson diode effect see chapter 3.4. The Josephson diodes with asymmetric critical currents require an asymmetric CPR , as discussed in most recent literature. In superconductors with strong spin-orbit coupling helical superconductivity is observed when time-reversal symmetry is broken. Cooper pairs in these helical systems have a finite momentum in the absence of an external bias which causes the non-reciprocity in the experimental findings. In Josephson junctions an asymmetric CPR causes the junction's critical currents to become dependent on the biasing direction. Time reversal symmetry breaking is usually achieved by an external magnetic field and is essential for helical superconductivity to be observed.

In the presented experiments no external magnetic field is applied. The magnetic moment of the atoms do not have a preferential direction and are therefore not suited to break time-reversal symmetry and do not cause helical superconductivity. In our case the processes are governed by noise and non-reciprocities can be explained by differences in the damping properties alone. Asymmetries in the quasiparticle conductance arise due to the electron-hole asymmetry of the induced YSR states and influence the damping properties of the Josephson junction. The difference of the damping is mainly observed in the retrapping current of the V(I)Cs as opposed to observing non-reciprocities in the switching currents.

We show that by adding single magnetic atoms we can influence the damping properties of the Josephson junctions (as schematically shown in figure 8.8). The electron-hole asymmetry induced by the adatoms breaks inversion symmetry without breaking time-reversal symmetry. This asymmetry influences the damping of the junction in the running-state and causes the observed non-reciprocities of the retrapping currents.

CHAPTER 9

SUMMARY, CONCLUSION AND OUTLOOK

Current-biased STM Josephson junctions enable the investigation of the junction's phase dynamics on the atomic scale. In STM Josephson junctions the normal state conductance becomes an easily tunable parameter and the exact atomic composition of the surface on which the junction is formed is fully controlled. However, the exact physical form of the tip remains elusive so that the junction capacitance is not well defined and may change between experiments. Single atoms on the Pb(111) surface were used to stabilize junctions of conductances up to 60 µS. A statistical analysis was done by recording a few hundred sweeps for each bias direction for each junction.

9.1 Characterization of STM Josephson junctions

The STM Josephson junctions investigated in this thesis couple to the environment via a frequency-dependent impedance. The frequency-dependent impedance causes the junction to weakly interact with the environment at low frequencies (underdamped junction) while strong dissipation is observed at higher frequencies (overdamped junction).

In the current-biased V(I)Cs phase diffusion is observed in the Cooper-pair tunneling regime where the plasma frequency dominates the phase dynamics and the junction is in the overdamped state. The switching currents extracted from the V(I)Cs are more than an order of magnitude smaller than the expected value for the full superconducting gap of a Pb-Pb Josephson junction. The junction switches prematurely due to noise fluctuations which are also responsible for the observed phase diffusion in the Cooper-pair tunneling regime. Retrapping events, i.e. the opposite transition from the resistive state to the Cooper-pair tunneling regime occurs at much lower current values compared to the switching current. This hysteresis is clearly related to underdamped behaviour.

Voltage-biased Josephson junctions also allow Cooper-pair tunneling by exchanging energy with the electromagnetic environment. The interaction with the environment can be described by P(E)-theory and takes a frequency dependent impedance into account for calculating the probability functions that determine the likelihood of tunneling for each individual Cooper pair.

We observe that while both biasing methods exchange energy with the environment, the coupling to the environment is not always the same. For current-biased Josephson junctions the impedance is determined by an RC-component in parallel to the junction. The impedance of the voltage-biased junction is dominated by the series resistance.

9.2 HF irradiation and Cooper-pair tunneling

To further investigate the interaction of the Josephson junction with the environment and particularly the influence on the phase dynamics, an HF-field of ω_r =40 GHz was applied via an antenna located near the junction. As previously discussed the STM Josephson junctions strongly interact with the environment. In voltage-biased Josephson junction photon-assisted tunneling is known to occur for incoherently tunnelling Cooper pairs. The tunneling Cooper pairs absorb an integer number of photons n at energies of $2eV = n\hbar\omega_r$.

In current-biased Josephson junctions phase coherence may result in the coherent absorption of energy from the HF-field. Coherent excitations occur when the Josephson frequency due to the motion of the phase particle in the RCSJ washboard potential matches the frequency of the HF radiation. Resonances are also expected at voltage values of $V_{n,dc} = n\frac{\hbar\omega_r}{2e}$.

Resonances are observed in the presented experiments at the expected voltage values. The transition between resonances in the current-biased junctions depend on the direction of the applied current. This hysteresis implies that the inertia of the phase particle in the washboard potential influences the transition between resonances which corresponds to phase coherence in the junction. However, the voltage resonances are not flat but show a finite slope which indicates the presence of phase diffusion and accordingly incoherent processes to be relevant.

Comparing the voltage- and current-biased measurements showed that the HF irradiation affects the transport through the junction quite similarly. The voltage resonances show small variations of the slope for the two biasing methods. This variation is probably related to the coupling to the environment via different impedances as discussed in the previous section. The largest difference consists in the hysteresis which is observed only in the current-biased junction but not in the voltage-biased measurements. Hysteresis is a feature that is expected for slightly underdamped junctions for which the phase particle's inertia determines the transition between resonant voltage states. However since incoherent processes are observed at the same time, Shapiro steps cannot be clearly identified in the current-biased STM Josephson junctions.

9.3 Magnetic adatoms in Josephson junctions

The influence of single magnetic atoms on the properties of current-biased Josephson junctions was studied. Switching currents as well the conductance in the Cooper-pair tunneling regime are reduced in comparison to the pristine Pb-Pb junctions. This reduction can be correlated either to an increase of noise fluctuations in the junction increasing the escape rates or to a reduction of the Josephson Energy due to coupling of the impurity to the Cooper-pair condensate. Additionally, we observed a non-reciprocity which was most pronounced in the measured retrapping currents. This asymmetry with respect to the biasing direction appeared only in the presence of the magnetic atoms while no asymmetry is observed in the pristine Pb-Pb junctions. According to the RCSJ model, the retrapping event marks the transition from the running state of the phase particle within the washboard potential picture to the trapped state.

By introducing magnetic adatoms to the junction YSR states are induced via the coupling of the spin of the unpaired electrons to the superconducting condensate. The YSR states can be accessed by electrons and holes and appear at positive and negative energies in the tunneling spectra. Potential scattering occurs as the local electromagnetic environment at the sample surface is disturbed by the magnetic adatom. Potential scattering influences the tunneling rates when accessed by an electron or hole. This electron-hole asymmetry introduces different intensity weights for YSR states at positive and negative energies. At high junction conductances additional resonant tunneling processes through the YSR states influence the in-gap conductance of the tunnel junction significantly. Specifically, it in-gap conductance of the junction close to zero energy becomes asymmetric due to the asymmetric intensities of the YSR resonances.

Josephson spectroscopy was performed on magnetic Cr and Mn adatoms to investigate the influence the YSR states. In collaboration with the theory group of Felix von Oppen at Freie Universität Berlin the electron-hole asymmetry of the YSR states was correlated to the damping properties of the Josephson junction. They solved the Langevin equation from the adapted RCSJ model by Monte-Carlo simulations. Assuming a symmetric CPR and modelling the resistive quasiparticle current from the experiments it was possible to reproduce the non-reciprocities observed in the experiments.

Magnetic atoms influence the presented Josephson junctions by interacting with the Cooper-pair condensate and changing the junction's damping properties. In the absence of time-reversal symmetry breaking there is no reason to assume a fundamentally change the CPR of the junction causing asymmetric critical currents. The magnetic moments of the adatoms do not have a preferential direction so that they do not break time-reversal symmetry.

9.4 Conclusion

In this thesis STM Josephson spectroscopy was performed on single-atom adsorbates on a Pb(111) surface. The phase dynamics of STM Josephson junctions was found to be strongly influenced by noise fluctuations. Noise is introduced to the junction by interaction with electromagnetic environment via a frequency-dependent impedance. It was found that a current-biased STM Josephson junction couples to the environment by an impedance that is different from the impedance of the voltage-biased junction.

The coherence of the Cooper-pair tunneling process was further investigated by applying external HF irradiation. Hysteretic steps are observed in the current-biased V(I)Cs. This hysteresis indicates the presence of phase coherence in the current-biased Josephson junctions. The steps could not be identified unambiguously as coherent Shapiro steps due to the evidence of incoherent processes such as phase diffusion.

Performing Josephson spectroscopy on single magnetic adatoms revealed a reduction of the switching currents compared to the pristine junctions. A reduction of the Josephson energy E_J or an increase of the noise fluctuations due to single-particle scattering processes were identified as possible causes. A non-reciprocity was observed with respect to the sweep direction of the retrapping currents in the presence of magnetic adatoms. It was found that the conductance in the resistive state of the junction strongly influences the damping properties of the Josephson junction. The damping of the Josephson junction becomes asymmetric in the presence of magnetic adatoms due to the electron-hole asymmetry induced by the YSR states. This results in the observed Josephson diode effect with respect to the retrapping events in the Josephson junctions.

STM Josephson spectroscopy provides the possibility to fine-tune the non-reciprocal transport through the junction by the manipulation of magnetic adsorbates on superconducting surfaces and thereby the induced YSR states.

9.5 Outlook

One of the goals for future possible projects could be to deepen the understanding of the relevant timescales of the Josephson junctions and investigate the influence of noise fluctuations in more detail. Another interesting avenue consists in further investigating the Josephson diode effect and looking into the possibility of asymmetric CPRs in the presence of magnetic structures.

For a deeper understanding of the phase dynamics in STM Josephson junctions, the timescales of the phase coherence in the junction should be further investigated. Systematically changing the speed of bias sweeps will provide informations on the escape rates of the phase particle from the washboard potential. Preliminary results showed an influence of the current sweep rate on the average switching and retrapping currents. For a measurable effect the sweep rate had to be varied by at least one order of magnitude. It was found that sweeping the bias slowly increases the probability of the phase particle to gain sufficient energy to permanently escape from the potential for each applied current value. For that reason a decrease of switching currents is expected the slower the current is changed over time. The effects on the phase-diffusion conductance are not as intuitive. The ratio of the time the phase particle spends in the running state to the time it stays in the trapped state should be constant over sufficiently long time averages. These effects will be highly influenced by external noise sources and strongly impacted by the exact form of the tip apex. For that reason good statistics are necessary to draw conclusions from the suggested experiments. Presumably the current-biased measurements might converge with the voltage-biased measurements for very slow sweep rate.

In this work HF irradiation was applied to the pristine Pb-Pb Josephson junctions. These measurements might hold further information on the coherence of the tunneling processes in the junction when combined with the suggested sweep rate dependence. Applying different irradiation frequencies in combination with changing the speed of the current bias sweep may influence the dynamics of the junction. Additionally, the influence of the HF irradiation on the Josephson junctions that contain magnetic adatoms can be investigated. Magnetic adatoms locally disturb the Cooper-pair condensate and introduce noise by the induced YSR states. Preliminary measurements of Josephson junctions containing Mn atoms have been performed and are shown in figure 9.1. The additional tunneling channels that are mediated by the YSR states result in a higher overlap of the splitting peaks in the measured dI/dV maps (figure 9.1 a) and b)). For the current-biased measurements in figure 9.1 c) - f) the appearance of a first HF-induced step can be observed at zero bias. However, since the switching and retrapping events occur at much smaller values for the Josephson junctions in the presence of magnetic adatoms, subsequent steps are hard to resolve.

The noise in the Josephson junction should be further specified as well. In STM experiments shot noise experiments have been performed on similar setups [107, 108]. Further specifying the amount and type of noise in the Josephson junction may provide more insights into the physics behind the phase dynamics of the junction.

One of the main advantages of using Josephson spectroscopy in an STM experiment is that it provides control over the junction on the atomic scale. It may be possible to build magnetic structures that fix the magnetic moment of the atoms providing a ferromagnetic or anti-ferromagnetic behaviour. These structures might break time-reversal symmetry and change the CPR of a Josephson junction fundamentally. As of now the Josephson experiments performed in STM are dominated by external noise and it is unlikely that non-reciprocity of the critical currents of the junctions would be resolved in the experiment. By further improving the noise ratio of the junction for instance by cooling the bias line resistor to temperatures close to the junction temperature and improving the noise in the wiring leading to the junc-

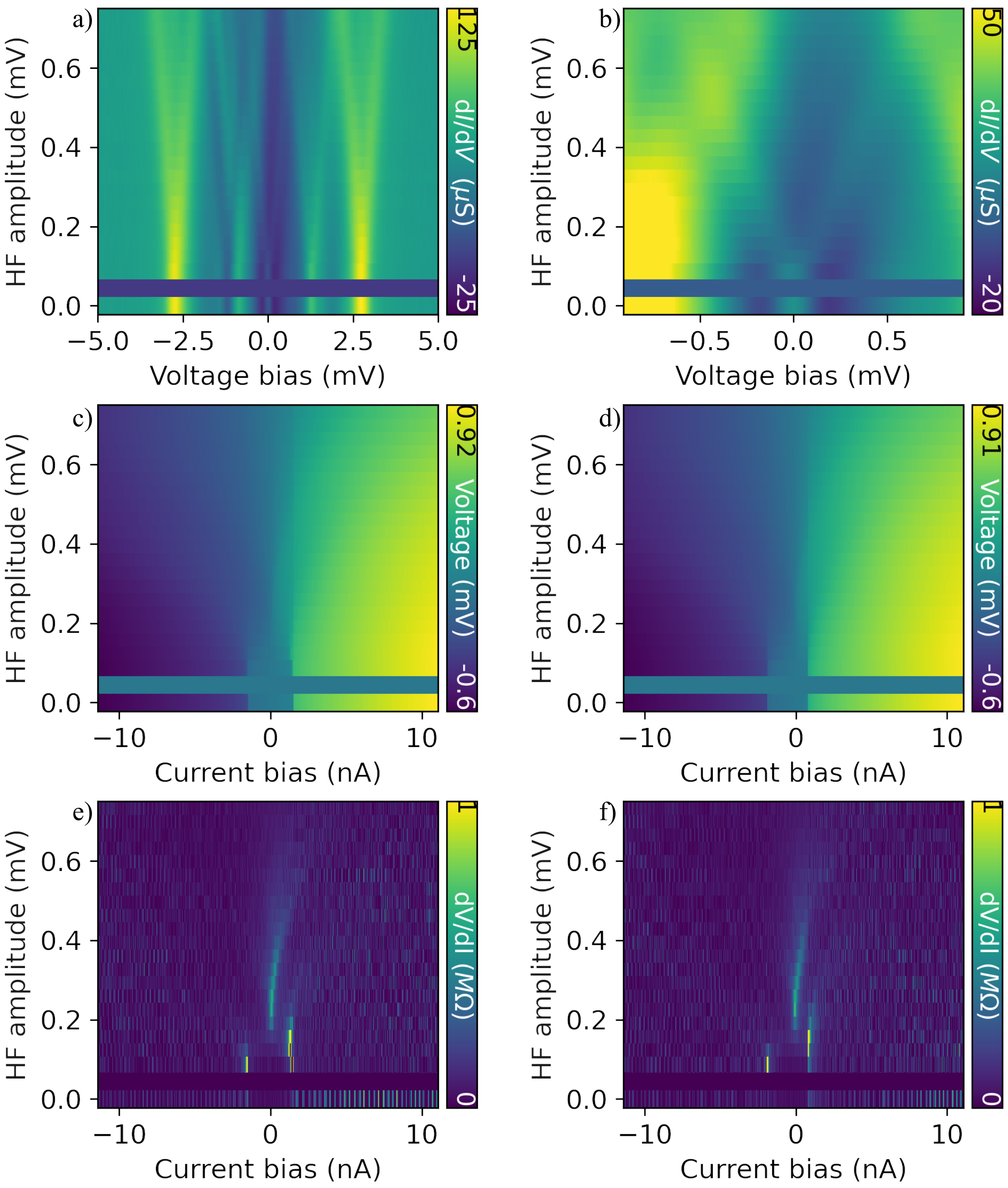

Figure 9.1: Josephson junction at a normal state conductance of 50 µS on a Mn adatom in the presence of HF irradiation. a) shows the splitting of the voltage-biased dI/dV spectrum. b) shows a zoom-in on the Josephson peak. Due to the overlap of the additional conductance peaks caused by the YSR states the splitting of the Josephson peak is hardly resolved. c) and d) show the current-biased junction for the two sweep directions. Compared to the pristine Pb-Pb junction switching and retrapping currents are reduced. e) and f) show the derivative of current-biased spectra.

tion it might be possible to test for asymmetries in the CPRs of STM Josephson junctions.

Appendix

APPENDIX A

CONCERNING THE AC JOSEPHSON EFFECT

The ac Josephson effect describes the ac modulation of the current in response to a a dc voltage drop across the junction. The ac Josephson effect can be explained in the washboard potential picture. In contrast to the main text where the voltage-biased junction dissipates energy to the environment and is treated by P(E)-theory the ac Josephson effect occurs in the absence of noise fluctuations. Biasing a junction with a voltage directly controls the velocity of the phase particle. For a constant velocity a force needs to counteract the energy dissipation of the phase particle due to the damping properties of the junction. That force corresponds to a tilt of the potential which is equivalent to the measured current. A constant dc voltage V_b simplifies the RCSJ equation since $V_b \propto \frac{d\phi}{dt} = const \rightarrow \frac{d^2\phi}{dt^2} = 0$:

$$I(t) = I_C \sin(\phi(t)) + \frac{\hbar}{2e}\frac{1}{R}\frac{d\phi}{dt} = I_C \sin(\phi(t)) + \eta V_b = I_{ac} + I_{dc} \tag{A.1}$$

The current has a dc component I_{dc} which is modulated by the ac component I_{ac}. The dc component of the current corresponds to the average tilt of the washboard potential. In figure A.1 a) the equivalent tilt of the washboard potential is depicted for two different applied voltages. The average tilt of the potential compensates for losses due to the dissipation in the system. However, the particle experiences acceleration and deceleration within each period of the washboard potential. To keep the velocity constant within each period of the potential an additional modulation of the potential tilt is necessary. $I_{ac} = I_C \sin(\phi(t))$ decelerates the particle on the down-slope of the potential and accelerates it on the up-slope to keep the velocity constant with $\phi(t) = \omega_J t$. The relevant frequency for this motion is the Josephson frequency ω_J.

In figure A.1 b) the current modulations for different applied voltages are shown over time. The higher the dc voltage the higher also the average tilt of the washboard potential (I_{sc}) and the higher the frequency of the modulation. Additionally the height of the effective maxima decrease with increasing average tilt of the potential. Accordingly the modulation amplitude of the ac component of the measured current decreases with increasing voltage.

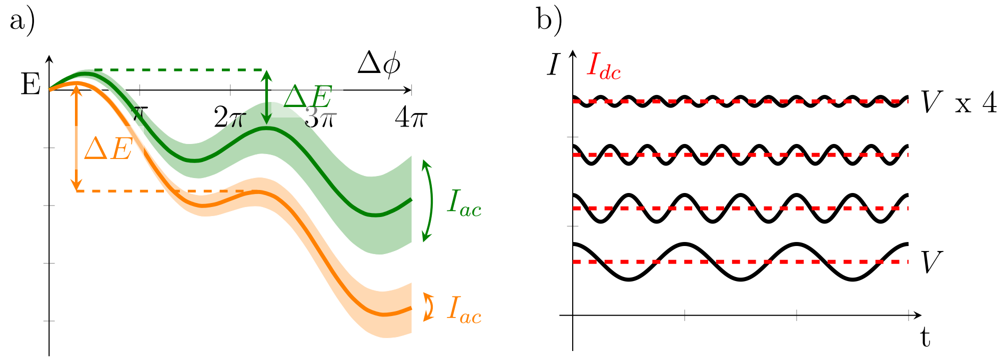

Figure A.1: The ac Josephson effect and the washboard potential picture. a) An applied voltage causes an ac modulation of the measured current. For an overdamped junction the washboard potential's average tilt compensates the junction's damping by ΔE. b) Current modulations for different applied voltages. The average tilt of the washboard potential is given by I_{dc}. The frequency of I_{ac} depends on the applied voltage ($\phi(t) = \omega_J t$) and it's amplitude on the effective height of the potential maxima.

APPENDIX B

CORRECTION OF V(I)CS FOR A FINITE VOLTAGE IN THE RUNNING STATE

In chapter 5.2 it was mentioned that the current-biased measurements of the V(I)Cs are not completely accurate as soon as the Josephson junction switches to the resistive state. In the resistive state a voltage drops across the junction which is not negligible compared to the bias line resistor of $R_{\mathrm{B}} = 1\ \mathrm{M\Omega}$. The applied current needs to be corrected by the measured voltage V_{measure} as follows:

$$I_{\mathrm{junction}} = I_{\mathrm{b}} - \frac{V_{\mathrm{measure}}}{R_{\mathrm{B}}} \tag{B.1}$$

Most prominently this effect changes the extracted retrapping currents for each single V(I)C.

In figure B.1 the histograms of data sets recorded on Josephson junctions containing a single Pb, Cr and Mn adatoms are shown. The extracted data for the uncorrected V(I)Cs are displayed in the left column while the histograms that result from the corrected V(I)Cs are shown in the right column. The extracted current values shift as expected when the correction is applied. However, the qualitative comparison between the data sets is consistent with the analysis and interpretation given in chapter 8. Note that fewer V(I)-curves enter the statistics of the corrected histograms due to the challenges with regarded to the now not completely monotonous behaviour of the V(I)Cs with the applied current I_{b} as pointed out in chapter 5.2.

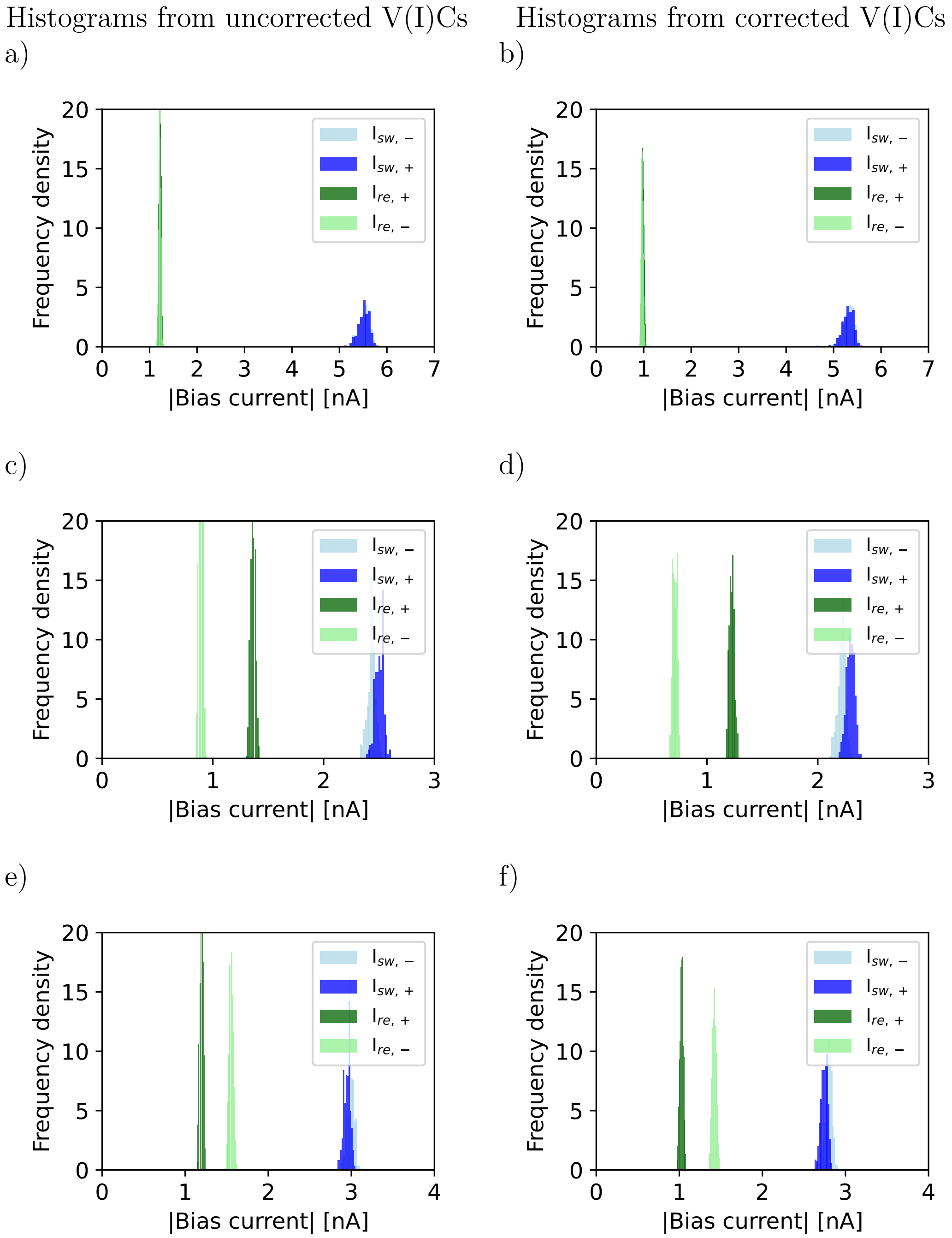

Figure B.1: Comparison of histograms from uncorrected and corrected V(I)Cs. The left column (a) Pb, c) Cr, e) Mn) show the histograms based on the uncorrected V(I)Cs for Pb, Cr and Mn adatoms respectively. the right column (b) Pb, d) Cr, f) Mn) shows the histograms after correcting for the finite voltage drop in the resistive state of the junction.

APPENDIX C

ADDTIONAL DATA WITH HF IRRADIATION

In chapter 7 the influence of an external HF irradiation on the current-biased Josephson junctions has been discussed in detail. As an example a junction on a Pb atom at a junction conductance of 60 µS was chosen with an irradiation frequency of 40 GHz.

More data has been recorded on junctions containing a Pb atom at 50 µS. The junctions were irradiated with different frequency and are presented in figure C.1 with 40 GHz, figure C.2 with 35 GHz and in figure C.3 with 30 GHz irradiation frequency. Both the voltage-biased and current-baised data is presented. Comparing the voltage-biased data sets for different applied frequencies shows a reduction of the spacing between peaks as expected. In the current-biased data the amount of hysteresis of the first step seems to reduce with decreases frequency. A more detailed analysis is necessary to investigate the influence of the irradiation frequency on the phase dynamics of the current-biased junctions.

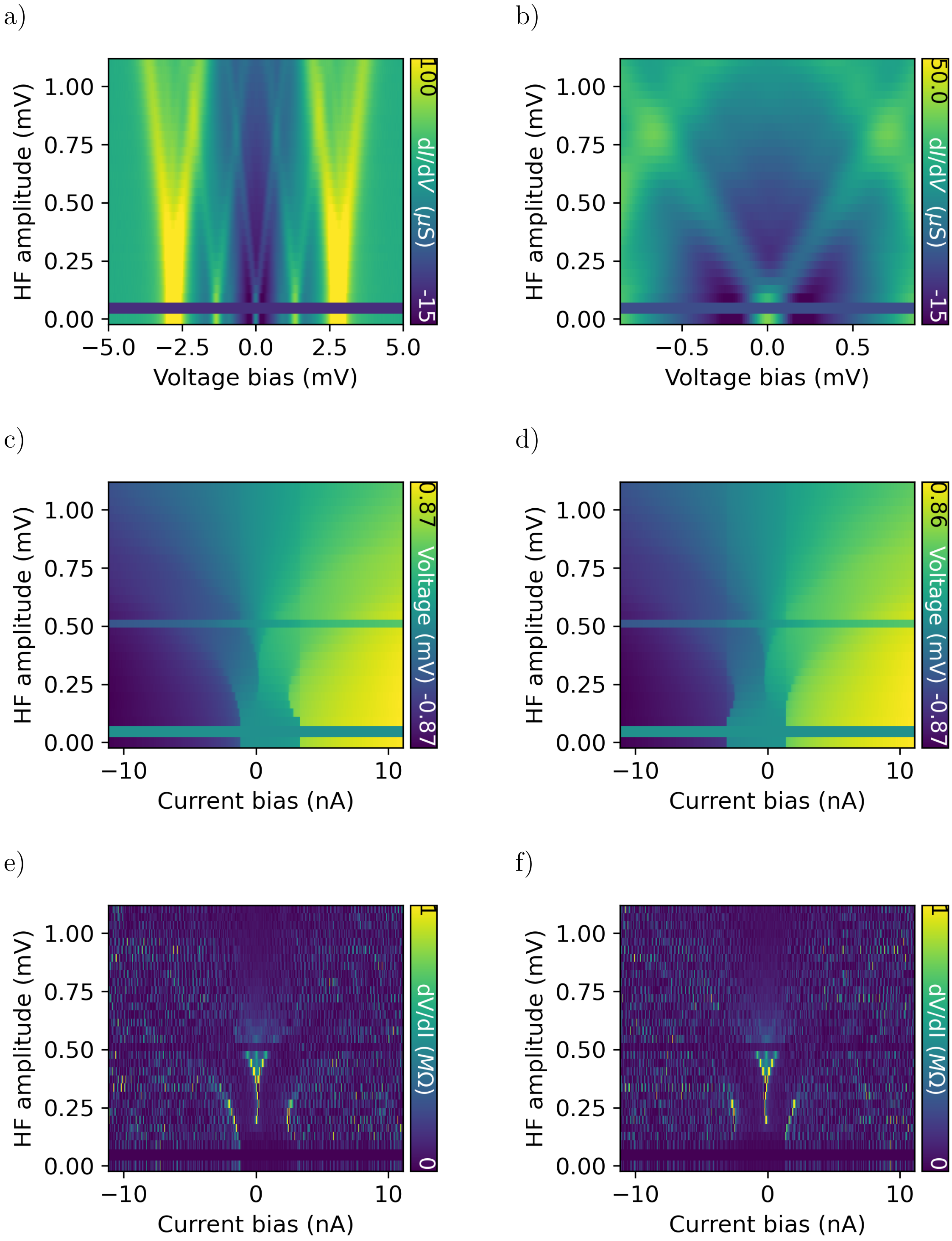

Figure C.1: 50 µS Josephson junction on a Pb adatom under 40 GHz HF irradiation. a) shows the voltage-biased dI/dV spectra (amplitude $V_{rms} = 20\,\mu\text{V}$) for an increasing HF amplitude. b) shows the zoom in on the Josephson peak. In c) and d) the current-biased V(I)Cs are displayed for both sweep directions. The derivative of these data sets is plotted in e) and f).

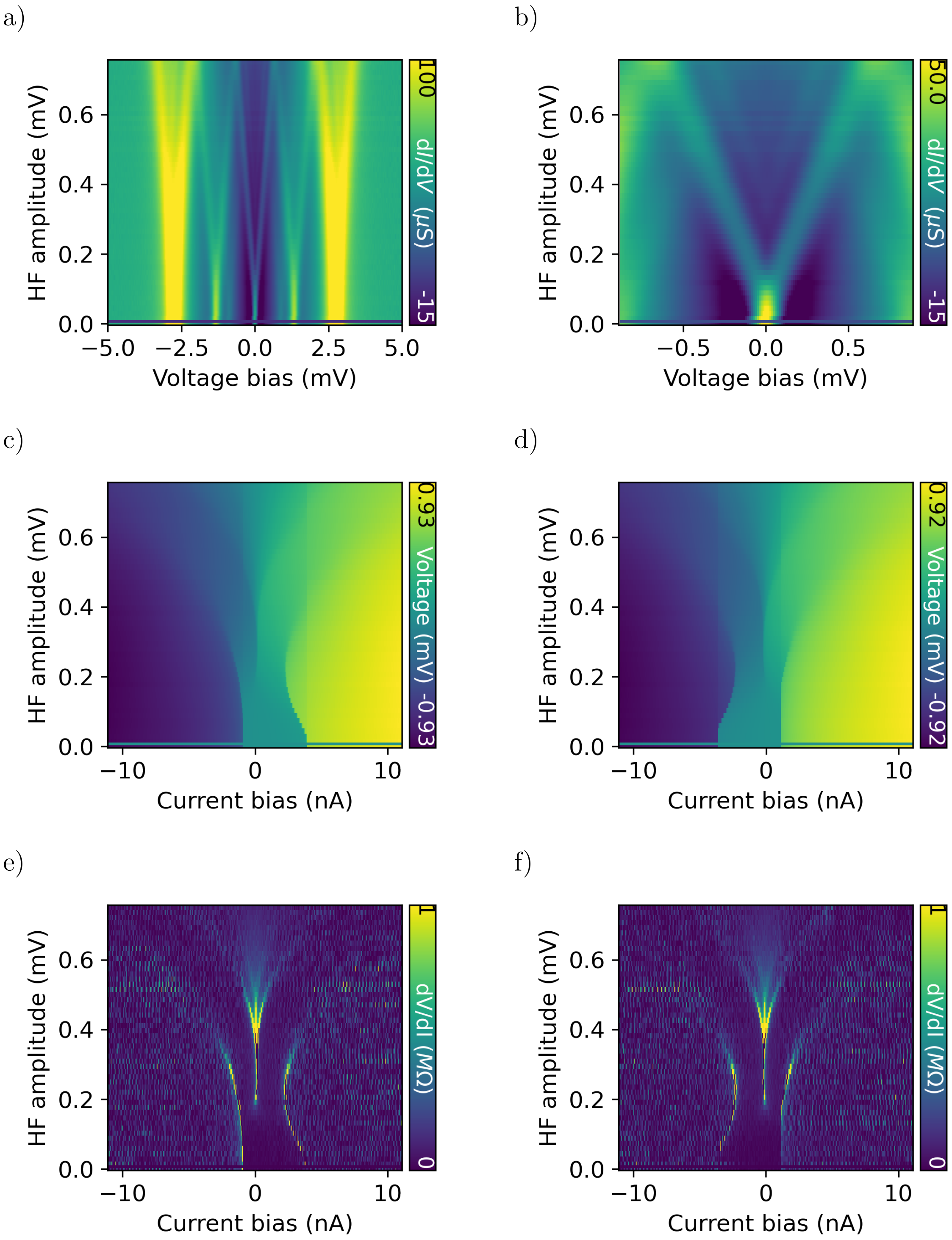

Figure C.2: 50 µS Josephson junction on a Pb adatom under 35 GHz HF irradiation. a) shows the voltage-biased dI/dV spectra (amplitude $V_{rms} = 20\,\mu\text{V}$) for an increasing HF amplitude. b) shows the zoom in on the Josephson peak. In c) and d) the current-biased V(I)Cs are displayed for both sweep directions. The derivative of these data sets is plotted in e) and f).

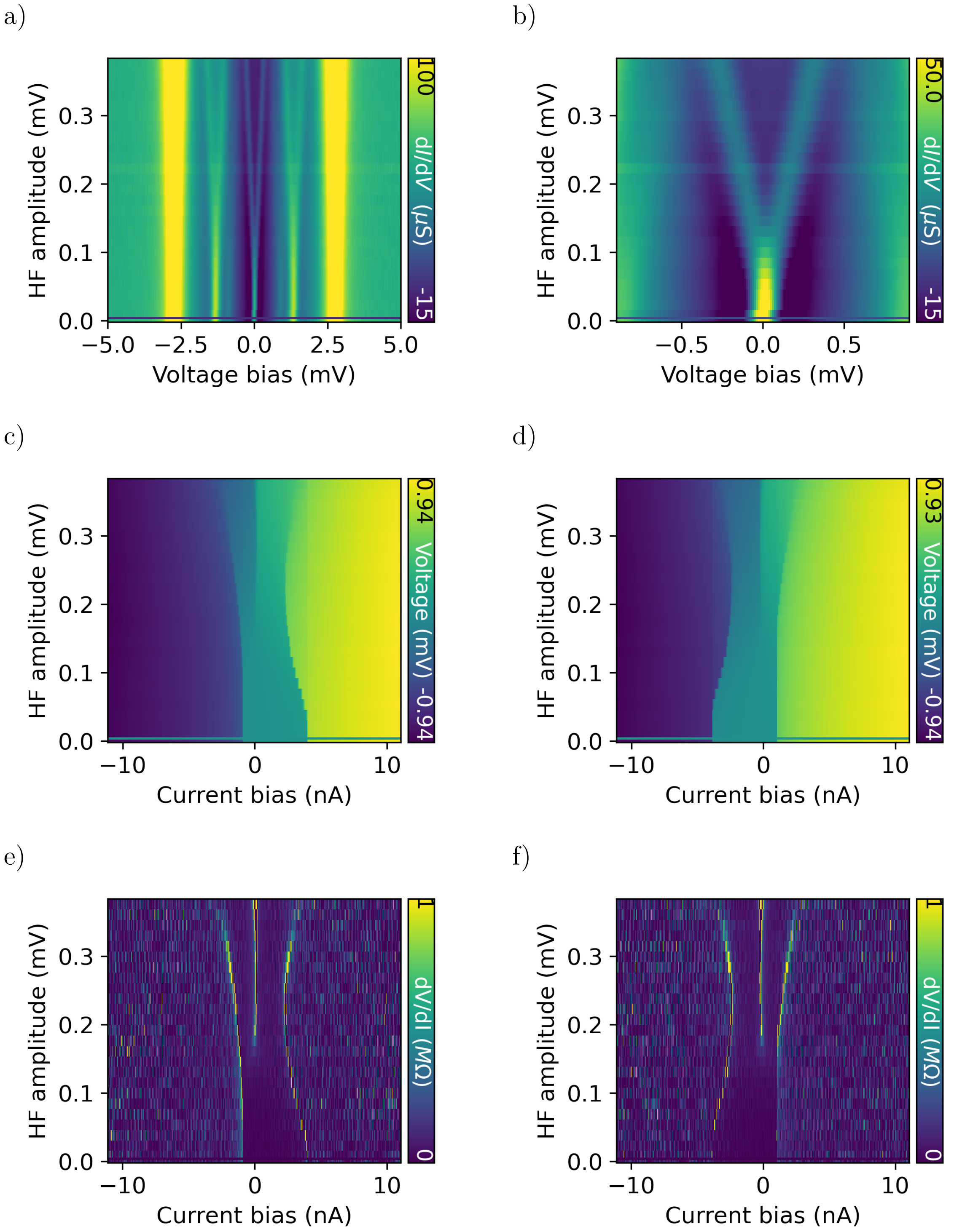

Figure C.3: 50 µS Josephson junction on a Pb adatom under 30 GHz HF irradiation. a) shows the voltage-biased dI/dV spectra (amplitude $V_{rms} = 20\,\mu\text{V}$) for an increasing HF amplitude. b) shows the zoom in on the Josephson peak. In c) and d) the current-biased V(I)Cs are displayed for both sweep directions. The derivative of these data sets is plotted in e) and f).

REFERENCES

[1] Martina Trahms et al. "Diode effect in Josephson junctions with a single magnetic atom". *Nature* 615.7953 (2023), pp. 628–633. ISSN: 1476-4687. DOI: `10.1038/s41586-023-05743-z`.

[2] B. D. Josephson. "Possible new effects in superconductive tunnelling". *Physics Letters* 1.7 (1962), pp. 251–253. ISSN: 0031-9163. DOI: `10.1016/0031-9163(62)91369-0`.

[3] J. Clarke and A. I. Braginski. *The SQUID handbook*. Weinheim: Wiley-VCH, 2006. ISBN: 9783527609956. DOI: `10.1002/9783527609956`.

[4] R. L. Fagaly. "Superconducting quantum interference device instruments and applications". *Review of Scientific Instruments* 77.10 (2006). ISSN: 0034-6748. DOI: `10.1063/1.2354545`.

[5] Sidney Shapiro. "Josephson Currents in Superconducting Tunneling: The Effect of Microwaves and Other Observations". *Physical Review Letters* 11.2 (1963), p. 80. ISSN: 0031-9007. DOI: `10.1103/PhysRevLett.11.80`.

[6] Clark A. Hamilton. "Josephson voltage standards". *Review of Scientific Instruments* 71.10 (2000), pp. 3611–3623. ISSN: 0034-6748. DOI: `10.1063/1.1289507`.

[7] B. Jeanneret and S. P. Benz. "Application of the Josephson effect in electrical metrology". *The European Physical Journal Special Topics* 172.1 (2009), pp. 181–206. ISSN: 1951-6401. DOI: `10.1140/epjst/e2009-01050-6`.

[8] Samuel A. Wilkinson and Jared H. Cole. "Linear response theory of Josephson junction arrays in a microwave cavity". *Physical Review B* 99.13 (2019). ISSN: 2469-9950. DOI: `10.1103/PhysRevB.99.134502`.

[9] Guido Burkard. *Theory of solid state quantum information processing*. 2004.

[10] Yuriy Makhlin, Gerd Schön, and Alexander Shnirman. "Quantum-state engineering with Josephson-junction devices". *Reviews of Modern Physics* 73.2 (2001), pp. 357–400. ISSN: 0038-5646. DOI: `10.1103/RevModPhys.73.357`.

[11] G. Wendin and V. S. Shumeiko. “Quantum bits with Josephson junctions (Review Article)”. *Low Temperature Physics* 33.9 (2007), pp. 724–744. ISSN: 1063-777X. DOI: `10.1063/1.2780165`.

[12] Fuyuki Ando et al. “Observation of superconducting diode effect”. *Nature* 584.7821 (2020), pp. 373–376. ISSN: 1476-4687. DOI: `10.1038/s41586-020-2590-4`.

[13] Akito Daido, Yuhei Ikeda, and Youichi Yanase. “Intrinsic Superconducting Diode Effect”. *Physical review letters* 128.3 (2022), p. 037001. DOI: `10.1103/PhysRevLett.128.037001`.

[14] Noah F. Q. Yuan and Liang Fu. “Supercurrent diode effect and finite-momentum superconductors”. *Proceedings of the National Academy of Sciences* 119.15 (2022), e2119548119. DOI: `10.1073/pnas.2119548119`.

[15] Christian Baumgartner et al. “Supercurrent rectification and magnetochiral effects in symmetric Josephson junctions”. *Nat. Nanotechnol.* 17.1 (Nov. 2021), pp. 39–44. DOI: `10.1038/s41565-021-01009-9`.

[16] Banabir Pal et al. “Josephson diode effect from Cooper pair momentum in a topological semimetal”. *Nature Physics* 18.10 (2022), pp. 1228–1233. ISSN: 1745-2473. DOI: `10.1038/s41567-022-01699-5`.

[17] E. Strambini et al. “Superconducting spintronic tunnel diode”. *Nature Communications* 13.1 (2022), pp. 1–7. ISSN: 2041-1723. DOI: `10.1038/s41467-022-29990-2`.

[18] Daniel Margineda et al. “Sign reversal diode effect in superconducting Dayem nanobridges”. *Communications Physics* 6.1 (2023), pp. 1–9. ISSN: 2399-3650. DOI: `10.1038/s42005-023-01458-9`.

[19] Sanat Ghosh et al. “High-temperature Josephson diode”. *Nature Materials* (2024), pp. 1–7. ISSN: 1476-4660. DOI: `10.1038/s41563-024-01804-4`.

[20] Margarita Davydova, Saranesh Prembabu, and Liang Fu. “Universal Josephson diode effect”. *Science Adv.* 8.23 (2022), eabo0309. DOI: `10.1126/sciadv.abo0309`.

[21] Klaus Halterman et al. “Supercurrent diode effect, spin torques, and robust zero-energy peak in planar half-metallic trilayers”. *Physical Review B* 105.10 (2022), p. 104508. ISSN: 2469-9950. DOI: `10.1103/PhysRevB.105.104508`.

[22] Heng Wu et al. “The field-free Josephson diode in a van der Waals heterostructure”. *Nature* 604.7907 (2022), pp. 653–656. ISSN: 1476-4687. DOI: `10.1038/s41586-022-04504-8`.

[23] G. Binnig et al. “Tunneling through a controllable vacuum gap”. *Applied Physics Letters* 40.2 (1982), pp. 178–180. ISSN: 0003-6951. DOI: `10.1063/1.92999`.

[24] G. Binnig et al. “Surface Studies by Scanning Tunneling Microscopy”. *Physical Review Letters* 49.1 (1982), p. 57. ISSN: 0031-9007. DOI: `10.1103/PhysRevLett.49.57`.

[25] S. H. Pan, E. W. Hudson, and J. C. Davis. “Vacuum tunneling of superconducting quasiparticles from atomically sharp scanning tunneling microscope tips”. *Applied Physics Letters* 73.20 (1998), pp. 2992–2994. ISSN: 00036951. DOI: `10.1063/1.122654`.

[26] Michael Ruby et al. “Experimental demonstration of a two-band superconducting state for lead using scanning tunneling spectroscopy”. *Physical review letters* 114.15 (2015), p. 157001. DOI: `10.1103/PhysRevLett.114.157001`.

[27] O. Naaman, W. Teizer, and R. C. Dynes. “Fluctuation Dominated Josephson Tunneling with a Scanning Tunneling Microscope”. *Phys. Rev. Lett.* 87 (9 Aug. 2001), p. 097004. DOI: `10.1103/PhysRevLett.87.097004`.

[28] J. G. Rodrigo, H. Suderow, and S. Vieira. “On the use of STM superconducting tips at very low temperatures”. *Eur. Phys. J. B* 40.4 (2004), pp. 483–488. ISSN: 14346028. DOI: `10.1140/epjb/e2004-00273-y`.

[29] M. Ternes et al. “Subgap structure in asymmetric superconducting tunnel junctions”. *Phys. Rev. B* 74.13 (2006), p. 132501. DOI: `10.1103/PhysRevB.74.132501`.

[30] Hikari Kimura et al. “Josephson scanning tunneling microscopy: A local and direct probe of the superconducting order parameter”. *Physical Review B* 80.14 (2009), p. 144506. ISSN: 2469-9950. DOI: `10.1103/PhysRevB.80.144506`.

[31] J. G. Rodrigo, V. Crespo, and S. Vieira. “Josephson current at atomic scale: Tunneling and nanocontacts using a STM”. *Physica C: Superconductivity and its Applications* 437-438 (2006), pp. 270–273. ISSN: 09214534. DOI: `10.1016/j.physc.2005.12.040`.

[32] Jacob Senkpiel et al. “Single channel Josephson effect in a high transmission atomic contact”. *Communications Physics* 3.1 (2020), pp. 1–6. ISSN: 2399-3650. DOI: `10.1038/s42005-020-00397-z`.

[33] Benjamin W. Heinrich, Jose I. Pascual, and Katharina J. Franke. “Single magnetic adsorbates on s -wave superconductors”. *Progress in Surface Science* 93.1 (2018), pp. 1–19. ISSN: 00796816. DOI: `10.1016/j.progsurf.2018.01.001`.

[34] K. J. Franke, G. Schulze, and J. I. Pascual. “Competition of superconducting phenomena and Kondo screening at the nanoscale”. *Science (New York, N.Y.)* 332.6032 (2011), pp. 940–944. DOI: `10.1126/science.1202204`.

[35] A. Yazdani et al. “Probing the Local Effects of Magnetic Impurities on Superconductivity”. *Science (New York, N.Y.)* 275.5307 (1997), pp. 1767–1770. DOI: `10.1126/science.275.5307.1767`.

[36] Luh Yu. “Bound States in superconductors with paramagnetic impurities”. *Acta Physica Sinica* 21.1 (1965), p. 75. ISSN: 1000-3290. DOI: `10.7498/aps.21.75`.

[37] Hiroyuki Shiba. “Classical Spins in Superconductors”. *Progress of Theoretical Physics* 40.3 (1968), pp. 435–451. ISSN: 0033-068X. DOI: `10.1143/PTP.40.435`.

[38] A. I. Rusinov. “Superconductivity near a paramagnetic impurity”. *JETP Lett. (USSR) (Engl. Transl.); (United States)* 9 (Jan. 1969).

[39] Michael Ruby et al. “Tunneling Processes into Localized Subgap States in Superconductors”. *Physical review letters* 115.8 (2015), p. 087001. DOI: `10.1103/PhysRevLett.115.087001`.

[40] Michael Ruby et al. “Orbital Picture of Yu-Shiba-Rusinov Multiplets”. *Physical review letters* 117.18 (2016), p. 186801. DOI: `10.1103/PhysRevLett.117.186801`.

[41] Michael Ruby et al. “Wave-Function Hybridization in Yu-Shiba-Rusinov Dimers”. *Physical review letters* 120.15 (2018), p. 156803. DOI: `10.1103/PhysRevLett.120.156803`.

[42] Laëtitia Farinacci et al. “Tuning the Coupling of an Individual Magnetic Impurity to a Superconductor: Quantum Phase Transition and Transport”. *Physical review letters* 121.19 (2018), p. 196803. DOI: `10.1103/PhysRevLett.121.196803`.

[43] Eva Liebhaber et al. “Yu-Shiba-Rusinov States in the Charge-Density Modulated Superconductor $NbSe_2$”. *Nano Lett.* 20.1 (2020), pp. 339–344. DOI: `10.1021/acs.nanolett.9b03988`.

[44] Mallika T. Randeria et al. “Scanning Josephson spectroscopy on the atomic scale”. *Physical Review B* 93.16 (2016), p. 161115. ISSN: 2469-9950. DOI: `10.1103/PhysRevB.93.161115`.

[45] Felix Küster et al. “Correlating Josephson supercurrents and Shiba states in quantum spins unconventionally coupled to superconductors”. *Nature Commun.* 12.1 (Feb. 2021), p. 1108. DOI: `10.1038/s41467-021-21347-5`.

[46] Gert-Ludwig Ingold and Yu. V. Nazarov. “Charge Tunneling Rates in Ultrasmall Junctions”. *in: "Single Charge Tunneling", edited by H. Grabert and M. H. Devoret, NATO ASI Series B, Vol. 294, pp. 21-107 (Plenum Press, New York* 294 (2005).

[47] Berthold Jäck et al. “Critical Josephson current in the dynamical Coulomb blockade regime”. *Physical Review B* 93.2 (2016), p. 020504. ISSN: 2469-9950. DOI: 10.1103/PhysRevB.93.020504.

[48] Christian R. Ast et al. “Sensing the quantum limit in scanning tunnelling spectroscopy”. *Nature Communications* 7.1 (2016), pp. 1–8. ISSN: 2041-1723. DOI: 10.1038/ncomms13009.

[49] P. K. Tien and J. P. Gordon. “Multiphoton Process Observed in the Interaction of Microwave Fields with the Tunneling between Superconductor Films”. *Physical Review* 129.2 (1963), pp. 647–651. ISSN: 0031-899X. DOI: 10.1103/PhysRev.129.647.

[50] G. Falci, V. Bubanja, and Gerd Schön. “Quasiparticle and Cooper pair tenneling in small capacitance Josephson junctions”. *Zeitschrift für Physik B Condensed Matter* 85.3 (1991), pp. 451–458. ISSN: 1431-584X. DOI: 10.1007/BF01307643.

[51] A. Roychowdhury et al. “Microwave Photon-Assisted Incoherent Cooper-Pair Tunneling in a Josephson STM”. *Physical Review Applied* 4.3 (2015), p. 034011. DOI: 10.1103/PhysRevApplied.4.034011.

[52] Olof Peters et al. “Resonant Andreev reflections probed by photon-assisted tunnelling at the atomic scale”. *Nature Phys.* 16.12 (2020), pp. 1222–1226. DOI: https://doi.org/10.1038/s41567-020-0972-z.

[53] H. Kamerlingh Onnes. “The liquification of helium”. *KNAW, Proceedings* 11 (1909), pp. 168–185.

[54] Rudolf Gross and Achim Marx. *Festkörperphysik*. Oldenburg Wissenschaftsverlag, 2014. ISBN: 978-3-11-035869-8. DOI: 10.1524/9783110358704.

[55] W. Meissner and R. Ochsenfeld. “Ein neuer Effekt bei Eintritt der Supraleitfhigkeit”. *Die Naturwissenschaften* 21.44 (1933), pp. 787–788. ISSN: 0028-1042. DOI: 10.1007/BF01504252.

[56] Charles P. Poole et al. “Phenomenon of superconductivity”. In: *Superconductivity*. Ed. by Charles P. Poole. Vol. B. 47. Elsivier Insights. Amsterdam, Netherlands: Elsevier Inc, 2014, pp. 33–85. ISBN: 9780124095090. DOI: 10.1016/B978-0-12-409509-0.00002-0.

[57] J. Bardeen, L. N. Cooper, and J. R. Schrieffer. “Theory of Superconductivity”. *Physical Review* 108.5 (1957), p. 1175. ISSN: 0031-899X. DOI: 10.1103/PhysRev.108.1175.

[58] V.L. Ginzburg and L. D. Landau. “On the Theory of superconductivity”. 20 (1950), pp. 1064–1082. DOI: 10.1016/B978-0-08-010586-4.50035-3.

[59] Michael Tinkham. *Introduction to Superconductivity*. 2nd ed. Dover Publications, June 2004. ISBN: 0486435032.

[60] Harald Ibach and Hans Lüth. *Festkörperphysik: Einführung in die Grundlagen*. 7. Aufl. 2009. Springer-Lehrbuch. Berlin, Heidelberg: Springer Berlin Heidelberg, 2009.

[61] Combescot, Roland. "Phenomenology". In: *Superconductivity: An Introduction*. Cambridge University Press, 2022, pp. 1–27. DOI: 10.1017/9781108560184.002.

[62] A. B. Pippard. "An experimental and theoretical study of the relation between magnetic field and current in a superconductor". *Proceedings of the Royal Society of London. Series A. Mathematical and Physical Sciences* 216.1127 (1953), pp. 547–568. ISSN: 0080-4630. DOI: 10.1098/rspa.1953.0040.

[63] A. V. Balatsky, I. Vekhter, and Jian-Xin Zhu. "Impurity-induced states in conventional and unconventional superconductors". *Reviews of Modern Physics* 78.2 (2006), pp. 373–433. ISSN: 0038-5646. DOI: 10.1103/RevModPhys.78.373.

[64] Laëtitia Farinacci et al. "Interfering Tunneling Paths through Magnetic Molecules on Superconductors: Asymmetries of Kondo and Yu-Shiba-Rusinov Resonances". *Physical review letters* 125.25 (2020), p. 256805. DOI: 10.1103/PhysRevLett.125.256805.

[65] J. Kondo. "Resistance Minimum in Dilute Magnetic Alloys". *Progress of Theoretical Physics* 32.1 (1964), pp. 37–49. ISSN: 0033-068X. DOI: 10.1143/PTP.32.37.

[66] Felix Oppen, Yang Peng, and Falko Pientka. "Topological superconducting phases in one dimension: Lecture Notes of the Les Houches Summer School: Volume 103, August 2014". In: Jan. 2017, pp. 387–450. ISBN: 9780198785781. DOI: 10.1093/acprof:oso/9780198785781.003.0009.

[67] Alexander C. Hewson. *The Kondo problem to heavy fermions*. 1. paperback ed. (with corr.), transferred to digital printing 2003. Vol. 2. Cambridge studies in magnetism. Cambridge: Cambridge Univ. Press, 2003. ISBN: 0521599474.

[68] Laëtitia Farinacci. "Tuning the Interactions of Magnetic Molecules on a Superconductor". PhD thesis. Freie Universität Berlin, 2020. DOI: 10.17169/REFUBIUM-27604.

[69] T. Matsuura. "The Effects of Impurities on Superconductors with Kondo Effect". *Progress of Theoretical Physics* 57.6 (1977), pp. 1823–1835. ISSN: 0033-068X. DOI: 10.1143/PTP.57.1823.

[70] Nino Hatter et al. "Magnetic anisotropy in Shiba bound states across a quantum phase transition". *Nature communications* 6.1 (2015), p. 8988. DOI: 10.1038/ncomms9988.

[71] P. G. de Gennes. *Superconductivity of Metals and Alloys*. CRC Press, 2018. ISBN: 9780429497032. DOI: 10.1201/9780429497032.

[72] C. W. J. Beenakker. “Colloquium : Andreev reflection and Klein tunneling in graphene”. *Reviews of Modern Physics* 80.4 (2008), pp. 1337–1354. ISSN: 0038-5646. DOI: `10.1103/RevModPhys.80.1337`.

[73] C. W. J. Beenakker. “Random-matrix theory of quantum transport”. *Reviews of Modern Physics* 69.3 (1997), pp. 731–808. ISSN: 0038-5646. DOI: `10.1103/RevModPhys.69.731`.

[74] Francesco Tafuri. *Fundamentals and Frontiers of the Josephson Effect.* Springer Cham, Sept. 2019. ISBN: 9783030207267.

[75] A.F. Andreev. “The Thermal Conductivity of the Intermediate State in Superconductors”. *Soviet Physics-JETP* 19 (1964), pp. 1228–1232.

[76] G. E. Blonder, M. Tinkham, and T. M. Klapwijk. “Transition from metallic to tunneling regimes in superconducting microconstrictions: Excess current, charge imbalance, and supercurrent conversion”. *Physical Review B* 25.7 (1982), pp. 4515–4532. ISSN: 2469-9950. DOI: `10.1103/PhysRevB.25.4515`.

[77] Rudolf Gross and Achim Marx. *Lecture notes: Applied Superconductivity: Josephson Effect and Superconducting Electronics, Chapter 3.* `https://www.wmi.badw.de/teaching/lecture-notes`. Walther-Meißner-Institut, Oct. 2005.

[78] Vinay Ambegaokar and Alexis Baratoff. “Tunneling Between Superconductors”. *Phys. Rev. Lett.* 10 (11 June 1963), pp. 486–489. DOI: `10.1103/PhysRevLett.10.486`.

[79] W. C. Stewart. “Current-voltage characteristics of Josephson junctions”. *Applied Physics Letters* 12.8 (1968), pp. 277–280. ISSN: 0003-6951. DOI: `10.1063/1.1651991`.

[80] D. E. McCumber. “Effect of ac Impedance on dc Voltage–Current Characteristics of Superconductor Weak–Link Junctions”. *Journal of Applied Physics* 39.7 (1968), pp. 3113–3118. ISSN: 0021-8979. DOI: `10.1063/1.1656743`.

[81] R. L. Kautz and John M. Martinis. “Noise-affected I-V curves in small hysteretic Josephson junctions”. *Phys. Rev. B* 42 (16 Dec. 1990), pp. 9903–9937. DOI: `10.1103/PhysRevB.42.9903`.

[82] Joachim Ankerhold, Hermann Grabert, and Philip Pechukas. “Quantum Brownian motion with large friction”. *Chaos (Woodbury, N.Y.)* 15.2 (2005), p. 26106. ISSN: 1054-1500. DOI: `10.1063/1.1855731`.

[83] Berthold Jäck. “Josephson Tunneling at the Atomic Scale: The Josephson Effect as a Local Probe”. PhD thesis. 2015. DOI: `10.5075/EPFL-THESIS-6750`.

[84] Berthold Jäck et al. “Quantum Brownian Motion at Strong Dissipation Probed by Superconducting Tunnel Junctions”. *Phys. Rev. Lett.* 119 (14 Oct. 2017), p. 147702. DOI: `10.1103/PhysRevLett.119.147702`.

[85] A. Steinbach et al. “Direct Measurement of the Josephson Supercurrent in an Ultrasmall Josephson Junction”. *Physical Review Letters* 87.13 (2001), p. 137003. ISSN: 0031-9007. DOI: 10.1103/PhysRevLett.87.137003.

[86] Jan Olof Peters. “Transport Processes through Superconducting Junctions at the Atomic Scale: Implementation of a High-Frequency Circuit into a Scanning Tunneling Microscope”. PhD thesis. Freie Universität Berlin, 2020.

[87] R. L. Kautz. “The ac Josephson effect in hysteretic junctions: Range and stability of phase lock”. *Journal of Applied Physics* 52.5 (1981), pp. 3528–3541. ISSN: 0021-8979. DOI: 10.1063/1.329132.

[88] R. L. Kautz. “Noise, chaos, and the Josephson voltage standard”. *Reports on Progress in Physics* 59.8 (1996), pp. 935–992. ISSN: 0034-4885. DOI: 10.1088/0034-4885/59/8/001.

[89] Dmitry Shcherbakov et al. “Layer- and gate-tunable spin-orbit coupling in a high-mobility few-layer semiconductor”. *Science advances* 7.5 (2021). DOI: 10.1126/sciadv.abe2892.

[90] Ryohei Wakatsuki et al. “Nonreciprocal charge transport in noncentrosymmetric superconductors”. *Science Adv.* 3.4 (2017), e1602390. DOI: 10.1126/sciadv.1602390.

[91] Ryohei Wakatsuki and Naoto Nagaosa. “Nonreciprocal Current in Noncentrosymmetric Rashba Superconductors”. *Physical Review Letters* 121.2 (2018), p. 026601. ISSN: 0031-9007. DOI: 10.1103/PhysRevLett.121.026601.

[92] Lorenz Bauriedl et al. “Supercurrent diode effect and magnetochiral anisotropy in few-layer $NbSe_2$”. *Nature Commun.* 13.1 (July 2022), p. 4266.

[93] Jiang-Xiazi Lin et al. “Zero-field superconducting diode effect in small-twist-angle trilayer graphene”. *Nature Physics* 18.10 (2022), pp. 1221–1227. ISSN: 1745-2473. DOI: 10.1038/s41567-022-01700-1.

[94] Harley D Scammell, J I A Li, and Mathias S Scheurer. “Theory of zero-field superconducting diode effect in twisted trilayer graphene”. *2D Materials* 9.2 (2022), p. 025027. ISSN: 2053-1583. DOI: 10.1088/2053-1583/ac5b16.

[95] Jonginn Yun et al. “Magnetic proximity-induced superconducting diode effect and infinite magnetoresistance in a van der Waals heterostructure”. *Physical Review Research* 5.2 (2023), p. L022064. DOI: 10.1103/PhysRevResearch.5.L022064.

[96] Baoxing Zhai et al. “Prediction of ferroelectric superconductors with reversible superconducting diode effect”. *Physical Review B* 106.14 (2022). ISSN: 2469-9950. DOI: 10.1103/PhysRevB.106.L140505.

[97] James Jun He, Yukio Tanaka, and Naoto Nagaosa. “A phenomenological theory of superconductor diodes”. *New Journal of Physics* 24.5 (2022), p. 053014. ISSN: 1367-2630. DOI: 10.1088/1367-2630/ac6766.

[98] A. Costa et al. “Sign reversal of the Josephson inductance magnetochiral anisotropy and 0-π-like transitions in supercurrent diodes”. *Nature Nanotechnology* (2023), pp. 1–7. ISSN: 1748-3395. DOI: 10.1038/s41565-023-01451-x.

[99] J. Bardeen. “Tunneling from a many-particle point of view”. *Physical review letters* 55.4 (1961), pp. 6–8.

[100] J. Tersoff and D. R. Hamann. “Theory of the scanning tunneling microscope”. *Phys. Rev. B* 31.2 (1985), pp. 805–813. ISSN: 01631829. DOI: 10.1103/PhysRevB.31.805.

[101] Deung-Jang Choi et al. “Mapping the orbital structure of impurity bound states in a superconductor”. *Nature Commun.* 8 (2017), p. 15175. DOI: 10.1038/ncomms15175.

[102] Martina Trahms et al. *Original experimental data and code for the Paper "Diode effect in Josephson junctions with a single magnetic atom"*. 2023. DOI: 10.17169/REFUBIUM-37060.

[103] Trevyn F. Q. Larson et al. “Zero Crossing Steps and Anomalous Shapiro Maps in Graphene Josephson Junctions”. *Nano letters* 20.10 (2020), pp. 6998–7003. DOI: 10.1021/acs.nanolett.0c01598.

[104] Y. Koval, M. V. Fistul, and A. V. Ustinov. “Enhancement of Josephson phase diffusion by microwaves”. *Physical review letters* 93.8 (2004), p. 087004. DOI: 10.1103/PhysRevLett.93.087004.

[105] Jacob F. Steiner et al. “Diode Effects in Current-Biased Josephson Junctions”. *Physical Review Letters* 130.17 (2023), p. 177002. ISSN: 0031-9007. DOI: 10.1103/PhysRevLett.130.177002.

[106] Hermann Grabert and Gert-Ludwig Ingold. “Mesoscopic Josephson effect”. *Superlattices and Microstructures* 25.5 (1999), pp. 915–923. ISSN: 0749-6036. DOI: 10.1006/spmi.1999.0739.

[107] Idan Tamir et al. “Shot-noise measurements of single-atom junctions using a scanning tunneling microscope”. *The Review of scientific instruments* 93.2 (2022), p. 023702. DOI: 10.1063/5.0078917.

[108] K. M. Bastiaans et al. “Imaging doubled shot noise in a Josephson scanning tunneling microscope”. *Physical Review B* 100.10 (2019). ISSN: 2469-9950. DOI: 10.1103/PhysRevB.100.104506.

LIST OF PUBLICATIONS

Publications related to this thesis

First author:

- M. Trahms, L. Melischek, J. F. Steiner, B. Mahendru, I. Tamir, N. Bogdanoff, O. Peters, G. Reecht, C. B. Winkelmann, F. von Oppen, K. J. Franke, *"Diode effect in Josephson junctions with a single magnetic atom"*, Nature **615**, 628-633 (2023).

Co-author:

- J. F. Steiner, L. Melischek, M. Trahms, K. J. Franke, F. von Oppen, *"Diode effects in current-biased Josephson junctions"*, Phys. Rev. Lett. **130**, 177002 (2023).

Conference contribution

2019

- **Poster** - *"Superconductive coupling in tailored [(SnSe)1+δ]m[NbSe2]1 multilayers"*, Lorentz center: 'The Challenge of 2-Dimensional Superconductivity', July 2019, Leiden, Netherlands.
- **Poster** - *"Scanning tunnelling spectroscopy on disordered superconductors"*, 704. Wilhelm und Else Heraeus-Seminar 'Exploring the Limits of Nanoscience with Scanning Probe Methods', October 2019, Bad Honnef, Germany.

2021

- **Poster** - *"Switching current distribution in an STM Josephson junction on a Pb(111) surface with Mn adatoms"*, DPG-Tagung der Sektion Kondensierte Materie (SKM), September/October 2021, virtual conference.

2022

- **Poster** - *"Phase dynamics in current-biased Josephson junctions in the presence of Yu-Shiba-Rusinov bound states"*, 769. WE-Heraeus-Seminar on 'Novel Quantum Phases in Superconducting Heterostructures, May/June 2022, Bad Honnef, Germany.
- **Talk** - *"Non reciprocity in current biased Josephson junctions in the presence of Yu Shiba Rusinov bound states"*, 12th International Conference on Magnetic and Superconducting Materials (MSM22), August/September 2022, Duisburg, Germany.
- **Talk** - *"Non reciprocity in current biased Josephson junctions in the presence of Yu Shiba Rusinov bound states"*, DPG-Tagung der Sektion Kondensierte Materie (SKM), September 2022, Regensburg, Germany.

Publications not related to this thesis

First author:

- M. Trahms, M. Jost, C. T. Trinh, N. Preissler, S. Albrecht, R. Schlatmann, B. Rech, D. Amkreutz, *"All-Thin-Film Tandem Cells Based on Liquid Phase Crystallized Silicon and Perovskites"*, IEEE Journal of Photovoltaics **9** 3 (2019).
- M. Trahms, C. Grosse, M. B. Alemayehu, O. K. Hite, O. Chiatti, A. Mogilatenko, D. C. Johnson, S. F. Fischer, *"Superconductive coupling in tailored [(SnSe)1+δ]m(NbSe2)1 multilayers"*, Supercond. Sci. Technol. **31** 065006 (2018).

Co-author:

- I. Tamir, M. Trahms, F. Gorniaczyk, F. von Oppen, D. Shahar, K. J. Franke, *Direct observation of intrinsic surface magnetic disorder in amorphous superconducting films"*, Phys. Rev. B **105** L140505 (2022).
- C. T. Trinh, M. Bokalic, N. Preissler, M. Trahms, D. Abou-Ras, R. Schlatmann, D. Amkreutz, M. Topic, *"Assessment of Bulk and Interface Quality for Liquid Phase Crystallized Silicon on Glass"*, IEEE Journal of Photovoltaics **9** 2 (2019).
- N. Preissler, D. Amkreutz, J. Dulanto, J. A. Töfflinger, C. T. Trinh, M. Trahms, D. Abou-Ras, H. Kirmse, R. Weingärtner, B. Rech, R. Schlatmann, *"Passivation of Liquid-Phase Crystallized Silicon With PECVD-SiNx and PECVD-SiNx/SiOx"*, Phys. Status Solidi A **215** 1800239 (2018).
- C. T. Trinh, N. Preissler, P. Sonntag, M. Muske, K. Jäger, M. Trahms, R. Schlatmann, B. Rech, Daniel Amkreutz, *"Potential of interdigitated back-contact silicon heterojunction solar cells for liquid phase crystallized silicon on glass with efficiency above 14%"*, Solar Energy Materials and Solar Cells **174** 187-195 (2018).
- N. Preissler, C. T. Trinh, M. Trahms, P. Sonntag, D. Abou-Ras, H. Kirmse, R. Schlatmann, B, Rech, D. Amkreutz, *"Impact of Dielectric Layers on Liquid-Phase Crystallized Silicon Solar Cells"*, IEEE Journal of Photovoltaics **8** 1 (2018).
- N. Preissler D. Amkreutz, P. Sonntag, M. Trahms, R. Schlatmann, B. Rech, *"Interface Engineering for Liquid-Phase Crystallized-Silicon Solar Cells on Glass"*, Sol. RRL **1** 170015 (2017).
- D. Amkreutz, N. Preissler, C. T. Trinh, M. Trahms, P. Sonntag, R. Schlatmann, B. Rech, *"Influence of the precursor layer composition and deposition processes on the electronic quality of liquid phase crystallized silicon absorbers"*, Prog. Photovolt Res. Appl. **26** (2017).

- P. Sonntag, N. Preissler, M. Bokali**c**, M. Trahms, J. Haschke, R. Schlatmann, M. Topi**c**, B. Rech, D. Amkreutz, *"Silicon Solar Cells on Glass with Power Conversion Efficiency above 13% at Thickness below 15 Micrometer"*, Scientific Reports **7.1** (2017).

ACKNOWLEDGEMENT

It is impossible to mention all the ways so many different people supported and helped me during the years of my PhD studies. Here is an attempt to at least mention some of you.

First and foremost, I want to thank Prof. Dr. Katharina Franke. Working with you was such a great combination of exciting physics, new and challenging lab work and a great group atmosphere. Even though times were tough for a while, you helped keeping up the motivation and the group spirit. The last years have shown me how great working as a scientist can be.

Thank you also to Prof. Dr. Martin Wolf for being the second reviewer of this work. Physics can be so exciting especially if knowledge and understanding is deepened by so many fruitful discussions. For that I want to thank Prof Dr. Felix von Oppen and his group. Especially Larissa Melischek and Jacob Steiner who were always ready to squeeze in another discussion and to share their knowledge and insights so openly. A lot of value was added to the experiments by your understanding and feedback. Thank you also to Prof. Dr. Clemens Winkelmann. Your insights both in the lab as well as when it comes to discussing physics have been very important to deepen my understanding of Josephson physics. Thank you for the great discussions.

Of course I would like to thank all of my colleagues from AG Franke for all the help whether it was related to the lab, discussing physics or eating cake and drinking coffee. Thanks to Gaël Reecht, I cannot emphasize enough how much you helped me in the beginning of my work at the group. It was so helpful for me to have someone as patient to bounce off all my questions and insecurities as well as to discuss improvements and repairs of the setup! Thanks also to Christian Lotze. It is amazing how you manage to help everyone seemingly at once with everything. A big thank you to Jennifer Hartfiel, for being there for me through the whole process of this thesis. Climbing rocks;) Thank you to Rika Simon for all the musical, switch and board game fun we had! It is good to know there is always someone to nerd-out with! Verena Caspari and Bharti Mahendru, thank you for carrying on with the project! It really motivates me knowing that the project lives on! I also would like to thank Idan Tamir and Laëtitia Farinacci you both pushed me to be a better scientist.

Last but not least, I would like to thank my friends and family. Though you might not be aware, the help you provided was invaluable to me. Thank you Julia and Daniela for being so patient and providing the distractions I needed when I buried myself in my work! I know I can always rely on you. A huge thank you to my family.

Without you none of this would have been possible. To my parents who supported me throughout my whole studies in all possible ways. To Carola and Johannes, you were always there for me when the rain started to pour. Thank you also to little Frederike, for just being very cute and putting things into perspective.

SELBSTSTÄNDIGKEITSERKLÄRUNG

Name: Trahms
Vorname: Martina

Ich erkläre gegenüber der Freien Universität Berlin, dass ich die vorliegende Dissertation selbstständig und ohne Benutzung anderer als der angegebenen Quellen und Hilfsmittel angefertigt habe. Die vorliegende Arbeit ist frei von Plagiaten. Alle Ausführungen, die wörtlich oder inhaltlich aus anderen Schriften entnommen sind, habe ich als solche kenntlich gemacht. Diese Dissertation wurde in gleicher oder ähnlicher Form noch in keinem früheren Promotionsverfahren eingereicht.

Mit einer Prüfung meiner Arbeit durch ein Plagiatsprüfungsprogramm erkläre ich mich einverstanden.

Datum, Unterschrift